Czech Technical University in Prague
Faculty of Electrical Engineering

Doctoral Thesis

February 2017

Václav Kabourek

Czech Technical University in Prague

Faculty of Electrical Engineering
Department of Electromagnetic Field

OBJECTS CHARACTERIZATION BY MEANS OF WIDEBAND SIGNALS

Doctoral Thesis

Ing. Václav Kabourek

Prague, February 2017

Ph.D. Programme: Electrical Engineering and Information Technology
Branch of Study: Radioelectronics

Supervisor: ***Prof. Ing. Miloš Mazánek, CSc.***
Supervisor-Specialist: ***Ing. Tomáš Kořínek, Ph.D.***

Abstract

Thesis deals with objects characterization by means of wideband signals. More specifically, radar cross section and high-resolution images are used to describe scattering behavior of objects in wide frequency band.

The aim of this thesis is then to develop a simple method allowing to predict accurate far field radar cross section of objects from their near field measurements and subsequently calculate high-resolution images of their contours.

According to these facts, appropriate techniques are investigated and thoroughly described. Circular near-field to far-field radar cross section prediction technique is selected to correct data obtained from mono-static, near field measurement of scattered field of selected electrically large objects. One-plane measurements are undertaken in full anechoic chamber at frequencies ranging from 3 GHz to 18 GHz. Obtained results are then compared to simulated values and discussed. Since test antenna introduces tapering errors into measured radar cross section values, its broadband radiation patterns are computed employing novel antenna impulse response measurement technique. Radiation pattern correction is subsequently employed in proposed overall computational method. Obtained results show good correspondence with simulated patterns. In order to verify its applicability in image processing, images of selected objects are created by means of inverse synthetic aperture radar technique. Following achieved results, presented overall correction scheme is proven to be suitable for both, radar cross section calculation as well for restoring contour of object shape in image domain.

Abstrakt

Dizertační práce pojednává o charakterizaci objektů pomocí širokopásmových signálů. V užším smyslu se jedná o určení jejich efektivní odrazné plochy v širokém frekvenčním pásmu a následnou obrazovou rekonstrukci tvaru na základě jejich rozptylových vlastností.

Cílem této dizertační práce je tedy navrhnout ucelenou metodu pro získání přesných hodnot efektivní odrazné plochy objektů z měření jejich odrazivosti v blízkém zářivém poli. Na základě těcho výsledků je dalším cílem rekonstrukce obrazů s vysokou rozlišitelností tvaru měřených objektů.

Dle vytýčených cílů je v práci popsán současný stav dané problematiky. Dále jsou podrobně rozebrány metody použité pro vlastní řešení. K získání potřebných dat je navrženo monostatické měření odrazivosti elektricky velkých objektů v bezodrazové komoře v širokém frekvenčním pásmu 3 - 18 GHz. Měření vychází z cylindrického skenování, avšak v tomto případě jsou uskutečněna pouze pro jeden horizontální řez. Z charakteru měření vychází vybraná metoda umožňující přepočet naměřených dat do vzdálené oblasti a následné vyjádření efentivní odrazné plochy. Vypočítané výsledky jsou porovnávány s hodnotami získanými simulacemi daných objektů a následně diskutovány. Kvůli malé měřené vzdálenosti je nutné počítat s chybami způsobenými neuniformní vyzařovací charakteristikou antény. Další část této práce proto popisuje novou metodu pro získání širokopásmových vyzařovacích charakteristik antén z měření jejich impulzních odezev jak v časové, tak ve frekvenční oblasti. Takto získané hodnoty jsou následně použity pro eliminaci vlivu antény v popisované transformační metodě. Z končených výsledků vyplývá dobrá shoda se simulovanými hodnotami. Použitelnost celkové navržené metody měření a korekce dat je dále zkoumána na obrazech vytvořených pomocí techniky inverzní syntetické apertury. Veškeré dosažené výsledky potvrzují schopnost a vhodnost popsaného postupu jak při výpočtu efektivní odrazné plochy, tak pro detekci obrysů různých objektů.

Prohlášení

Tímto prohlašuji, že svou dizertační práci na téma "Charakterizace objektů pomocí širokopásmových signálů" jsem vypracoval samostatně s použitím odborné literatury a dalších informačních zdrojů, které jsou všechny citovány v práci a uvedeny v seznamu literatury na konci této práce.

Jako autor uvedené dizertační práce dále prohlašuji, že jsem v souvislosti s vytvořením této práce neporušil autorská práva třetích osob, zejména jsem nezasáhl nedovoleným způsobem do cizích autorských práv osobnostních.

V Praze dne 27. února 2017

Václav Kabourek

Acknowledgments

Hereby I thank my supervisor Prof. Ing. Miloš Mazánek, CSc. for his support, guidance and valuable advices during my studies and this work. I would like to thank Ing. Tomáš Kořínek, Ph.D. and Ing. Petr Černý, Ph.D. for their patience, constant and valuable support and insightful guidance over the years. Last but not least, I thank to all my colleagues for their positive attitude, that led to inspiring and constructive working atmosphere.

February 24, 2017 Václav Kabourek

Contents

List of Abbreviations

Abbreviation	**Description**
AP	Antenna Pattern
AWACS	US Airborne Warning and Control System
BW	Band Width
CATR	Compact Antenna Test Range
CNFFFT	Circular Near Field to Far Field Transform
CW	Continuous Wave
DC	Direct Current
FD	Frequency Domain
FDTD	Finite-Difference Time-Domain method
FT	Fourier Transform
FF	Far Field
FFT	Fast Fourier Transform
FMCW	Frequency Modulated Continuous wave
IFFT	Inverse FFT
IFT	Inverse FT
LTI	Linear Time Invariant system
MoM	Methods of Moments
NF	Near Field
OSM	Open-Short-Match calibration
PCA	Principal Component Analysis
PEC	Perfect Electric Conductor
PG	Propelled Grenade
PRF	Pulse Repetition Frequency
RAM	Radar Absorbent Material
RCS	Radar Cross Section
RPG	Rocket-Propelled Grenade
Rx	Receive (antenna)
SFCW	Step Frequency Continuous Wave
SNR	Signal to Noise ratio
TD	Time Domain
TDT	Time Domain Transmission module
TOSM	Through-Open-Short-Match calibration
SVD	Singular Value Decomposition
Tx	Transmit (antenna)
UWB	Ultra WideBand

List of Symbols and Operators

Symbols

Symbol	Description
A	Amplitude
A_n	Sum of weighted cylindrical harmonics
$A_n(k_z)$	Spectral cylindrical expansion component
a_n	Cylindrical harmonic
$B_n(k_z)$	Spectral cylindrical expansion component
BW	Frequency bandwidth
$\mathbf{C}$	Covariance matrix of original data set
c	Speed of light in vacuum
D	Size of projected target
E	Intensity of electric field
$E_{cal.meas}$	Scattered electric field from calibration standard
E_{tg}	Scattered electric field from target
$E_{t-V,H}$	Transmitted electric field of vertical, horizontal polarization
$E_{r-V,H}$	Received electric field of vertical, horizontal polarization
e_i	Intensity of incident electric field in TD
$F(T_{1,2})$	Fresnel integral of argument $T_{1,2}$
f	Frequency
Δf	Frequency step
G, G_{tx}, G_{rx}	Gain of transmit/receive antenna
H	Intensity of magnetic field
$H_a(\omega)$	Transfer function of antenna in FD
$H_{back}(\omega)$	Transfer function of background in FD
$H_{cross}(\omega)$	Crosstalk transfer function in FD
$H_{ch}(\omega)$	Transfer function of transmission channel in FD
$H_n^{(1)}(x)$	Hankel function of the first kind, order n
$H_{ref}(\omega)$	Transfer function of reference antenna in FD
$H_{tg}(\omega)$	Transfer function of target
$H_{tx}(\omega)$	Transfer function of transmit antenna
h	Height of target
$h_{1,2,3}(t)$	Normalized effective height of antenna 1, 2, 3

$h_a(t)$	Normalized effective height of antenna
$h_{back}(t)$	Impulse response of background
$h_{cross}(t)$	Crosstalk response
$h_{meas}(t)$	Measured normalized effective height of antenna
$h_{rx}(t)$	Normalized effective height of receive antenna
$h_{tg}(t)$	Impulse response of target
$h_{tx}(t)$	Normalized effective height of transmit antenna
$I(x', y')$	Filtered Back-projection image of target
J_n	Bessel function of n-th order
j	Imaginary unit
$K(\omega)$	Constant including signal differentiation and Green's function
k	Wave number
k_a, k_r, k_x, k_y, k_z	Spatial wavenumbers
L	Losses
M	Maximum harmonics of antenna pattern
N	Maximum harmonics of scattered field
$P(\phi, k_r)$	Spatial harmonics projection
P_t	Transmit power
P_r	Receive power
p	Multiplicative constant
R	Range between scattering center γ and observation point
$\vec{R}$	Position vector of scattering center γ with respect to observation point
R_0	Distance from observation point to target center
$\vec{R_0}$	Position vector of target center with respect to observation point
$\hat{R_0}$	Unit position vector of $\vec{R_0}$
ΔR_0	Down range resolution
R_{FF}	Far field range
R_{unamb}	Unambiguous range
r	Range
$\vec{r}'$	Position vector of scattering center γ
$\hat{\boldsymbol{r}}$	Unit position vector
Δr	Range difference of spherical wavefront at target plane
r_{tg}	Minimum radius enclosing target
$\mathbf{S}$	Transformation matrix of PCA
$S_{11}, S_{12}, S_{21}, S_{22}$	Scattering parameters of common two-port
$S_{VV}, S_{VH}, S_{HV}, S_{HH}$	Polarimetric components of Sinclair matrix $[S]$
S_i	Incident plane wave at target plane
$S_{meas}(\omega)$	Transfer function of measured antenna in FD
S_r	Scattered field from target in NF, reflected plane wave at antenna aperture
$S_n(\phi, k)$	Coefficient of generalized Fourier series
S_r^{FF}	Scattered field from target in FF

$S_{ref}(\omega)$	Scattering coefficient of reference antenna in FD
t	Time
$\mathbf{U}$	Eigenvector matrix of $\mathbf{XX}^T$
$U_r(\phi, R)$	Received field in range domain in NF
$U_r^{NF}(n, k)$	Angular harmonics of received NF field
$U_{tx}(\omega)$	Spectrum of transmitted voltage in FD
$U_{rx}(\omega)$	Spectrum of received voltage in FD
$U_{rx}^{gated}(\omega)$	Spectrum of gated received voltage in FD
$u_i(\vec{R}, k)$	Incident field in NF
$u_r(\vec{R}_0, k)$	Received field in NF
$u_r'(\vec{R}, k)$	Received field contribution of particular scattering center in NF
$u_r^{NF}(\phi, k)$	Received pre-processed field in NF
$u_r^{FF}(\phi, k)$	Received scattered field in FF
$u_{rx}(t)$	Received voltage in TD
$u_{rx}^{back}(t)$	Received voltage from background reflectivity measurement in TD
$u_{rx}^{gated}(t)$	Time gated received voltage in TD
$u_{rx}^{subtr}(t)$	Background-subtracted received voltage from target reflectivity measurement in TD
$u_{rx}^{tg}(t)$	Received voltage from target reflectivity measurement in TD
$u_{tx}(t)$	Transmitted voltage in TD
$\mathbf{V}$	Eigenvector matrix of $\mathbf{XX}^T$
$W(\omega)$	Spectrum of gating window
w	Width of target
$w(t)$	Time window
$\mathbf{X}$	Matrix of original data set in PCA
$\tilde{\mathbf{X}}$	Matrix of PCA restored original data set from n components
$\mathbf{X}_0$	Matrix of mean-subtracted original data set
$\bar{x}_{ij}$	Mean value subtracted original data point x_{ij} of i-th row and j-th column
$\mathbf{Y}$	Matrix of transformed data set in PCA
Z	Impedance
Z_0	Impedance of free space
Z_{tx}	Impedance of transmit antenna at its terminal
Z_{rx}	Impedance of receive antenna at its terminal
Δz	Spatial sampling step in z direction
Γ_{air}	Reflection coefficient of air
Γ_L	Reflection coefficient of receiver
Γ_{meas}	Total reflection coefficient
Γ_{obj}	Target reflection coefficient
γ	Scattering center
δ	Dirac delta function
θ	Elevation angle

$\mathbf{\Lambda}$	Matrix of eigenvalues $\mathbf{XX}^T$
λ	Wavelength
λ_{max}	Maximum wavelength of used signal
λ_{min}	Minimum wavelength of used signal
σ	Radar Cross Section (RCS)
σ_{tg}	Radar Cross Section of target
$\sigma_{cal.comp}$	Analytical Radar Cross Section of calibration standard
τ	Convolution time constant
φ	Phase
$\Delta\varphi$	Phase shift
ϕ	Azimuthal angle of target and observation point
ϕ'	Azimuthal angle of particular scattering center
$\Delta\phi$	Azimuthal sampling step
ω	Angular velocity
$\hat{\boldsymbol{\phi}}$, $\hat{\boldsymbol{\theta}}$	Unit vectors of spherical coordinates
(x', y', z')	Coordinate system of target
(x, y, z)	Coordinate system of observation point

Operators

Operator	**Description**
$\mathscr{F}\{\cdot\}$	Fourier transformation
$\mathscr{F}^{-1}\{\cdot\}$	Inverse Fourier transformation
$\mathscr{H}\{\cdot\}$	Hilbert transformation
$\vert \cdot \vert$	Absolute value
$*$	Convolution operator
$[\cdot]^T$	Matrix transpose
$[\cdot]^{-1}$	Matrix inverse

Chapter 1

Introduction

Objects characterization by means of radio wave signals plays important role across many industry fields and applications. The term itself covers objects detection, localization and even determination of their shape. Radio waves, traveling within medium, reflect from obstacles, objects (that act as inhomogeneities) if their conductivity, dielectric and magnetic properties differ from properties of the medium. Re-radiated waves, created by currents induced in various points of an object, are summed differently in space depending on mutual phase relations. Resulting scattered field is consequently a product of incident waves having defined frequency and polarization as well as shape and electromagnetic properties of the object.

Knowing the intensity of backscattered field reflected from the object at certain aspect angle (or within whole angular span), the range from object to observation point can be determined and vice versa. In the terms of radar surveillance, this backscattered field is referred as radar cross section (RCS).

RCS measurement and determination is very important especially in military applications worldwide. The amount of backscattered power received by radar determines its maximum operational range and indicates detectability and trackability of an object, therefore there is an effort to reduce RCS of many targets as aircrafts, ships, missiles, etc.; [1], [2],[3]. Contrary to that, in automotive industry, knowing RCS of cars leads to development and implementation of adaptive cruise control systems and/or forward vehicle collision warning systems into cars in order to prevent or mitigate vehicle collisions; [4], [5], [6].

In the above mentioned cases, only mono or multi-frequency RCS characterization is often used. In practice, major problem of narrow-band radars is target-clutter separation owing to limited possibilities of clutter mitigation, since low-RCS targets can have similar or even smaller backscatter compared to their clutter environment (boats in sea, targets in forests, housing developments etc.). The term clutter mostly refers to undesirable reflections from environment that reduce detectability of target. Broadband radar systems (based i.e. on pulsed, stepped frequency, frequency modulated signals) are therefore used instead for their down-range resolution and penetration capabilities. Clutter can be than subtracted by means of time gating, Doppler filtering etc.; [7]. Following this, broadband backscattered signals can be used for targets shape reconstruction by means of Synthetic Aperture Radar (SAR) and its inverse form (ISAR). In the case of SAR, Ground Penetrating Radar (GPR) is widely used in the field of geophysical surveying for subsurface mapping, highway, building construction, archeology, for concealed and buried objects detection etc.; [8], [9], [10].

On the other hand, ISAR plays important role in maritime and airborne forces, where it is a powerful tool for characterization of scattering properties of radar targets, thus for automatic target recognition based on RCS; [11].

In both cases, measurements in far-field condition is assumed. Following theory, distance between radar and target needs to meet far-field criteria which implies the backscattered field can be approximated by plane wave at receive antenna.

Generally, obtaining precise RCS characteristics of electrically large-sized objects requires outdoor test ranges, [12]. Such measurement systems are very expensive and also extensive test sites are needed. However, the range can be effectively reduced i.e. by Compact Antenna Test Range (CATR) arrangement, [13]. The setup consisting of transmit antenna and reflector creates plane wave illumination of object under test. This technique requires a high-quality reflector and suffers from edge diffraction that limits size of volume, where illumination can be considered as plane wave (so called quite zone). Since the RCS measurements have begun important and challenging discipline across wide scientific society and research centers, the indoor RCS measurement techniques and systems have been developed as more affordable and all-weather usable alternative. Besides compact ranges, scaled model measurements are frequently employed to obtain RCS of original-sized objects, [14], [15]. Nevertheless, operational frequency increases together with model scaling. That leads to high demands on measurement system. Nowadays, computational possibilities of personal computers allow to incorporate simulation methods in modeling and prediction of RCS. Electromagnetic full-wave simulators, such as CST Microwave Studio, FEKO, ANSYS HFSS, etc., use basically powerful Method of Moments (MoM) and Finite-Difference Time-Domain (FDTD) methods to effectively simulate RCS of various objects; [16], [17]. Even though are these techniques good for RCS modeling in regime, where the wavelength and target size are comparable, calculation of RCS at high frequencies became difficult, especially in case of complex geometries of target. As frequency increases, the number of mesh cells (or wire meshes) dramatically increases.

Another technique of acquiring RCS pattern of electrically large objects at high frequencies in indoor facilities is based on near-field (NF) measurements. The estimate of far-field (FF) RCS pattern can be extrapolated from NF measurements of the object. Basic concepts have been adopted and used from NF antennas radiation pattern measurements since early 1970's; [18]. NF to FF techniques became applicable world-wide with development of frequency-swept systems able to measure both, amplitude and phase of signal and process measured data by means of fast Fourier transform (FFT). Nowadays, there are still challenges in obtaining FF RCS from NF data since correct NF measurement involves, according to equivalence principle, a knowledge of the field on surface enclosing target. Furthermore, from scattering point of view, transmit and receive antenna need to scan continuously and independently whole surface. This condition is practically not feasible and some approximative measurement technique need to be used instead.

The next challenge rises from the NF measurement itself, where phase of signals is involved in FF reconstruction process. Measured object is located in NF of the transmit/receive antenna and vice versa, thus phase and amplitude variation of antenna radiation pattern influences the power distribution on the object. Therefore, wide-beam antennas with uniform main beam are used in order to cover whole target extent if possible and also correction techniques are developed to compensate the antenna radiation pattern influence.

Possible phase errors lead in amplitude errors of main/side-lobes in reconstructed RCS pattern, their misalignment and undistinguished nulls between them. In case of image reconstruction by means of ISAR, individual scattering centers are predominantly misaligned and can create new false ones.

Chapter 2

State of the Art

Following chapter describes state of the art and present trends in RCS measurements focused on NF techniques and error correction methods and image processing by means of ISAR. First section briefly presents RCS definition. Next sections deal with measurement principles, used waveforms and techniques employed in FF and NF regimes. Selected circular NF to FF method is thoroughly described. Following section is then dedicated to errors occurring in both FF and NF measurements, and also to their correction techniques. Finally, last part of this chapter briefly describes ISAR imaging method based on computed tomography processing. In addition, clutter minimizing technique employing statistical method Principal Component Analysis (PCA) is introduced.

Presented RCS state of the art and described techniques are closely related to this thesis.

2.1 RCS Definition

The electromagnetic scattering properties of objects became important after invention of the radar in early 1940'. However, in 1900, Nicola Tesla proposed that electromagnetic waves reflections could be used to detect metallic objects. In 1908, Gustav Mie published a paper [19], where he outlined computation of light scattering by small spherical particles using Maxwell's electromagnetic theory. The first "target" was localized by american electrical engineers Albert H. Taylor and Leo C. Young of the Naval Research Laboratory (USA) in 1922, when the wooden boat accidentally interfered with their continuous wave (CW) signals. Thirteen years later Robert Watson-Watt suggested that radio waves might be used to detect aircraft at a distance. Since then, an intensive research has begun in the field of radar systems and targets localization. In the early 1950s, members of Britain's Royal Aircraft Establishment (RAE) at Farnborough started looking at so called "radar echoing area". The term Radar Cross Section has come into use later. Further experimental work in the field of radar design and RCS measurements together with analytic efforts helped to increase the understanding of scattering mechanisms; [20].

The backscattering of the target is a complex phenomenon since total backscattered field is formed from individual reflections of the scattering centers, representing reflective parts of target with their scattering mechanisms. The most significant parts of backscattered field of common target are specular reflection from the flat surfaces oriented perpendicularly to the receive antenna and reflections from the corners. The other contributions state for edges and tips diffraction, creeping waves and resonant parts sources. The distribution of overall scattered field, as well as its polarization, changes with orientation of the target according to radar and depends on polarizations of transmit (Tx) and receive (Rx) antennas, that may be arbitrary in the general case. The incident wave with certain polarization excites currents in the target which re-radiate in a scattered wave in all directions with generally non-specified polarization. From the theory, this reflected wave can be broken down into two orthogonal linearly polarized parts. In most radar systems, linear Tx/Rx antennas are employed and therefore only co-polarized part of the reflected wave is received. This amount of energy actually characterizes the RCS.

Known RCS of a target σ, among other parameters, that mainly characterize radar system, determines range R between the target and radar. It is described by well known radar equation, see Eq. (2.1). Here, λ is wavelength of radar system. P_r and P_t stand for power received and transmitted by antennas with gains G_{tx} and G_{rx} respectively, measured at detector/generator terminals. Constant L then represents losses in the system (cable, polarization losses, impedance mismatch etc.), [21].

$$R = \sqrt[4]{\frac{P_t G_{tx} G_{rx} \lambda^2}{P_r L (4\pi)^3} \sigma} \tag{2.1}$$

However, RCS is formally defined as a power density scattered in specified direction (θ, ϕ) obtained at the receive antenna S_r normalized to incident plane wave at the target S_i in specified direction. Its mathematical expression is stated in Eq. (2.2). The definition can be also described as a projected area of a substituted electrically large metal sphere which would return the same echo signal as a given target.

$$\sigma = \lim_{R \to \infty} 4\pi R^2 \frac{|S_r(f, \theta, \phi)|^2}{|S_i(f, \theta, \phi)|^2} \tag{2.2}$$

The limit in Eq. (2.2) ensures plane wave propagation of both, incident and scattered waves. An assumption inherent to the definition is mutual independence of both, target and the radar. It means that incident field at the target and also scattered field at the receive antenna are solely functions of the antenna and target. If this condition is not met or any other targets or noise signals (referred as clutter) are present, the errors occur in the measurements. These need to be eliminated by changing measurement technique and/or subsequent calibration of the system and data post-processing.

As it is seen from Eq. (2.2), the RCS has dimensions of area - m^2. Due to a big variation in RCS of particular objects (or across objects compared to each other), unit of RCS is therefore stated rather in logarithmic scale dBsm. It is obvious from Tab. 2.1 of maximum RCS of selected objects in X-band (8-12 GHz).

Comparing the conventional planes or bombers (i.e. B-52 invented in 1950's) with stealth aircrafts incorporating advanced stealth technologies (B-2, F-117) their

Table 2.1: RCS of selected objects in X-band, [22].

Object	RCS (m^2)	RCS (dBsm)
Car	100	20
B-52	100	20
B-1	10	10
Cabin cruiser	10	10
F-16	5	7
Mig-21	3	4.8
Man	1	0
F-18	1	0
Typhoon	0.5	-3
Tomakawk SLCM	0.05	-13
Bird	0.01	-20
F-117 Nighthawk	0.003	-25
Insect	0.001	-30
B-2	0.0001	-40

RCSs are typically multiple orders of magnitude higher, whereas stealth aircrafts can reach signatures below the RCS of birds and some big insects, see Tab. 2.1.

The Eq. (2.1) and Tab. 2.1 show that RCS of the target can dramatically change the maximum detection range. For instance, the US airborne warning and control system (AWACS) can detect target with and RCS of 7 m^2 at a range of at least 370 km. However, stealth missiles could be undetected up to 108 km. With their travel speed 805 km/h, only 8 minutes remain to locate and destroy them; [22]. From the radar point of view, mainly statistical values of targets RCS are useful whereas in the field of RCS reduction/augmentation the knowledge of precise spatial distribution of RCS as well as its frequency-dependent characteristics are important for shaping the target and radar absorbent material (RAM) usage.

As it was written earlier, RCS of each target varies differently with the change of frequency. However, three frequency regimes - Rayleigh, Mie and Fraunhofer region - are defined to describe RCS changes within wide frequency band. This behavior is valid for almost all structures and it is further described for sphere. In the case of low-frequency **Rayleigh region**, objects dimensions are considerably smaller than used wavelength of radar system and RCS is approximately proportional to fourth power of frequency (for sphere applies $\sigma = 9\pi r^2 (kr)^4$). In the second, **Mie region**, referred also as resonant, the radar wavelengths are comparable to object dimensions and therefore RCS oscillates in this region. At higher frequencies, in **Fraunhofer (or optical) region**, where wavelengths are much smaller compared to object, variations of its RCS are moderate with increasing frequency. In case of sphere, RCS is then proportional to its silhouette surface ($\sigma = \pi r^2$). Mentioned regions are depicted for RCS of sphere as it is illustrated in Fig. 2.1, where r represents its radius; [23].

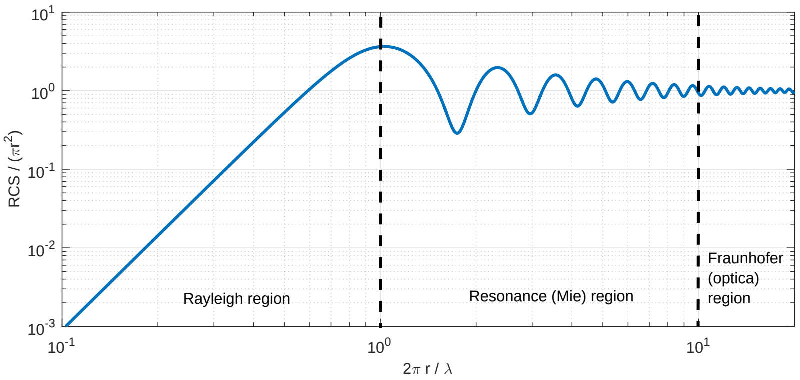

Figure 2.1: RCS of the sphere.

2.2 RCS Measurement Principles

RCS measurements, as well as test sites and instrumentation, are very closely related to measurements of antennas characteristics. Detailed antenna measurement techniques were published in many publications, i.e. [24], [25], [26]. Illuminated target acts basically as an antenna - it re-radiates the incident energy to space according to its electrical parameters and shape as well as operating frequency, direction of incident and scattered waves and according to polarization of the incident field. It means that RCS measurement is treated as antenna measurement and therefore near-fields and far-fields of the target are defined in the same manner. Following this, the same measurement techniques are employed as in the case of antennas. RCS measurement principles are summarized in the Radar Cross Section Handbook; [23].

Typical measurement system consists of generator, Tx/Rx antenna and a detector. Based on the configuration, there are two basic measurement radars: mono-static and bi-static. Comprehensive list of radar systems can be found in [28].

Mono-static system employs one antenna for transmitting and receiving signal. Resulting **mono-static RCS** is in most cases a function of target-radar orientation. Mono-static radar systems are widely used and mono-static RCS is then basic target characteristic.

In bi-static (or multi-static) case, [29], separate Tx, Rx antennas are used. Resulted **bi-static RCS** is then measured with antennas separated by a few degrees up to 180 degrees, where Tx antenna, target and Rx antenna lie in one line. It is also often stated as a function of bi-static angle (mutual angle of Tx antenna - target - Rx antenna). Compared to mono-static case, bi-static RCS of some targets can be higher for certain Tx-Rx antennas topology; [30]. It can be shown on CST simulation of RCS of metallic sphere, see Fig. 2.2. Its diameter is 10λ and it is illuminated by plane wave propagating along "z" axis (toward $z = 0$).

As it is seen, the value of bi-static RCS at angle 180° is about 30 dB higher then mono-static RCS, that is -11.5 dBsm. The principle of forward scattering of sphere was derived in 1908 by Mie; [19]. Based on Babinet's theorem, only silhouette of the target, that is seen by Rx antenna, is needed to create the same scattered field; [31]. This property is used in many bi-static passive/active radar systems, i. e. Czech radar systems Tamara, Vera; [32].

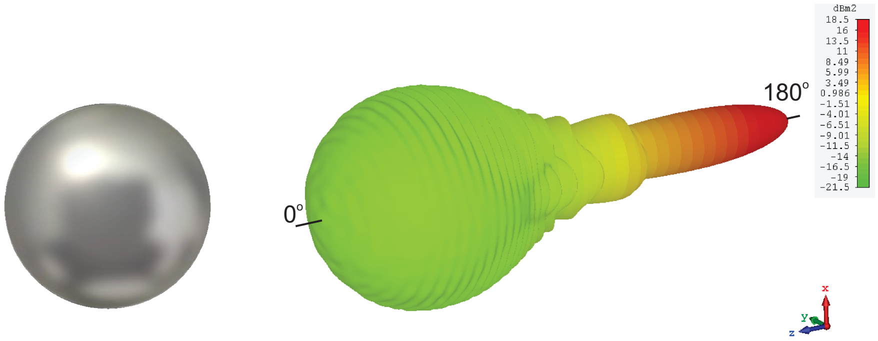

Figure 2.2: Bi-static RCS of the sphere, d = 30 cm (10λ).

In RCS measurement, in addition to amplitude and phase, also polarization of transmitted and scattered field can be utilized to describe scattering parameters of the target. In this way, target acts as a polarization transformer. Its properties can be described by 2x2 coherent scattering matrix, commonly denoted as Sinclair matrix [S], see Eq.(2.3); [33].

$$\begin{bmatrix} E_{r-V} \\ E_{r-H} \end{bmatrix} = \begin{bmatrix} S_{VV} & S_{VH} \\ S_{HV} & S_{HH} \end{bmatrix} \begin{bmatrix} E_{t-V} \\ E_{t-H} \end{bmatrix} \tag{2.3}$$

Measuring the target, received scattered field $E_{r-V,H}$ has, in general, different polarization from incident field $E_{t-V,H}$. The transform is represented by complex Sinclair scattering matrix $[S]$. Here, S_{VV} and S_{HH} are co-polarized components, whereas S_{VH} and S_{HV} state for cross-polar components. Measuring passive and static targets, cross-polar terms are identical.

The polarimetric-based measurement approaches are nearly identical to basic RCS measurement [34], [35], [36], as well as calibration techniques (based on reference object) [33], [37], background subtraction [38] etc.

2.2.1 Used Waveforms

The main purpose of RCS measurement is obtaining scattered field at certain angular extent of the target at given frequency or within defined frequency range. The operating frequency bandwidth together with used waveform determine requirements on measuring instrumentation. Basically, most used transmit signals are based on following approaches:

1. Continuous wave (CW),
2. Gated CW,
3. Frequency modulated CW,
4. Stepped frequency CW,
5. Pulsed signals.

In the first case, **CW radar** stands for basic and most simple mono-frequency radar system. Despite its impossibility to provide range information, it is still widely used as a Doppler radar in many applications, [27]. To resolve range or targets separation, a time reference of the received echo need to be known. It is achieved by modulating the transmit signal, mostly by three basic techniques, [39]:

- amplitude modulation,
- frequency modulation,
- phase modulation.

Gated CW systems represent form of CW radars, referred also as pulsed Doppler radars, where the mono-frequency signal is amplitude-modulated by On-Off keying to generate pulsed CW waveform in order to obtain range information. It combines advantages of both, pulsed and CW systems. By appropriate timing of On-Off states - pulse repetition frequency (PRF), clutter and other reflections can be separated from target reflection and only one antenna can be used for transmitting and receiving, [39].

Frequency modulation of CW (FMCW) is one of the most common technique to broaden the signal bandwidth. Carrier is often modulated by rectangular, triangular, sawtooth signals. The last mentioned is referred as chirp signal. SFCW radar has better down range resolution than other CW systems, its low-cost, mid-power and has a good immunity to interference signals; [40].

Contrary to FMCW system, **stepped frequency CW radar** (SFCW) synthesizes short pulses of wide bandwidth by step-by-step fixed frequency shifting of transmitted signal as it is depicted in Fig. 2.3.

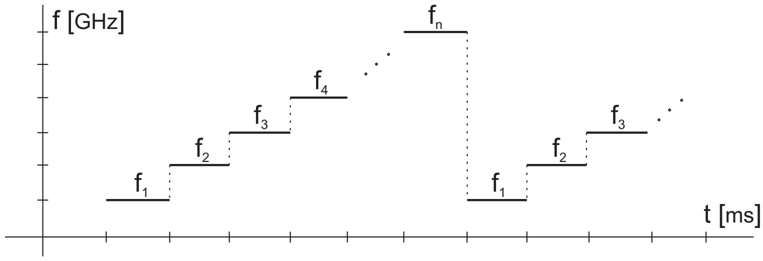

Figure 2.3: SFCW principle.

Frequency step, as well as span, is selected according to required unambiguous range and resolution, respectively. When each step signal is transmitted, received echo is coherently detected and thus the absolute phase information is obtained; [41]. From the basis of SFCW, transmitted signal has rectangular frequency spectrum and resulting TD waveform is sinc function, see Eq. (2.4).

$$\mathrm{sinc}(x) = \frac{\sin(\pi x)}{\pi x} \tag{2.4}$$

The function is defined in singular point $x = 0$ as $\mathrm{sinc}(0) = 1$. The phase difference, and consequently frequency difference Δf, between two received signal steps determines unambiguous range R_{unamb} according to Eq. (2.5); [42].

$$R_{unamb} = \frac{c}{2\Delta f} \tag{2.5}$$

Range resolution (or down-range resolution) ΔR_0 is then, using Fourier theory, dependent on used frequency bandwidth BW of transmit signal, see Eq. (2.6).

$$\Delta R_0 = \frac{c}{2BW} \tag{2.6}$$

Resulting signal from SFCW system consists of consecutive short transmitted signals with "mono-frequency" bandwidths, therefore received signal have high signal-to-noise ratio (SNR). Moreover, high transmit power can be used for long range detection and deep penetration through many materials; [41]. That is used primarily in through-wall imaging [43], hidden objects detection, landscape monitoring, [44] etc. A difficulty of SFCW system is to maintain a synchronization between transmitter and receiver. Other problem is in measurement of dynamic RCS. Doppler effect shifts the apparent distance of the target, therefore correct range cannot be resolved. In many cases, vector network analyzers (VNA) are used as SFCW radar system for RCS measurement in laboratory conditions, even proposed by R&S, Keysight; [45], [46]. Using VNA together with broadband antennas, very fine resolution can be obtained for gating or imaging purposes.

Impulse or **pulsed radar systems** employ TD pulses in order to obtain high-resolution images. Their spectrum can be extremely wideband and radar transmits and receives all the frequencies simultaneously. Such a system has therefore different architecture and also performance compared to previously described CW systems. Range resolution is the same as in case of SFCW case. However, due to inherent broad bandwidth, the dynamic range of receiver decreases as it is also difficult to design short and high-power signal.

2.2.2 Far-Field RCS Measurement

The most precise RCS determination involves measurement of the target in FF region. Incident spherical wavefront differs from plane wave along the target projection by certain phase shift $\Delta\varphi$. This phase error depends on transmitter frequency and dimension of target projection perpendicular to incident field direction D. The situation is depicted in Fig. 2.4). Difference between spherical wave and plane wave Δr at the plane of the target can be defined as in Eq. (2.7). Phase difference is then written from phase term $k\Delta r$ of the spherical wave into Eq. (2.8).

$$\Delta r = \sqrt{R^2 + \frac{D}{2}} - R \tag{2.7}$$

$$\Delta\varphi = \frac{2\pi}{\lambda}\left(\sqrt{R^2 + \frac{D}{2}} - R\right) \tag{2.8}$$

The Eq. (2.8) can be decomposed into Taylor series. Taking the first term, approximation of the phase difference is then (Eq. 2.9):

$$\Delta\varphi \approx \frac{\pi D^2}{4\lambda R} \tag{2.9}$$

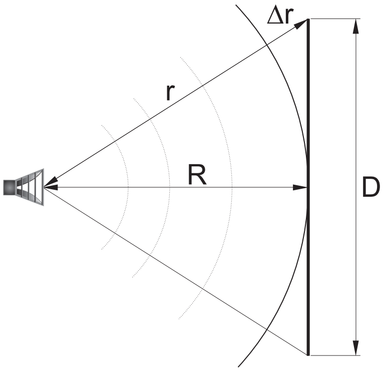

Figure 2.4: Far-field approximation.

Define maximum acceptable error $\Delta\varphi = \pi/8$ (22.5°), the well known equation of Fraunhofer's FF criteria R_{FF} is then obtained, see Eq. (2.10).

$$R_{FF} = \frac{2D^2}{\lambda} \tag{2.10}$$

For example, assume target of maximum dimension of 1 m. Resulting minimum FF range, according to Eq. (2.10) at frequency 1 GHz is 6.7 m and 66.7 m at 10 GHz. It is obvious, that mostly outdoor ranges can be used for direct unscaled FF RCS measurement. There are many ranges in US, [48] and Europe; [49].

Time and Frequency Domain Description

General FF measurement scheme, involving radar with Tx, Rx antenna and target placed in any surrounding can be depicted by Fig. 2.5. Received signal is represented as a sum of scattered field from target and other unwanted signals, mainly antennas crosstalk and reflections from background.

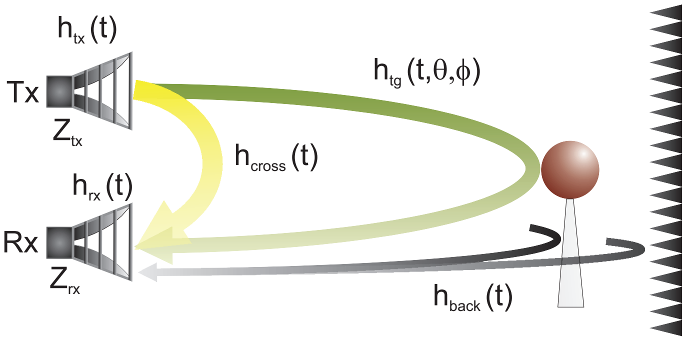

Figure 2.5: Measurement channel in TD.

It can be described by appropriate equation in both, TD (Eq. (2.11)) as an impulse response of linear, time invariant (LTI) system and also in FD (see Eq. (2.12)) representing frequency response.

$$u_{rx}(t) = \sqrt{\frac{Z_{rx}}{Z_{tx}}} \frac{\partial}{\partial t} u_{tx}(t) * h_{tx}(t, \theta_t, \phi_t) * \frac{1}{2\pi R^2 \mathrm{c}} \delta \left(t - \frac{2R}{\mathrm{c}} \right)$$
$$* \left[h_{tg}\left(t, \theta_{tg}, \phi_{tg}\right) + h_{cross}(t) + h_{back}(t, \theta_{tg}, \phi_{tg}) \right] * h_{rx}(t, \theta_r, \phi_r) \qquad (2.11)$$

$$U_{rx}(\omega) = \sqrt{\frac{Z_{rx}}{Z_{tx}}} \mathrm{j}\omega U_{tx}(\omega) H_{tx}(\omega, \theta_t, \phi_t) \frac{\mathrm{e}^{-\mathrm{j}2\omega R/\mathrm{c}}}{2\pi R^2 \mathrm{c}}$$
$$\left[H_{tg}\left(\omega, \theta_{tg}, \phi_{tg}\right) + H_{cross}(\omega) + H_{back}(\omega, \theta_{tg}, \phi_{tg}) \right] H_{rx}(\omega, \theta_r, \phi_r) \qquad (2.12)$$

The received voltage $u_{rx}(t)$ at the terminal of receive antenna is expressed essentially as a convolution of transmitted signal $u_{tx}(t)$, impulse response of antenna $h_{tx}(t, \theta_{tg}, \phi_{tg})$ (or Tx and Rx antennas in bi-static case) and response from the surrounding environment - target, crosstalk, background $h_{tg}(t, \theta, \phi) + h_{cross} + h_{back}(t)$ respectively. Derivative term (jω in FD) represents impulse differentiation by transmit antenna. It is obvious from this term, that Tx antenna cannot radiate DC component of signals (for $\omega = 0$). Dirac function convolution then stands for time retardation of the signal due to finite speed of light c, that is converted to FD as Green's function. Antenna transient response $h_{tx}(t)$ represents effective height of the antenna and describes its spatial characteristics. However, with the convolution term "$h_{tx}(t)*$" (time integration) the final unit is m; [47]. Impedance terms Z_{tx}, Z_{rx} stand for port impedances of antennas. Chanel transient response consist mainly of antennas crosstalk $h_{cross}(t)$ target response $h_{tg}(t, \theta_{tg}, \phi_{tg})$ and background $h_{back}(t, \theta_{tg}, \phi_{tg})$, that comprises all other reflections in measurement channel. First mentioned term exists only in bi-static arrangement and significantly decreases SNR. It transforms to reflection from antenna aperture in mono-static case.

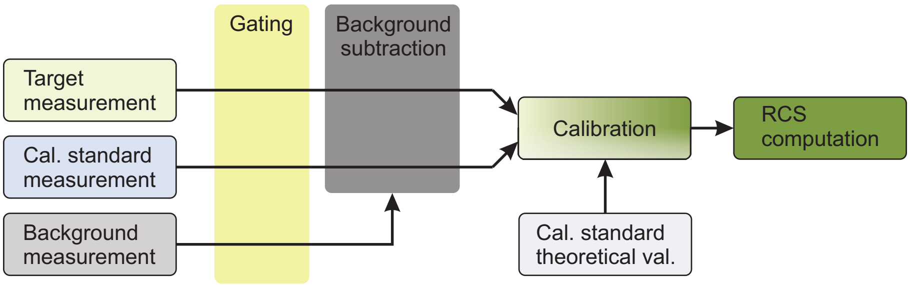

Figure 2.6: FF RCS measurement and calibration process.

As it is seen from Eq. (2.11) or (2.12), response from target can be extracted from received signal only by appropriate calibration and correction techniques. Basic and well known procedure is depicted in Fig. 2.6 and can be summarized as follows. Raw measured data need to be calibrated to obtain RCS value precise as possible. Commonly used calibration technique comprises obtaining error function of the measurement channel by additional measurement of known object that need to be analytically described. Additionally, measured signals can be time-gated in TD in order to suppress more distant reflections and antennas crosstalk. Furthermore, measured background (without target) can be subtracted from received signal. More detailed description of errors and correction techniques will be described later in next chapter.

2.2.3 Near-Field RCS Measurement

So far only direct method to obtain FF RCS pattern has been taken into account, where the incident field is assumed to be a plane wave at the target as well at the antenna. However, there are indirect methods whereby RCS of the target can be synthesized from cylindrical or spherical near-field backscattered from the target. Based on equivalence principle, [24], FF pattern can be calculated from field (i.e. E field) distributed on surface close to target. In praxis, E field is measured in discrete positions to provide approximative FF pattern. There are three basic scanning techniques adopted from antennas radiation pattern measurement utilized for NF RCS measurements: planar, cylindrical and spherical, see Fig. 2.7. These geometries are preferred since convenient positioning systems are employed and furthermore, the complex vector data are collected on the well-described surfaces.

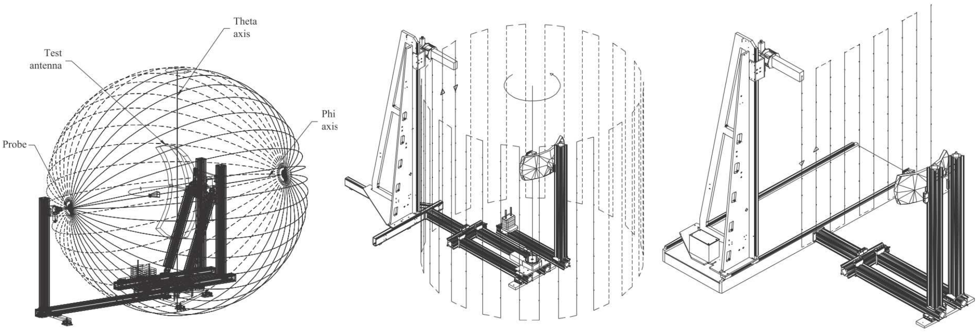

Figure 2.7: Spherical, cylindrical and planar NF measurement geometries; [26].

However, NF measurement at discrete positions over finite surface, defined by measuring geometry, introduces field truncation error, that can result in errors in FF approximation. Appropriate scanning system should be therefore used regarding to measured targets geometry and anticipated RCS pattern.

Measuring antenna (referred as probe in NF measurements) also influences resulting FF RCS due to its mutual coupling with target. Antenna illuminates the target non-uniformly depending on its radiation pattern and multiple reflection between target and antenna aperture can occur. Therefore, there are requirements on antennas characteristics, that are basically: mechanical rigidity, small aperture, low RCS, wide-band operation, low directivity (wide beamwidth), pure polarization, small return loss and high front-to-back ratio. Based on mentioned parameters, rectangular or cylindrical open-ended waveguides, pyramidal or cylindrical horns, corrugated and double ridge horns are frequently used.

Near-field RCS measurement and calibration process differs from FF one because both, amplitude and phase is collected over the surface enclosing target and therefore more steps are necessary to recover estimated FF pattern, see Fig. 2.8.

As in case of FF measurement, gating and background subtraction can be performed in NF case. However, phase measurement introduces other error sources, as imperfect mechanical moving parts with tolerances (positioning mechanism, target fixture, etc.), antenna effects, finite sampling steps and restricted scanning surface. Practically, it is not possible to correct all the errors concerning NF measurement and some approximations are assumed:

- mechanical system is stable,
- field out of scanning surface is negligible or zero,
- multiple reflections between antenna and target do not exist,
- processing techniques do not add errors caused by additional truncation, rounding,
- multiple reflections can be separated from target response by appropriate gating.

These approximations can be applied when related errors are accurately predicted and minimized.

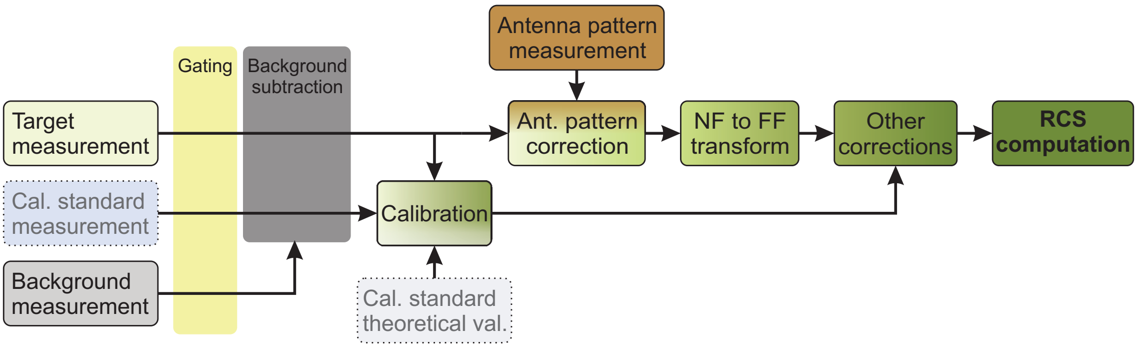

Figure 2.8: Basic NF RCS measurement and calibration process.

Basic NF processing technique comprises, according to Fig. 2.8, NF data correction by means of measured response from measuring antenna, subsequent NF to FF transform (combining FFT and IFFT data transformations) and final corrections and level equalization; [24], [26].

For the purpose of this work, cylindrical measurement technique is described in next part.

Cylindrical Near-field Measurement

Cylindrical NF scan, contrary to spherical and planar systems, utilizes rotational movement of the target and vertical movement of scanning antenna to collect NF data over cylinder enclosing the target.

Assuming ideal case (no other reflections are present, ideal infinitesimal probe is used), electric field component in FF $\vec{E}(R,\theta,\phi)$ can be described, according to Huygens principle, as a superposition of the cylindrical wave functions; [56]. Utilizing the method of stationary phase, FF formula in spherical coordinate system (R,θ,ϕ) has the following form, see Eq. (2.13); [55]. Magnetic component of FF field can be accordingly evaluated as in Eq. (2.14), where Z_0 denotes free space impedance.

$$\vec{E}(R,\theta,\phi) \approx \frac{-2k\sin(\theta)\mathrm{e}^{\mathrm{j}kR}}{R} \sum_{n=-\infty}^{\infty} \mathrm{j}^n \mathrm{e}^{\mathrm{j}n\phi} \left[\mathrm{j}A_n(k\cos(\theta))\hat{\boldsymbol{\phi}} + B_n(k\cos(\theta))\hat{\boldsymbol{\theta}}\right] \qquad (2.13)$$

$$\vec{H}(R,\theta,\phi) = \frac{\hat{\boldsymbol{r}} \times \vec{E}}{Z_0} \tag{2.14}$$

Here, k stands for wavenumber and $\hat{\boldsymbol{\phi}}$, $\hat{\boldsymbol{\theta}}$ represent unit vectors of spherical coordinates. Cylindrical spectral expansion components $A_n(k_z)$ and $B_n(k_z)$ are then evaluated in terms of tangential electric fields E_ϕ and E_z measured on the scan cylinder as Eq. (2.16) and (2.17).

$$A_n(k_z) = -\frac{1}{4\pi^2 k_a \frac{\partial}{\partial(k_a a)} H_n^{(1)}(k_a a)} \iint\limits_{-z_0\ 0}^{z_0\ 2\pi} E_\phi(a,\phi,z)\mathrm{e}^{-\mathrm{j}n\phi}\mathrm{e}^{-\mathrm{j}k_z z}\mathrm{d}\phi\mathrm{d}z \tag{2.15}$$

$$- \frac{nk_z}{4\pi^2 a k_a^3 \frac{\partial}{\partial(k_a a)} H_n^{(1)}(k_a a)} \iint\limits_{-z_0\ 0}^{z_0\ 2\pi} E_z(a,\phi,z)\mathrm{e}^{-\mathrm{j}n\phi}\mathrm{e}^{-\mathrm{j}k_z z}\mathrm{d}\phi\mathrm{d}z \tag{2.16}$$

$$B_n(k_z) = \frac{k}{4\pi^2 k_a^2 H_n^{(1)}(k_a a)} \iint\limits_{-z_0\ 0}^{z_0\ 2\pi} E_z(a,\phi,z)\mathrm{e}^{-\mathrm{j}n\phi}\mathrm{e}^{-\mathrm{j}k_z z}\mathrm{d}\phi\mathrm{d}z \tag{2.17}$$

In both equations, $H_n^{(1)}(k_a a)$ is Hankel function of the first kind and n-th order. Wavenumber component k_a, where a represents radius of cylinder, is evaluated as:

$$k_a = \sqrt{k^2 - k_z^2} \tag{2.18}$$

It can be shown, that A_n and B_n are independent of constant a, even though it appears in both expressions; [55]. Furthermore, by evaluating modal coefficient A_n for magnetic field, that has similar single-term form as electric coefficient B_n, both terms can be computed only from electric and magnetic components oriented in z direction.

In practice, scan cylinder has finite extent, thus the limits of integrals in Eq. (2.16) and (2.17) are truncated to $(-z_0,\ z_0)$. Similarly to planar scanning, sample spacing in vertical Δz and azimuthal $\Delta\phi$ direction is determined from the maximum value of their spatial harmonics k_z and k_ϕ, see Eq. (2.19) and (2.20) respectively.

$$\Delta z = \frac{\lambda}{2} \tag{2.19}$$

$$\Delta\phi = \frac{\lambda_{min}}{2a_{min}} \tag{2.20}$$

Constant a_{min} denotes minimum radius of cylinder enclosing the target and λ_{min} is minimum wavelength corresponding to highest frequency of used bandwidth.

Besides previously described basic cylindrical scan, other measuring systems has been developed based on this technique, i.e. spiral scanning [57], [58] or even one-plane circular scanning that reduces number of vertical probe positions to only one. It eliminates errors arisen mostly from cable movement and probe position. On the other hand, it brings a restrictions especially to vertical dimension of targets under test. As a relatively simple method that appears to be suitable for FF test ranges, it will be thoroughly described in next section.

2.3 Circular NF to FF Transformation

In comparison to NF antennas radiation pattern measurements, NF scattering measurement and RCS prediction techniques are more complex because target scattering pattern depends, above all, on its shape and physical properties. Obtaining the exact FF RCS from NF data involves, according to equivalence principle, a knowledge of the field on surface enclosing the target. Theoretically, from scattering point of view, transmit and receive antenna need to scan continuously and independently the whole surface. It is practically unfeasible thus some limitation need to be taken into account instead. Besides sampling the surface, measurement techniques have been adopted and used from NF antenna measurements such as spherical, cylindrical and planar techniques.

Besides these measurement methods, NF RCS can be determined also from single-plane measurement, considering additional restrictions.

LaHaie [59] proposed image-based measurement technique and NF-FF transformation that involves both, cylindrical and only one-plain measurement in the NF of the target. This circular NF-FF transformation (CNFFFT) prediction method is based on Synthetic Aperture Radar (SAR) or inverse SAR (ISAR) data processing used for obtaining "focused" radar image of target under test. Nevertheless, presented method does not require image reconstruction in order to obtain FF RCS approximation. CNFFFT is based on single-scattering model that means the target is composed of isotropically radiating mutual-independent elements. Therefore only small or negligible interactions between two or more separated points on the target are taken into account. This is main disadvantage of this method that can lead to some misalignment of the sidelobes and nulls in reconstructed RCS (in comparison to exact FF RCS) when multiple interactions (such as multiple reflections, traveling and creeping waves) become the main part of the overall scattering.

Another restriction concerns to the target dimensions. One-plain measurement is conditioned by limited vertical size of the target (in order of tens of λ), which should meets the far field condition and/or whose major part of back-scattered field is in direction of the receive antenna and is negligible in other directions. The situation is depicted in Fig. 2.9.

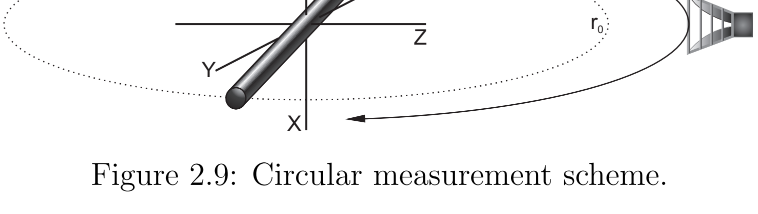

Figure 2.9: Circular measurement scheme.

From the radar point of view, broadband measuring system need to be employed in order to obtain range-dependent reflectivity data with required down-range resolution ΔR and perform range-frequency Fourier transform.

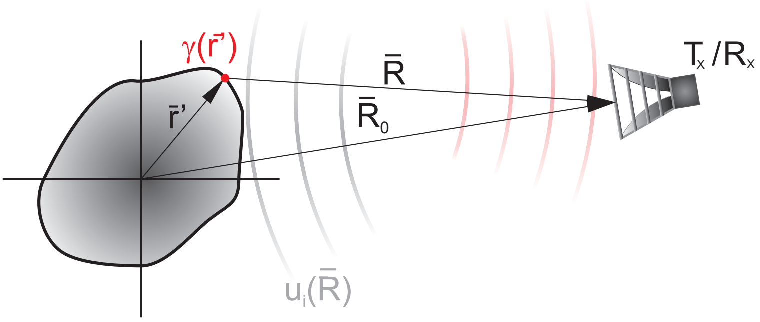

Figure 2.10: Geometry of 1D NF measurement setup.

The above mentioned transformation technique is derived from the target radar reflectivity distribution $u_r'(\vec{R}_0, k)$, see Eq. (2.21). According to Fig. 2.10, it describes two-way response of some scattering center $\gamma(\vec{r}')$ on the target at a distance R (Eq. (2.22)) from the observation point. Incident field $u_i(\vec{R}, k)$ impacting the target can be then written as a multiplication of Green's function and unit power, Eq. (2.23). Positive exponential terms denote incoming waves to the target and to the receiver, respectively.

$$u_r'\left(\vec{R}, k\right) = \gamma\left(\vec{r}'\right) u_i \frac{\mathrm{e}^{\mathrm{j}kR}}{4\pi R} \tag{2.21}$$

$$R = \left|\vec{R}_0 - \vec{r}'\right| \tag{2.22}$$

$$u_i\left(\vec{R}, k\right) = \frac{\mathrm{e}^{\mathrm{j}kR}}{4\pi R} \tag{2.23}$$

Total scattered field from the target in direction $\vec{R}_0$ collected by receive antenna in near field is thus described as an integral of reflectivity distribution over the whole target, see Eq. (2.24). Since the target is scanned in one plane, Eq. (2.24) can be rewritten in the polar coordinates as Eq. (2.25), where angle ϕ denotes turn of the receiver antenna with respect to coordinate system of target, whereas ϕ' is azimuthal angle between the position vector $\vec{r}'$ and coordinate system. Constant r_{tg} then represents smallest circle enclosing target extent. For the sake of clarity, integrals boundaries will be omitted in further equations.

$$u_r\left(\vec{R}_0, k\right) = \iiint\limits_V \gamma\left(\vec{r}'\right) \frac{\mathrm{e}^{\mathrm{j}2kR}}{\left(4\pi R\right)^2} \mathrm{d}^3\vec{r}' \tag{2.24}$$

$$u_r\left(\phi, k\right) = \int\limits_0^{r_{tg}} \int\limits_0^{2\pi} \gamma\left(r', \phi'\right) \frac{\mathrm{e}^{\mathrm{j}2kR}}{\left(4\pi R\right)^2} r' \mathrm{d}\phi' \mathrm{d}r' \tag{2.25}$$

The angular echo signal received in far field $u_r^{FF}\left(\phi, k\right)$, corresponding to Eq. (2.25), is formed from plane-wave reflections and basically depends only on relative angles $\phi - \phi'$ and phase differences, see Eq. (2.26). From the FF point of view there is no need to know the whole phase history to form the pattern and thus only relative change of phase is sufficient. It is expressed by projection of the position vector $\vec{r}'$ of the given scattering center into the direction of the receiver, represented by unit vector $\hat{R}_0$, see Eq. (2.27).

$$u_r^{FF}(\phi, k) = \iint \gamma(r', \phi')\, \mathrm{e}^{j2kr'\cos(\phi-\phi')} r' \mathrm{d}\phi' \mathrm{d}r' \tag{2.26}$$

$$\cos(\phi - \phi') = \vec{r}'\hat{R}_0 \tag{2.27}$$

By comparing the relations Eq. (2.25) and Eq. (2.26), the FF scattering pattern can be obtained from NF pattern by transforming the range factor from Eq. (2.22) to Eq. (2.27). Practically some extrapolating technique needs to be used; [60].

According to [61], the presented extrapolation technique firstly transforms measured data, described by two-way spherical wave function (2.25), to the form of cylindrically propagating wave and subsequently to plane-wave field. In the first case, partial derivative of Eq. (2.25) is performed with respect to k. Rearranging the result, differentiated NF pattern can be written as Eq. (2.28). The last term of the integral represents in fact the asymptotic expansion of zero-order ($\nu = 0$) Hankel function for large arguments z Eq. (2.29) describing incoming cylindrical wave; [62]. It is derived from general definition Eq. (2.30) considering identity $e^{-j\frac{\pi}{4}} = \dfrac{1}{\sqrt{j}}$.

$$\frac{\partial u_r(\phi, k)}{\partial k} = \mathrm{j} \iint \frac{1}{8}\sqrt{\frac{\mathrm{j}k}{\pi R}} \gamma(r', \phi') \sqrt{\frac{2}{\mathrm{j}2\pi k R}} \mathrm{e}^{\mathrm{j}2kR} r' \mathrm{d}\phi' \mathrm{d}r' \tag{2.28}$$

$$H_0^1(2kR) \approx \sqrt{\frac{2}{\mathrm{j}2\pi k R}} \mathrm{e}^{\mathrm{j}2kR} \tag{2.29}$$

$$H_\nu^{(1)}(z) \approx \sqrt{\frac{2}{\pi z}} \mathrm{e}^{\mathrm{j}(z - \frac{\pi}{2}\nu - \frac{\pi}{4})} \tag{2.30}$$

Thus, the Eq. (2.28) takes form of Eq. (2.31). The range factor R in amplitude term can be reduced to R_0 supposing negligible variation of $\vec{r}'$ in FF approximation.

$$\frac{\partial u_r(\phi, k)}{\partial k} \approx \frac{\mathrm{j}}{8}\sqrt{\frac{\mathrm{j}k}{\pi R_0}} \iint \gamma(r', \phi')\, H_0^1(2kR) r' \mathrm{d}\phi' \mathrm{d}r' \tag{2.31}$$

However, for practical purposes, numerical differentiation can be overcome by means of duality principle of Fourier transform $\mathscr{F}\{\}$ as follows, see Eq. (2.32):

$$\frac{\partial u_r(\phi, k)}{\partial k} \to \frac{\mathrm{j}}{2\pi} \mathscr{F}^{-1}\{R U_r(\phi, R)\} \tag{2.32}$$

Here, Fourier transform of differentiated $u(\phi, k)$ equals to Fourier image of $u(\phi, k)$ multiplied by the range factor R. Following this technique, NF data measured in TD are then directly weighted by R and transformed to frequency-dependent data using FT. In the case of SFCW radar, data need to be transformed to TD first. This process is outlined in Eq. (2.33).

$$\frac{\partial u_r(\phi,k)}{\partial k} = u_r^{NF}(\phi,k) = \int R\,\mathrm{e}^{\mathrm{j}2kR}\int u_r(\phi,k)\,\mathrm{e}^{-\mathrm{j}2kR}\mathrm{d}k\mathrm{d}R \tag{2.33}$$

Furthermore, more accurate results are obtained when the weight factor R is replaced by $R^{3/2}$ referring to [61]. The preprocessed data are finally written as Eq. (2.34):

$$u_r^{NF}(\phi,k) \approx \mathscr{F}\left\{R^{3/2}\mathscr{F}^{-1}\left\{u_r(\phi,k)\right\}\right\} \tag{2.34}$$

Next, the pre-processed data, Eq. (2.31), need to be extrapolated to the FF. Rewriting the Hankel function $H_0^{(1)}(2kR)$ to series according to Graf's addition theorem, Eq. (2.35), Eq. (2.31) can be write as a linear combination of Hankel and Bessel function, see Eq. (2.36).

In the explicit version of Graf's addition theorem, Eq. (2.35), [62], the $\mathbf{O}_j = (r_j, \vartheta_j)$ and $\mathbf{O}_k = (r_k, \vartheta_k)$ denote polar coordinates and (R_{jk}, ϑ_{jk}) are coordinates of $\mathbf{O}_k$ with respect to $\mathbf{O}_l$.

$$H_\nu^{(1)}(\eta r_k)\mathrm{e}^{\mathrm{j}\nu(\vartheta_k-\vartheta_{kl})} = \sum_{\mu=-\infty}^{\infty} H_{\nu+\mu}^{(1)}(\eta R_{kl})J_\mu(\eta r_l)\mathrm{e}^{\mathrm{j}\mu(\pi-\vartheta_l+\vartheta_{kl})} \tag{2.35}$$

$$u_r^{NF}(\phi,k) = \frac{1}{4}\sqrt{\frac{\mathrm{j}\pi k}{R_0}}\iint \gamma(r',\phi')\sum_{n=-\infty}^{\infty} H_n^{(1)}(2kR_0)J_n(2kr')\mathrm{e}^{\mathrm{j}n(\phi-\phi')}r'\mathrm{d}\phi'\mathrm{d}r' \tag{2.36}$$

On the other hand, The FF plane-wave data expressed by Eq. (2.26) can be also defined as a series of cylindrical waves by means of Jacobi-Anger Expansion Eq. (2.37), see Eq. (2.38); [62], [63].

$$\mathrm{e}^{\mathrm{j}2kr'\cos(\phi-\phi')} = \sum_{n=-\infty}^{\infty}(-\mathrm{j})^n J_n(2kr')\mathrm{e}^{\mathrm{j}n(\phi-\phi')} \tag{2.37}$$

$$u^{FF}(\phi,k) = \frac{1}{2\pi}\iint \gamma(r',\phi')\sum_{n=-\infty}^{\infty} J_n(2kr')\mathrm{e}^{\mathrm{j}n(\phi-\phi')}r'\mathrm{d}\phi'\mathrm{d}r' \tag{2.38}$$

Expansion relations, stated in Eq. (2.35) and Eq. (2.37), allow to relate NF and FF patterns from Eq. (2.36) and (2.38) through common periodic term $S_n(\phi,k)$ defined on interval $(0,2\pi)$ representing coefficients of generalized Fourier series of target image,[64], Eq. (2.39), depending only on angle ϕ and not on measurement distance.

$$S_n(\phi,k) = \iint \gamma(r',\phi')\,J_n(2kr')\mathrm{e}^{-\mathrm{j}n\phi'}r'\mathrm{d}\phi'\mathrm{d}r' \tag{2.39}$$

By rearranging the S_n to the form of Eq. (2.40), final FF scattering pattern S^{FF} can be expressed directly from NF pattern, see Eq. (2.41).

$$\frac{1}{4}\sqrt{\frac{\mathrm{j}\pi k}{R_0}}H_n^{(1)}(2kR_0)S_n(\phi,k) = \frac{1}{2\pi}\int_0^{2\pi} u^{NF}(\phi,k)\,\mathrm{e}^{-\mathrm{j}n\phi}\mathrm{d}\phi \tag{2.40}$$

$$S^{FF}(\phi,k)=\frac{1}{2}\sqrt{\frac{R_0}{\mathrm{j}\pi k}}\sum_{n=-\infty}^{\infty}\frac{(-\mathrm{j})^n\,\mathrm{e}^{\mathrm{j}n\phi}}{H_n^{(1)}(2kR_0)}\int_0^{2\pi}u_r^{NF}(\phi,k)\,\mathrm{e}^{-\mathrm{j}n\phi}d\phi \tag{2.41}$$

Integral of u^{NF} is periodic function and it is able to calculate it using Fourier transform. The result then takes the form of angular harmonics U_r^{NF} of u_r^{NF}.

$$\int_0^{2\pi}u_r^{NF}(\phi,k)\,\mathrm{e}^{-\mathrm{j}n\phi}d\phi=\mathscr{F}\left\{u_r^{NF}(\phi,k)\right\}\big|_{\phi}=U_r^{NF}(n,k) \tag{2.42}$$

According to Eq. (2.43) FF pattern S^{FF} is actually sum of angular harmonic weighted by filter function.

$$S^{FF}(\phi,k)=\frac{1}{4}\sqrt{\frac{R_0}{\mathrm{j}\pi k}}\sum_{n=-N}^{N}\frac{(-\mathrm{j})^n}{H_n^{(1)}(2kR_0)}U_r^{NF}(n,k)\,\mathrm{e}^{\mathrm{j}n\phi} \tag{2.43}$$

In addition, infinite series have to be truncated with respect to maximum harmonics N needed for FF reconstruction. The improved expression for the number of modes are given in Eq. (2.44); [65]. Here, constant r_{tg} stands for minimum radius of the circle enclosing the target in measured plane. This limitation indirectly determines a condition for angular sampling.

$$N=\mathrm{kr_{tg}}+2.5\sqrt[3]{\mathrm{kr_{tg}}} \tag{2.44}$$

Finally, approximated RCS of target can be obtained from Eq. 2.43 as follows:

$$\sigma(\phi,k)=4\pi\left|S^{FF}(\phi,k)\right|^2 \tag{2.45}$$

2.4 Errors in RCS Evaluation

Each reflectivity measurement contains errors that limit accuracy of the target RCS evaluation. These errors are caused mainly by characteristics of the particular components of whole measurement path - used test equipment, test range and the target. The complexity of overall system and associated measurement procedures make the description of all possible errors very difficult. In case of FF measurements, most of errors affect both, relative and absolute amplitude of resulting RCS patterns and can be deduced from a chart of relative power levels of overall transmission path between antenna and target, as it is depicted in Fig. 2.11, [66].

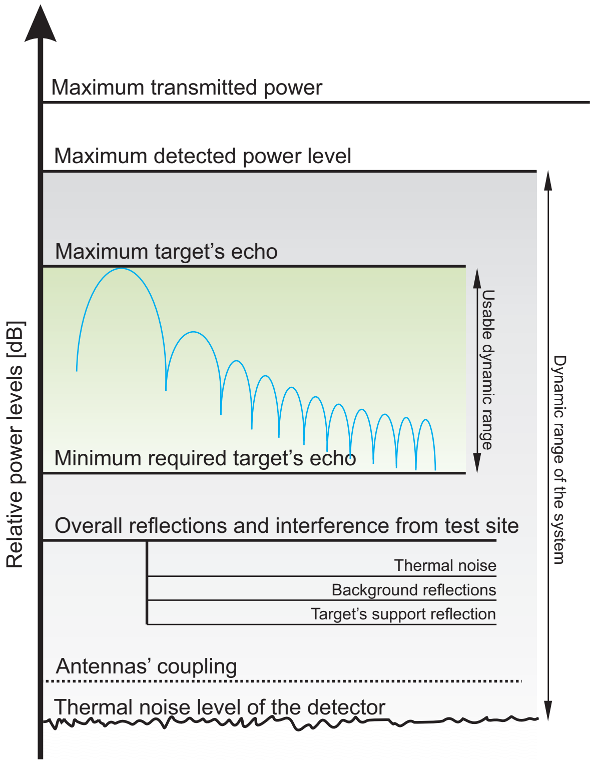

Figure 2.11: Relative power levels of the transmission path.

The dynamic range of the system is limited at the lowest detectable power by the receiver thermal noise and by its saturation at the maximum allowed power. This range is determined by used instrumentation. Using the bi-static radar (or separated transmitter and receiver), the lower detectable power can be higher than thermal noise level due to coupling of the antennas. However, another factors must be taken into account, as reflections from the ground, target support, another objects surrounding the target etc., that narrow dynamic range. Within this range there is "usable dynamic range" bounded by maximum target reflection and minimum usable reflection required for the RCS calculation.

Possible errors then arise since some power level exceeds the responses (min., max.) of usable dynamic range. Most of them state for coherent errors that cannot be eliminated by the increase of transmitted power. This can only improve signal to noise ratio. In many cases high antennas coupling, overall additional reflections and interferences, stand for most errors in FF RCS measurements.

Besides these facts that affecting accuracy of calculated RCS from FF measurements, there are also phase and amplitude errors typical in NF measurements, arisen from spherical waveforms of the radiated field.

2.4.1 NF Measurement Errors

Radar cross section of any target is defined as a ratio of the power scattered by the target surface in some direction and amount of incident power. From its definition, range between the target and radar goes to infinity that ensures the plane wavefronts of both, incident field at the target and scattered field at the receive antenna. It follows that the target and measuring antennas are mutually independent. Practically the range is truncated depending on test facility. Due to a spherical wave propagation, intensity of radiated field decays with increasing distance and therefore each part of target is illuminated by different amount of power and nonuniform phase. This power distribution also depends on the radiation pattern of the transmit antenna. Amplitude and phase variation (A, φ) of incident electric field can be described as a ratio of field at the end of target $E^i(L/2)$ and field at its center (2.46):

$$A\mathrm{e}^{-\mathrm{j}\varphi} = \frac{E^i(L/2)}{E^i(0)} \tag{2.46}$$

Assuming size of the antenna is relatively small compared to target, the change of relative amplitude A and phase φ are function of frequency, largest dimension of the target, its positioning and distance to receive antenna, see Eq. (2.47) and Eq. (2.48).

$$A = A(f, L, R, \theta) \tag{2.47}$$

$$\varphi = \varphi(f, L, R, \theta) \tag{2.48}$$

Simplified measurement scenario is depicted in Fig. 2.12. Monostatic radar is located at distance R from the target, which has dimensions L and D and it is turned by angle θ with respect to Tx/Rx antenna.

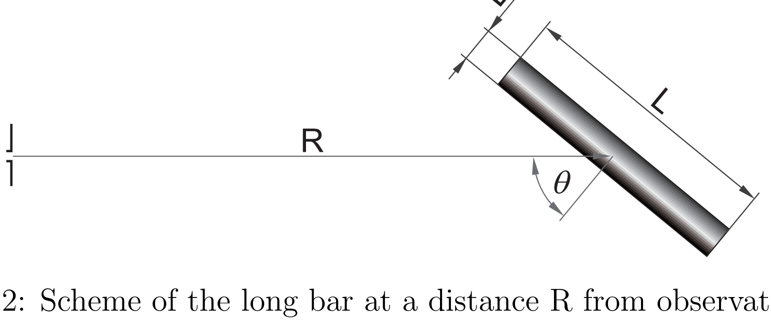

Figure 2.12: Scheme of the long bar at a distance R from observation point.

Incident spherical wavefront differs from plane wave along the target projection by certain phase shift. Maximum acceptable error (22.5° or $\lambda/16$) is given by the FF criteria (2.10) as it is defined in Section 2.1.

For example, phase error effect can be illustrated by the simulation of RCS calculated from the field obtained at different distances from the target. According to Fig. 2.12, electrically long, thin, conducting bar of length L and infinitesimal diameter D is located at a variable distance R from observation point. The target is rotated by angle θ. Its RCS can be then approximated by following expression (2.49); [23].

$$\sigma = pCL^2|F(T_1) + F(T_2)|^2 \tag{2.49}$$

In this equation, C stands for constant representing i.e. properties of the measuring system, p is multiplication factor of FF distance defined in (2.10) and $F(T)$ is a Fresnel integral (Eq. (2.50)) of an argument T stated in Eq. (2.51). Integral can be evaluated by means of its approximative expression, described i.e. in [67] and [68].

$$F(x) = \int_0^x \mathrm{e}^{\mathrm{j}\pi t^2/2}\mathrm{d}t \tag{2.50}$$

$$T_{1,2} = \frac{1}{2\sqrt{\mathrm{p}}} \pm 4\sqrt{\mathrm{p}}\frac{L}{\lambda}\sin\theta \tag{2.51}$$

NF phenomenon is demonstrated using Matlab simulation and implemented Fresnel integral calculation. RCS of the thin, 23λ long bar, modeled as perfectly electric conductor (PEC) object, is calculated from field distribution at distances that vary from $0.1R_{FF}$ to $50R_{FF}$ of actual FF range within azimuthal angles 0°−10°. Resulting figure is depicted in Fig. 2.13.

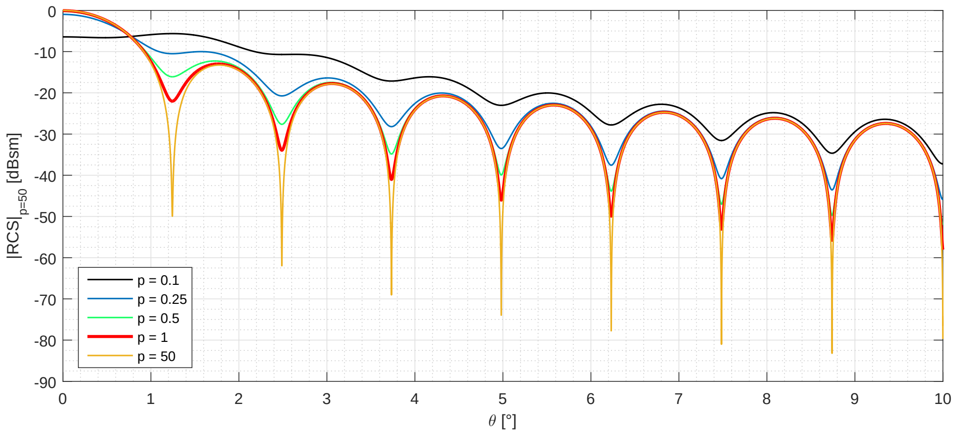

Figure 2.13: RCS simulation of the PEC bar by means of Fresnel integral - Matlab.

All the characteristics are normalized to maximum value of RCS simulated for $p = 50$. Red line represents RCS calculated from data obtained at distance that satisfies plane wave approximation condition according to Eq. (2.10). For very short distances (below $0.25R_{FF}$ in this case) the main beam is suppressed and the sidelobes are slightly misaligned in comparison to them satisfying FF criteria. On the other hand, nulls in the patterns get bigger with increasing distance pR_{FF}. Theoretically, for $p = \infty$ the nulls will tend also to infinity.

To validate correctness of this approximation a FEKO simulation has been carried out for the same setup described above. Results from both simulations show very good agreement and differ less than 0.1 dB for all given distances within whole angular range. The comparison is shown on the zoomed Fig. 2.14.

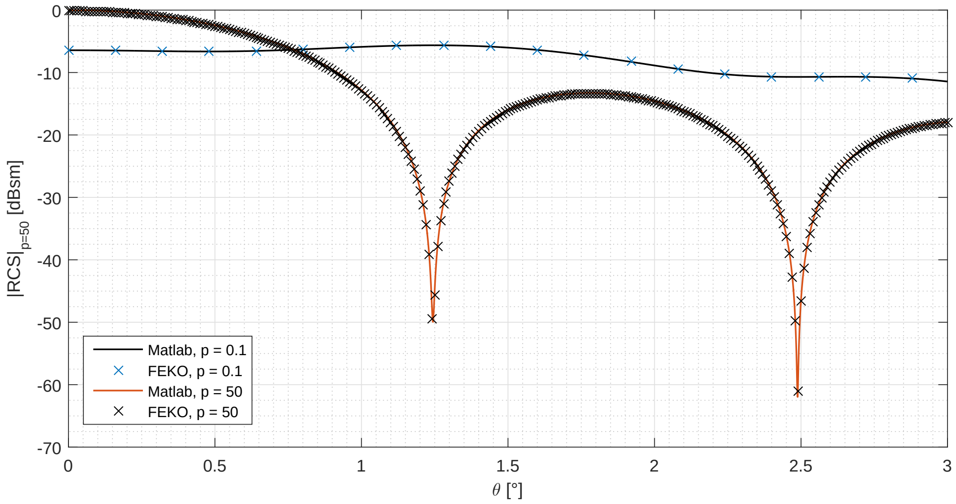

Figure 2.14: Comparison of RCS simulated by Matlab and FEKO.

It is obvious, that the NF measurements can affect significantly RCS pattern. Fig. 2.15 illustrates absolute amplitude error of NF RCS patterns related to FF one ($p = 50$). In the case of main- and side-lobes, it varies from 6.5 dB to 0.2 dB within NF ranges from $0.1R_{FF}$ to $1R_{FF}$. Long distances (or larger values of p) are required for accurate determination of the nulls, however, it is not essential in most RCS measurements.

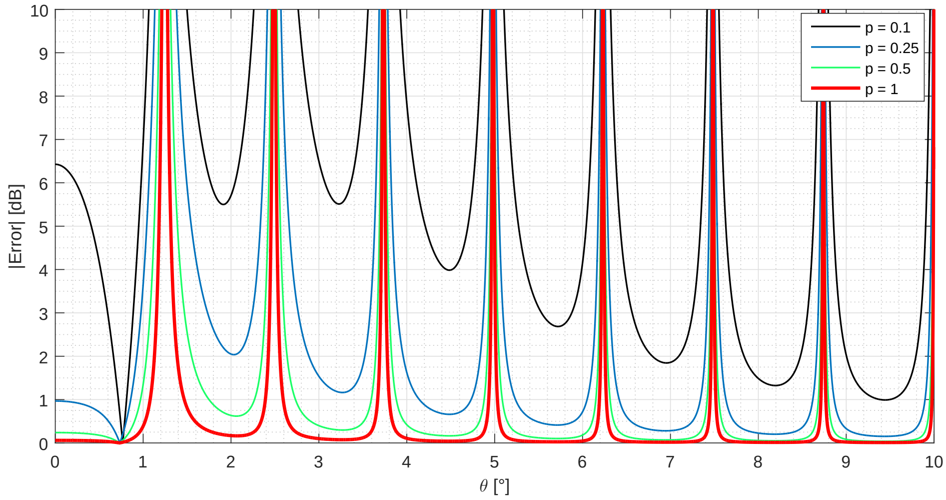

Figure 2.15: Error in Matlab RCS simulation of the PEC bar for distances $0.1R_{FF}$ - $1R_{FF}$.

2.5 Basic Error Suppression Techniques

Based on previously enumerated errors, related to measurement and calculation of RCS patterns from FF and NF ranges, common and frequently used correction techniques will be described further in both, frequency and time domains.

2.5.1 Time Gating (Windowing)

Assume SFCW scattering measurement performed by VNA within wide frequency range with sufficient number of frequency components, as depicted in Fig. 2.5. Due to different distances of discontinuities in measurement channel (instrumentation connections, antenna-free space transitions, target and surrounding objects in measurement path, etc.) to the reference plane of VNA, associated reflections arrive at the test port at different times and they can thus be measured separately to each other in TD representation of received signal. Reflection from the target can be distinguished from other unwanted reflections located in its vicinity depending on TD resolution.

Aforementioned clutter reflections can be filtered out from the signal by means of time gating (or windowing), that can be implemented in either hardware or software. However, it is obvious that these reflections, situated very close to target response (or they are even added to this response), cannot be eliminated by gating process.

Mathematically, gating is in TD represented as a multiplication of received signal $u_{rx}(t)$ with appropriate windowing function $w(t)$, whereas in FD frequency responses are convolved, see Eq. (2.52).

$$u_{rx}^{gated}(t) = u_{rx}w\left(t\right) \overset{\mathscr{F}\{\}}{\longleftrightarrow} U_{rx}^{gated}(\omega) = U_{rx}\left(\omega\right) * W\left(\omega\right) \tag{2.52}$$

Based on the usage of the data (in TD or FD), appropriate window need to be selected. Besides its position and span, also shape plays important role in gating. For example, rectangular (Dirichlet) window is most simplest one, however its usage does not yield optimum results in the FD: frequency response of rectangular window is a sinc function - it has relatively narrow main lobe but significant side lobes, that cause ripples in gated signal frequency response. Therefore, many other windows have been designed to suppress this phenomenon (triangular, Gaussian, Hamming, cosine, Kaiser, Blackman-Harris windows etc.).

The main limitation of windowing results from fact, that in many cases, there are no clear borders between early time and late time parts of target response. Furthermore, width of the main lobe and side lobes level of frequency response of the window affect resulting gated spectrum. These effects will be discussed later in this thesis.

2.5.2 Background Subtraction

Another widely used method for elimination of undesired background clutter is background vector subtraction. This technique cal eliminate static reflections from measured signals, provided coherent measurements of target under test and its background are undertaken. That means, that background echo needs to be measured without presence of target in same configuration as in case when the target is present. It is also assumed, that measured signals do not change in time. In ideal case, these two measurements differ only in target reflection. However, effectiveness of this method generally decreased as background level approaches to level of target or even exceeds its amplitude, [23].

According to Subsection 2.2.2 and Eq. (2.11) and Eq. (2.12) respectively, background subtraction can be generally described in TD by Eq. (2.53), where $u_{rx}^{tg}(t)$ represents voltage received from measurement where target is present and $u_{rx}^{back}(t)$ is voltage received from background measurement. Response $h_a(t)$ then states for impulse response of transmit/receive antenna.

$$\begin{aligned} u_{rx}^{tg}(t) - u_{rx}^{back}(t) = \sqrt{\frac{Z_{rx}}{Z_{tx}}} \frac{\partial}{\partial t} u_{tx}(t) * h_a(t) * \frac{1}{2\pi R^2 \mathrm{c}} \delta\left(t - \frac{2R}{\mathrm{c}}\right) \\ * \left[h_{tg}(t, \phi_{tg}) + h_{back}(t, \phi_{tg}) - h'_{back}(t, \phi_{tg})\right] * h_a(t) \end{aligned} \tag{2.53}$$

It is obvious, that this technique is applicable in both, TD and FD, see Eq. (2.54)

$$\begin{aligned} U_{rx}^{tg}(\omega) - U_{rx}^{back}(\omega) = \mathrm{j}\omega U_{tx}(\omega) H_a(\omega) \frac{\mathrm{e}^{-\mathrm{j}2\omega R/\mathrm{c}}}{2\pi R^2 \mathrm{c}} \\ \left[H_{tg}(\omega, \phi_{tg}) + H_{back}(\omega, \phi_{tg}) - H'_{back}(\omega, \phi_{tg})\right] H_a(\omega) \end{aligned} \tag{2.54}$$

In both above described equations, h_{back} or H_{back} denote background response in presence of target and h'_{back} or H'_{back} stand for responses measured without target. Their difference $\Delta h_{back} = h'_{back} - h_{back}$ describes main disadvantage of this method. Presence of target causes partial shadowing of background and also mutual interactions of target and surrounding objects (mainly target support). This difference Δh_{back} then introduces false reflections in subtracted signal.

2.5.3 Calibration by Means of Reference Target

Absolute FF RCS values of arbitrary targets are mostly calculated from measurements generally carried out by indirect method - taking the ratio of two separate target measurement; [23]. Thus, radar system is calibrated by means of accurate "known" calibration standard. It means that the shape of calibration standard needs to be fabricated with minimum tolerances according to operational frequency band and its RCS has to be known very precisely; [69]. Typical calibration process in FD is summarized in Eq. (2.55). Calibrated RCS value of the target σ_{tg} is obtained as ratio of measured scattered field from target E_{tg} and from calibration standard $E_{cal.meas}$ times by computed analytical RCS of the standard $\sigma_{cal.comp}$.

$$\sigma_{tg}(\omega, \phi) = \left| \frac{E_{tg}(\omega, \phi)}{E_{cal.meas}(\omega, \phi)} \right|^2 \sigma_{cal.comp}(\omega, \phi) \tag{2.55}$$

From Eq. (2.55) is obvious that if calibration measurement $E_{cal.meas}$ has significant errors, desired RCS value will contain calibration errors even if target backscattered field E_{tg} is obtained perfectly accurate.

In most cases, calibration metal sphere is employed as a standard for its constant and well known analytical mono-static RCS over whole angular span. However, commonly used spheres can be generally poorly fabricated; [70]. Another option is to use metal cylinders, plates.

2.6 Target Shape Retrieval Based on Broadband RCS and ISAR Imaging

Inverse synthetic aperture radar (ISAR) is a technique that uses radar in order to obtain high resolution image of an object. Is is analogous to synthetic aperture radar (SAR), however ISAR commonly employs rotational motion of the object relative to radar platform rather than radar motion along the target. This rotation generates spatial diversity needed to form synthetic aperture with corresponding enhanced azimuthal resolution in the same manner as in case of SAR; [71].

ISAR is mainly employed as a target recognition and classification technique for maritime and military services to provide contour image and subsequent classification of ships, aircrafts, vehicles, missiles etc., since ISAR is also utilized for high resolution RCS measurement. Another field of use is damages tracking, because holes and cracks can be easily detected by ISAR techique.

Mathematically, basic ISAR processing is similar to computed tomography (CT), [72], used widely in medical applications, however it is also employed in fields of nondestructive material testing - archeology [73], metrology, reverse engineering applications, transport security,[74], [75] etc.

In the case of ISAR, radar range profiles represent 3D-to-1D projection of the target, that can be also referred as Radon transform in the terms of CT. To form the image (or 2D cut) 1D projections are integrated by means of Projection Slice Theorem, interpolated and transformed via 2D IFT. There are various techniques to obtain ISAR image using Radon transform, such as Filtered Back-projection or Time Domain Correlation.

The technique itself comes from description of the target as a set of point-like scattering centers $\gamma(\vec{r}\,')$. Each scattering center is located at position $\vec{r}\,'$ $((x', y'))$ on the target surface and it is defined by its reflectivity according to Fig. 2.10. 2D scattered field from the target can be then described in the same manner as it is stated in Eq. (2.21) - Eq. (2.26) by following Eq. (2.56).

$$S_r\left(\vec{R}_0, k\right) = \iint\limits_S \gamma(\vec{r}\,') \frac{\mathrm{e}^{-\mathrm{j}2kR}}{4\pi R^2} \mathrm{d}^2\vec{r}\,' \tag{2.56}$$

Total scattered field $S_r(\vec{R}_0, k)$ is expressed at observation point $\vec{R}_0$ for each frequency point (or wavenumber k) as an integral of reflectivity distribution over the whole target surface S. Mentioned reflectivity distribution $\gamma(\vec{r}\,')$ actually represents image of the target. In the field of imaging techniques, range factor $4\pi R^2$ is usually neglected. Rewriting the Eq. (2.56) to polar coordinates, total FF received scattered field from the target has form of Eq. (2.57), where angle ϕ denotes turn of the receiver antenna with respect to coordinate system (target), whereas ϕ' are angular positions of target scattering centers and coordinate system.

$$S_r^{FF}(\phi, k) = \iint\limits_S \gamma(r', \phi') \, \mathrm{e}^{\mathrm{j}2kr'\cos(\phi-\phi')} r' \mathrm{d}\phi' \mathrm{d}r' \tag{2.57}$$

Main objective of ISAR technique is then reconstruct target image, described by $\gamma(\vec{r}\,')$, from Eq. (2.57). For example, in terms of aforementioned Filtered Backprojection, reconstructed image of the target is obtained as follows, see Eq. (2.58).

$$I(x', y') = \int\limits_0^\pi \int\limits_{-\infty}^{\infty} P(\phi, k_r)|k_r| \mathrm{e}^{\mathrm{j}2\pi k_r(x'\cos(\phi)+y'\sin(\phi))} \mathrm{d}k_r \mathrm{d}\phi \tag{2.58}$$

Backscattered field S_r^{FF} actually represents azimuth-dependent spatial harmonics ($k \equiv k_r$) of target image - $P(\phi, k_r)$. It can be understood as a ϕ-rotated slice across spatial harmonics domain representation of the target image as it is depicted in Fig. C.2 of Appendix C.

Each image pixel $I(x', y')$ of the target image is therefore retrieved employing 2D IFFT of $P(\phi, k_r)$. The term $|k_r|$ - absolute value of spatial (down-range) wavenumber - acts as a ramp filter function.

More detailed overview of typical ISAR imaging are stated in Appendix C.

2.7 Noise Reduction by Means of Principal Component Analysis

Principal component Analysis (PCA) is statistical method used generally to reduce dimensionality of large datasets containing redundant information. It means that some of data variables are correlated with another variables contained in data set. In other words, PCA is based on assumption, that each data set (i.e. image) consists of patterns separable from each other.

This technique is widely used, among others, in image processing, i.e. in face recognition methods; [76], [77]. Following description of PCA is published in [78].

The main goal of the PCA is to express the original data set in another domain by means of any appropriate linear transformation; [79]. The latter can be defined as:

$$\mathbf{Y} = \mathbf{S}\mathbf{X} \tag{2.59}$$

The original data set $\mathbf{X}$ (i.e. terrain scanning, where rows denote particular measurements - positions of radar, and columns stand for their data samples-frequency/time response) is expressed by a new transformed data matrix $\mathbf{Y}$ through the transformation matrix $\mathbf{S}$. The rows of $\mathbf{S}$ represent eigenvectors - principal components of $\mathbf{X}$. The question stipulates the desired form of transformed data $\mathbf{Y}$ and, consequently, stipulates the transformation matrix that ought to be selected. The measured data set can be characterized by the Signal-to-Noise Ratio and data redundancy, which stands for parts of measured signals correlated to each other, i.e. reflections from rotary support, objects located near target etc. It leads to the evaluation of correlation properties and, therefore, also construction of the covariance matrix from input data.

In this case, PCA finds a set of orthonormal vectors of principal components (matrix **S**) describing the distribution of original data and transforms them into the new set of uncorrelated data. The cornerstone prerequisite of PCA technique states that the final data **Y** ought to be mutually uncorrelated. Hence the covariance matrix of **Y** has to be diagonalized, so that the appropriate transformation matrix **S** is found. The derivation [80] enables to obtain the principal components in the form of eigenvectors of covariance matrix of the original data **X**. The covariance matrix consists of the correlation characteristics (covariance and variances) existing among all pairs of the data set **X**. The covariance between two measurements measures the degree of mutual similarity. A large absolute value denotes a high redundancy (or correlation) of respective data. Contrary to that, zero covariance points to completely uncorrelated data. The covariance of one measurement represents, at the same time, its variance (diagonal components of covariance matrix). In order to construct the covariance matrix from the data set **X**, it is firstly necessary to subtract the mean value from each measurement:

$$\bar{x}_{ij} = x_{ij} - \frac{1}{\mathrm{N}} \sum_{j=1}^{N} x_{ij} \tag{2.60}$$

where x_{ij} denotes the j-th data sample of the i-th row (i.e. measurement). Each measurement is centered and new data set takes the following form:

$$\mathbf{X}_0 = [\bar{\mathbf{x}}_1 \, \bar{\mathbf{x}}_2 \, \cdots \, \bar{\mathbf{x}}_N]^T \tag{2.61}$$

The covariance matrix can be then expressed as a dot product of the centered matrix $\mathbf{X}_0$ that is divided by the number of data samples:

$$\mathbf{C} = \mathrm{cov}(\mathbf{X}) = \frac{1}{\mathrm{N}} \mathbf{X}_0 \mathbf{X}_0^T \tag{2.62}$$

Principal components of PCA method are represented by eigenvectors of the covariance matrix **C**. These can be obtained by means of the Singular Value Decomposition method (SVD) that allows factorizing the data matrix onto its $\mathbf{\Lambda}$ eigenvalues and eigenvectors **U** and **V**:

$$\mathbf{X}_{M \times N} = \mathbf{U}_{M \times M} \mathbf{\Lambda}_{M \times N} \mathbf{V}_{N \times N}^T \tag{2.63}$$

The left matrix **U** represents eigenvectors of the $\mathbf{X}\mathbf{X}^T$ matrix, which is in fact identical to the covariance matrix, while **V** embraces eigenvectors of $\mathbf{X}^T\mathbf{X}$. Accordingly, the principal components of the PCA are evaluated in equation (2.64) as the matrix **U**. Yet apart from the principal component, the complete PCA method can be carried out via SVD as well by rewriting the equation (2.59) in the following manner:

$$\mathbf{\Lambda} \mathbf{V}^T = \mathbf{U}^T \mathbf{X}_0 \tag{2.64}$$

On the right side, the input data are multiplied by the matrix of principal components, so $\mathbf{U}^T \equiv \mathbf{S}$. Subsequently, the left side of (2.64) represents a transformed input data $\mathbf{X}_0$ with a zero correlation between particular measurements ($\mathbf{\Lambda V}^T \equiv \mathbf{Y}$). Furthermore, in the PCA the eigenvalues from $\mathbf{\Lambda}$ are sorted in descending order. Since each eigenvalue is related to a certain eigenvector (principal component), the matrix $\mathbf{U}$ is reorganized as well. Every eigenvalue represents a specific amount of variance in measured data and thus reflects the importance of particular eigenvector. In fact, the eigenvector (belonging to the largest eigenvalue – first principal component) contributes decisively, among others, to the reconstruction of the original data set, because it shows the highest correlation. The second principal component is correlated with some of the original data that are uncorrelated with first component. Since the matrix $\mathbf{S}$ of principal components is orthonormal ($\mathbf{S}^{-1} = \mathbf{S}^T$), the original data are obtained by means of the following transformation:

$$\mathbf{S}^T\mathbf{Y} = \mathbf{S}^T\mathbf{S}\mathbf{X}_0 \equiv \mathbf{X}_0 \tag{2.65}$$

Based on the selected components, the required data set can be restored only from the selected ones. The reconstruction applying only to n components $\{c_1,\, c_2,\, \dots c_n\}$ is expressed by the following equation:

$$\tilde{\mathbf{X}} = \mathbf{S}_n^T\mathbf{Y}_n = \left[\begin{pmatrix} \vdots \\ \mathbf{s}_{c1} \\ \vdots \end{pmatrix} \begin{pmatrix} \vdots \\ \mathbf{s}_{c2} \\ \vdots \end{pmatrix} \cdots \begin{pmatrix} \vdots \\ \mathbf{s}_{cn} \\ \vdots \end{pmatrix}\right] \begin{bmatrix} (\cdots \mathbf{y}_{c1} \cdots) \\ (\cdots \mathbf{y}_{c2} \cdots) \\ \vdots \\ (\cdots \mathbf{y}_{cn} \cdots) \end{bmatrix} \tag{2.66}$$

Dimension of the reconstructed matrix is identical to the one of the original matrix $\mathbf{X}$.

2.7.1 Principal Components Selection

In PCA, total number of principal components (PC) in $\mathbf{S}$ (eigenvectors of covariance matrix) is equal to total number of variables $\mathbf{X}$ - signals. According to Eq. (2.60), each variable is firstly transformed, so that it has zero mean value and thus its variance equals to one. It means, that every variable contributes to **total variance** (which is sum of particular variances) by one unit. Based on this, particular PC can be characterized as follows. The first PC accounts for maximal amount of total variance in variables and thus it is correlated with some of variables. Second PC then also accounts for maximal amount of total variance excluding variance belonging to first PC. Following this, second PC is, just as first PC, correlated with some of variables that have zero correlation with fist PC. Remaining components can be described in the same way.

It practically means, that if data set (i.e. image) consists of well-identifiable and separable patterns, each of these patterns will be described by one component in ideal case. Therefore, first PC belongs to strongest pattern, second PC to second strongest pattern etc. PCA method sorts PC according to their importance. Image can be then restored only from certain amount of most important PCs. There are several approaches for determining number of PCs needed, [81].

Scree Test

Scree test is visual inspection-based technique to determine minimum number of retaining PCs. It employs plot of eigenvalues associated with each principal component in order to reveal obvious break in the trace. In other words, quick change of slope of eigenvalues trace is finding. PCs corresponding to eigenvalues before break are maintained whereas other PCs are discarded.

For its simplicity, scree test is one of the most used strategy to determine number of PC that retain in data restoration process. However, it works well only when data set contain only few significant patterns.

Kaiser Criterion

Kaiser criterion, or the eigenvalue-one criterion is based on selection of significant PCs according to their eigenvalues. Simply, PC with eigenvalue lager than one is retained. It follows the fact that each variable contributes one unit of variance to total variance in original data set. Any PC with eigenvalue greater than one accounts for higher amount of variance than had been contributed by one variable; [82]. It is very simple criterion, since it does not require subjective assess and can be adjusted to particular problem. However, it can be unsuitable when number of eigenvalues greater then one rises. It means, that many mutually uncorrelated patterns in data set; [83].

Criterion of Variance Proportion

The criterion of proportion of total variance is another simple criterion for estimating number of significant PCs accounting for a specified proportion of variance so only PCs exceeding i.e. 10% of total variance are selected. This criterion can be adjusted in way that PCs with certain cumulative sum of variances are retained for data set description; [81].

Chapter 3

Main Goals of the Thesis

Based on the previously presented state of the art of NF RCS measurement and imaging, the main goals of this thesis can be stated as follows.

3.1 Precise and Fast FF RCS Determination From Simple Wide-Band NF Measurements in Indoor Conditions

Knowledge of precise RCS parameters is important worldwide, due to its importance in the field of design of modern aircrafts, boats, cars, military vehicles etc., as well as for radar systems development. Since the outdoor test sites are impractical for their large required measurement ranges and it is difficult to theoretically estimate RCS of complex targets owing to the impossibility to cover all scattering mechanisms in simulations, indoor, short-range RCS measurements in NF have been developed and used widely nowadays. Still, there are efforts in developing fast and simple measurement and processing technique in order to obtain RCS from near-field measurements. Based on the fact, that measurements of RCS in very close proximity of the target and measuring antenna is still challenging subject of research, this thesis focus on such measurements in small anechoic chamber (4x3x6 m), where FF conditions cannot be generally met for electrically large objects. One of the promising measurement method, used for this purpose, is Circular Near-Field to Far-Field Transform (CNFFFT), that has been thoroughly described in previous chapter.

Till now, performance of CNFFFT technique has been evaluated using primarily numerical models of simple targets and only few papers deal with real target measurements, i.e. [60], [61], [84], [85]. Furthermore, only narrow bandwidths (ones of GHz) of transmit signals have been employed leading to small down-range resolution. In addition, no image reconstruction performances have been presented yet. Accordingly, partial goal of this thesis comprises evaluation of applicability of CNFFFT using very broadband (15 GHz) transmit signal and real single- and multiple-scattering objects. Suggested solution is presented in Chapter 5 and follows pre-processing methods (Chapter 4) used in this case. Resulting estimated RCS data will be then used in image processing later on.

3.2 Elimination of Wide-Band Antenna Tapering Effects in the NF RCS Measurements

Supposing mono-static arrangement, measuring antenna could be located in NF of the target and vice versa. On the other hand, in most cases target is in the antenna FF. Due to its directional radiation pattern, target is illuminated non-uniformly, which leads to that the scattering centers, located on target far away from main beam direction of antenna, contributed incorrectly to total back-scattered field. Therefore antennas with small apertures are primarily used because of their main beam, that is wide enough to assure minimum beam taper across illuminated target extent. However, in case of wide-band antennas (i.e. one decade of frequency bandwidth) the radiation pattern typically narrows with increasing frequency. In fact, these antennas need to be used for high-resolution imaging purposes. From the time-domain (TD) point of view, the radiated signals differ in azimuthal extent - they are delayed and distorted compared to the one radiated in main-beam direction. The next goal of the thesis is to eliminate aforementioned antenna effects based on knowledge of wideband antenna radiation patterns. Following this, novel antenna frequency/impulse responses measurement and computation technique will be proposed in both, TD and FD for calculation required radiation patterns. Corresponding results are outlined in Chapter 6 of this thesis.

3.3 Objects Shape Reconstruction From the FF-Restored Data, Reduction Clutter and Dimensionality of Resulting Images

Besides RCS patterns, targets can be characterized in TD, or rather in spatial domain, also by their shape restored from broadband measurements. Well known ISAR technique is often used for targets classification purposes and for imaging of their scattering centers. However, NF measurements and subsequent data processing introduce errors (referred as clutter) that in final images represent, besides shape distortion, unwanted reflections or false scattering centers of target. These originate mainly from both, reflections from objects surrounding the target as well as from imaging technique itself.

Following this, next goal of this thesis cover image formation from NF data. Data obtained in NF, corrected and processed by proposed techniques will be used to obtain spatial 2D images of measured targets. Applicability of CNFFFT will be also shown in image processing. In addition, clutter and dimensionality of final images will be reduced incorporating statistical PCA technique. Results concerning this goal are discussed in Chapter 7.

Chapter 4

Methodology of RCS Calculation

According to previously outlined methods, next part of this thesis deals with FF and NF measurements of mono-static RCS, that is, besides bi-static case, still matter of interest and further improvement. Bi-static RCS is not considered in this thesis since employed test facility cannot provide bi-static measurements. Furthermore, presented techniques can be generalized to bi-static case as well.

This chapter firstly describes methodology of mono-static RCS measurements in anechoic chamber employing broadband horn antenna and vector network analyzer acting as radar system. In order to obtain valid RCS values from both, FF and NF measurements, errors related directly to measurements need to be corrected. Therefore, pre-processing techniques are presented in following part. Finally, RCS patterns of small metal plates are calculated from FF data and compared to modeled results to verify proposed pre-processing steps. This chapter serves as a prerequisite for further NF-FF processing steps.

4.1 Mono-static Measurement Setup

All presented results rise from measurements undertaken in full anechoic chamber located at the Department of electromagnetic field, CTU in Prague. Measuring equipment allows performing fully automated transmission and reflection measurements of basic antenna parameters (primarily radiation, polarization patterns) as well as mono-static RCS of various objects in full 360 degrees azimuthal span. Both, amplitude and phase of received signal is stored therefore NF measurements can be performed in order to compute FF estimation of required quantities.

Overall scheme of last mentioned full anechoic chamber and instrumentation employed for mono-static RCS measurements is shown in Fig. 4.1 and Appendix A.

Inner extent of the chamber is approximately 4x3x6 m (width x height x length), whereas maximum possible measurement distance R_{max} between antenna and target is 4 m. Targets under test are mounted on rotary fiberglass support connected to stepped motor that is synchronized with vector network analyzer (VNA) Rohde&Schwarz ZVA40, [86], acting as transmitter and receiver. Both positioning system as well as synchronization are manufactured by NSI-MI company, [87]. VNA

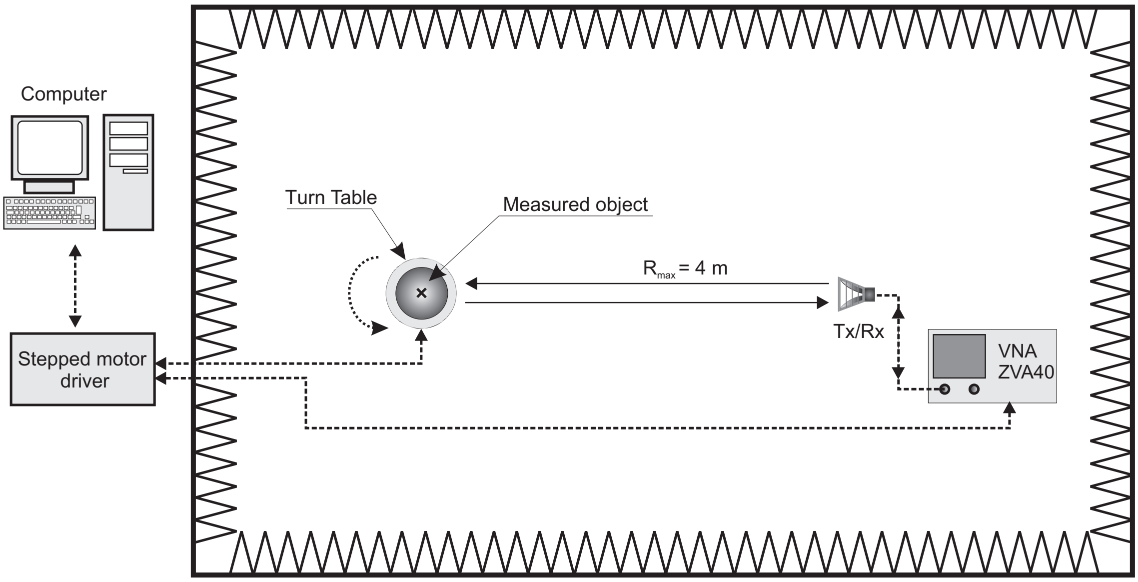

Figure 4.1: Monostatic measurement scheme in anechoic chamber.

is connected to broadband Double Ridged Horn (DRH) antenna DRH20, [88], with operational frequency bandwidth 1.7 - 20 GHz. Mono-static RCS measurement itself is then based on collecting backscattered field along circle that encloses target under test while it is rotating relative to fixed Tx/Rx antenna. Only vertical polarization of antenna is employed for purpose of this work.

Dimensions of the anechoic chamber do not allow to measure FF RCS of electrically large objects. Theoretical minimum FF ranges (according to Eq. (2.10)) for targets with different maximum dimensions D are depicted in Fig. 4.2. It is obvious, that only targets of maximum dimension approximately up to 0.16 m can be measured up to frequency 20 GHz meeting FF conditions.

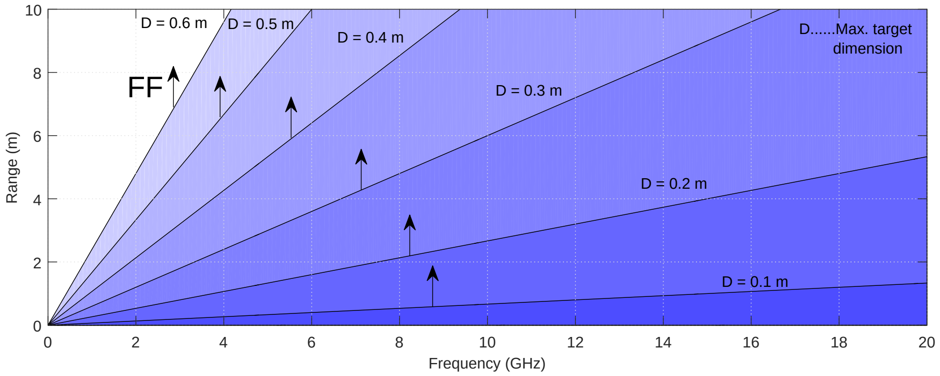

Figure 4.2: Minimum FF distances for different maximum targets dimensions and frequency ranges.

In this thesis, frequency range for measurement is set to 3 - 18 GHz covering C-band (4 - 8 GHz), X-band (8 - 12 GHz) and Ku-band (12 - 18 GHz) radar frequency bands. It is chosen according to theoretical down-range (along-track resolution) resolution and dynamic range of the measurement system. Given 15 GHz bandwidth results in $\Delta R_0 = 1$ cm resolution (see Eq. (2.6)).

To obtain time domain response from the target located at certain distance from the measuring antenna, unambiguous range need to be defined. From the transmit power and target RCS point of view, it represents maximum detection range given by radar equation, however it also determines time duration of the two-way signal traveling from radar to target and back. Following Fourier theory, unambiguous range then defines frequency sampling of the transmit signal and it is represented, according to Eq. (2.5), by following Eq. (4.1):

$$\Delta f = \frac{c}{2R_{unamb}} \tag{4.1}$$

Considering full range extent of the chamber and multiple reflections of the backscattered signal, unambiguous range is set to $R_{unamb} = 6$ m, that leads to the frequency sampling $\Delta f = 25$ MHz. Minimum azimuthal sampling results from cylindrical NF scan, see Eq. (2.20) for longest measured target. Suppose, that its length does not exceed 1 m, thus minimal azimuthal step is then (Eq. (4.2)):

$$\Delta\phi = \frac{\lambda_{min}}{2a_{min}} = 0.0167 \text{ rad} = 0.95° \tag{4.2}$$

All the key parameters mentioned above are summarized into Tab. 4.1.

Table 4.1: Basic setup parameters.

Term	Value
Frequency bandwidth	$BW = 3 - 18 \rightarrow 15$ GHz
Downrange resolution	$\Delta R_0 = c/2BW = 0.01$ m
Unambiguous range	$R_{unamb} = 6$ m
Frequency step	$\Delta f = 25$ MHz
Azimuthal step	$\Delta\phi = 0.5°$

Common coordinate system used across this thesis is outlined in Fig. 4.3. It is assumed, that target under test is situated in center of the coordinate system and it is rotated along z axis. Target is turned towards to measuring antenna by azimuthal angle ϕ. Distance R_0 represents range between antenna position (x, y, z) and center of target rotation, whereas R denotes distance of antenna and any point on target (x', y', z') defined by position vector $\vec{r'}$.

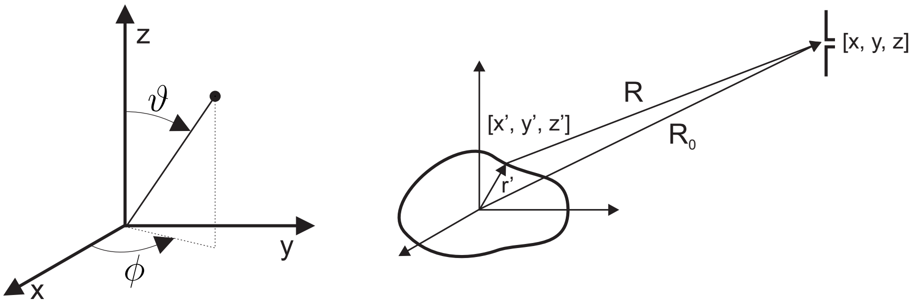

Figure 4.3: Coordinate system.

4.2 Data Pre-processing

Data pre-processing comprises methods for eliminating (mainly) systematic errors from measured data and correcting procedures in order to obtain correct absolute RCS values of target under test.

Therefore, well-known techniques of S-parameters calibration, time gating, background vector subtraction will be examined in following part of this thesis. Moreover, RCS normalization will be proposed to correct distance and antenna effects on received signal.

4.2.1 S-parameters Calibration

Dynamic range of the measuring system is limited by its particular parts, mainly VNA, cables and antenna. Length of the cable, connecting the VNA and Tx/Rx antenna, introduces additional attenuations. Furthermore, it also reduces unambiguous range between antenna and target, since the reference plane (R = 0) is set approximately at VNA ports as it is outlined in Fig. 4.4. It represents absolute value of time-domain response of mono-static metal plate measurement. Major reflections account for connection mismatches of VNA-cable and cable-antenna. Further reflection stands for antenna aperture mismatch. Target echo can be located at distance 2 m from the antenna. Effect of imperfect absorber coating of rotary positioner is evident approximately 0.5 m away from target. Last reflection (at approx. 6 m) represents effect of Fourier transform - discretized spectrum is transformed to periodically repeated time (range) response signal.

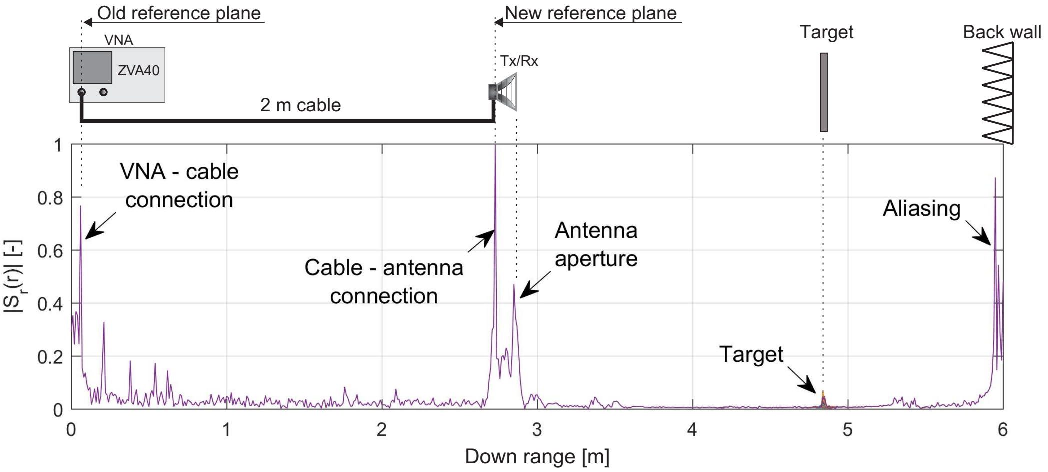

Figure 4.4: Uncalibrated time response of target reflection measurement.

In order to suppress systematic errors of measurement path, namely VNA and cable connected to the antenna, well known one-port Open-Short-Match (OSM) calibration should be performed. Its presumption is based on the division of the real VNA into the ideal VNA and the error four-port. After the measurement of the set of previously known three standards (whereby the error model is determined) is performed at required reference plane (that is the end of the cable connected to antenna in this case), the systematic errors of the VNA can be corrected.

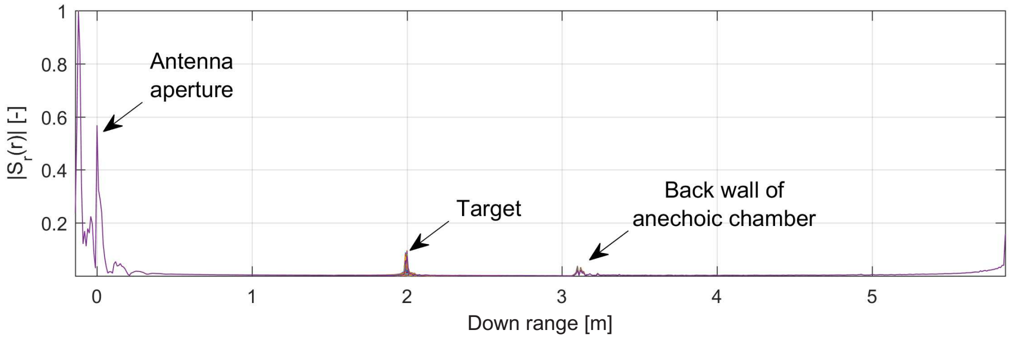

Figure 4.5: Calibrated time response.

However, used measurement instrumentation that comprises VNA ZVA40 and NSI positioning controller does not allow to calibrate the system directly, therefore measured data are corrected by post-processing OSM calibration method implemented in Matlab. Corrected data set is depicted in Fig. 4.5. Reference plane moved to the antenna connector which results in increase of maximum detection range from approx. 3 m to 6 m so further reflections can be detected, as backscattered field from back wall of the anechoic chamber (located 3.3 m away from antenna), that has not been seen in uncalibrated case.

4.2.2 Background Subtraction

Measured and corrected data, as depicted in Fig. 4.5, suffer still from unwanted reflections (caused by antenna) and background clutter. Calibrated mono-static TD transfer function can be derived from Eq. (2.11) into following form, see Eq. (4.3).

$$\begin{aligned} u_{rx}(t) = \frac{\partial}{\partial t} u_{tx}(t) * h_a(t) * \frac{1}{2\pi R^2 \mathrm{c}} \delta\left(t - \frac{2R}{\mathrm{c}}\right) \\ * \left[h_{tg}\left(t, \phi_{tg}\right) + h_{back}(t, \phi_{tg})\right] * h_a(t) \end{aligned} \tag{4.3}$$

Described relation is represented in FD accordingly, (Eq. (4.4)).

$$\begin{aligned} U_{rx}(\omega) = \mathrm{j}\omega U_{tx}(\omega) H_a(\omega) \frac{\mathrm{e}^{-\mathrm{j}2\omega R/\mathrm{c}}}{2\pi R^2 \mathrm{c}} \\ \left[H_{tg}\left(\omega, \phi_{tg}\right) + H_{back}(\omega, \phi_{tg})\right] H_a(\omega) \end{aligned} \tag{4.4}$$

It is obvious, that such transfer function consist of sum of the particular transfer functions representing reflections from target $h_{tg}(t, \phi_{tg})$ and also from background, antenna connection and its aperture. These unwanted reflections are summarized in $h_{back}(t)$ and will be referred as background. It is therefore possible to subtract undesirable responses from target response by means of vector background subtraction.

The technique coherently subtracts signals backscattered from test range with and without presence of target at its every azimuthal position. Background signal is supposed to be constant in time that means the target surrounding does not vary with time and there are no other noise signals present. It is important to measure background signal in the same arrangement as with presence of target to minimize errors risen from misalignment of target support and other objects, cable movement etc.

Resulting subtracted signal $u_{rx}^{subtr}(t)$ then should contain, except antenna responses, only impulse response of target and error term Δh_{back}. According to Eq. (2.53), subtracted signal is described by Eq. (4.5).

$$\begin{aligned} u_{rx}^{subtr}(t) = \frac{\partial}{\partial t} u_{tx}(t) * h_a(t, \phi_a) * \frac{1}{2\pi R^2 \mathrm{c}} \delta\left(t - \frac{2R}{\mathrm{c}}\right) \\ * \left[h_{tg}(t, \phi_{tg}) + \Delta h_{back}(t, \phi_{tg})\right] * h_a(t, \phi_a) \end{aligned} \tag{4.5}$$

From the equations mentioned above, there is obvious, that background subtraction can be performed in both, time and frequency domain. Results of background subtraction technique is demonstrated on corrected signal (4.5) from previous subsection.

Subtracted signal from metal plate measurement is depicted in Fig. 4.6 and Fig. 4.7, that represents the same background corrected target range profiles versus azimuth.

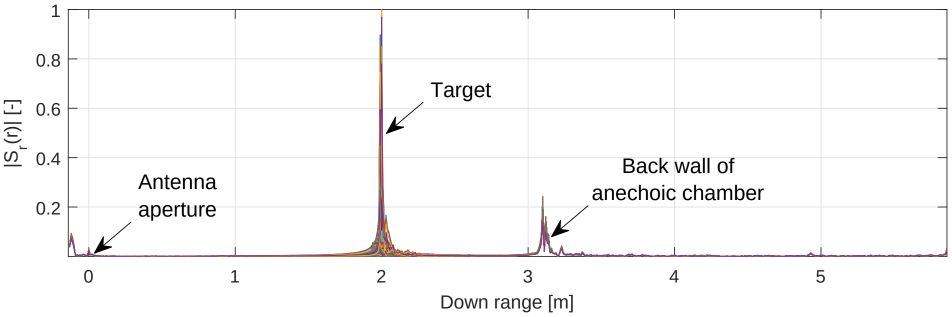

Figure 4.6: Time response of target after background subtraction.

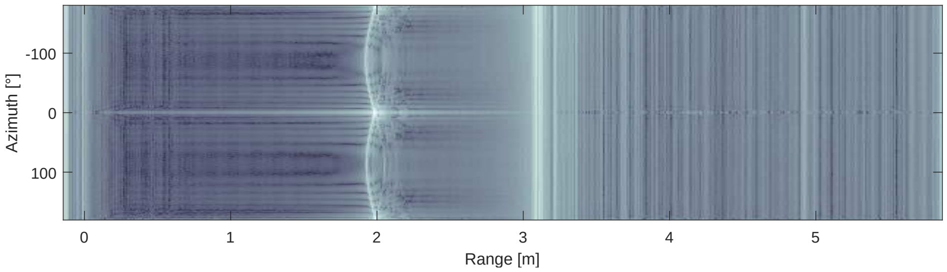

Figure 4.7: Subtracted target response versus azimuthal angle.

After the subtraction, almost all clutter reflections from surrounding were eliminated, whereas target can be clearly detected. Also static reflections from target support and from other objects, located in vicinity of the target, are suppressed. However, this technique is not able to deal with multiple interactions i.e. between target and its rotary support, that is one of the main disadvantage, that cannot be easily avoided. Another drawback is based on target shadowing whose effect is evident in aforementioned figures. From the radar point of view, target shadows the objects that would be normally illuminated by radar signal without its presence. Therefore, background signal contain reflection components from these "shadowed" object, that in turn, create undesired reflections in subtracted signals, represented by Δh_{back}. Here, these are located 3.3 m far from the antenna aperture and represent backscattered field from the back wall of the anechoic chamber. Another minor additional reflections, risen from subtraction, are caused by mutual interactions of antenna and the target, where its presence slightly changes antenna impedance matching. However, last mentioned errors can be removed by means of time gating.

4.2.3 Time Gating

Apparent residual reflections in Fig. 4.6, remained primarily from background subtraction, that are located in sufficient distance from the target reflection, can be filtered out employing **time gating**. According to Eq. (2.52), this filtering process is mathematically represented in TD as multiplication of received signal $u_{rx}(t)$ with appropriate windowing function $w(t)$, whereas in FD, frequency responses are convolved.

Based on the usage of data (in TD or FD), appropriate window need to be selected in order to obtain most correct results as possible. Main parameters of gating window, that affect final signal, are its shape (type) and width. There are many types of windows designed according their application. TD and FD representation of some widely used windows is outlined in Fig. 4.8. All the windows are plotted for same number of points (samples). Width and shape of each window in TD correspond to width of mainlobes and sidelobes attenuation to their FD representation. Widening of the window in TD its mainlobe narrows in FD and vice versa according to Fourier theory. Basic parameters of depicted windows are summarized in Tab. **??**.

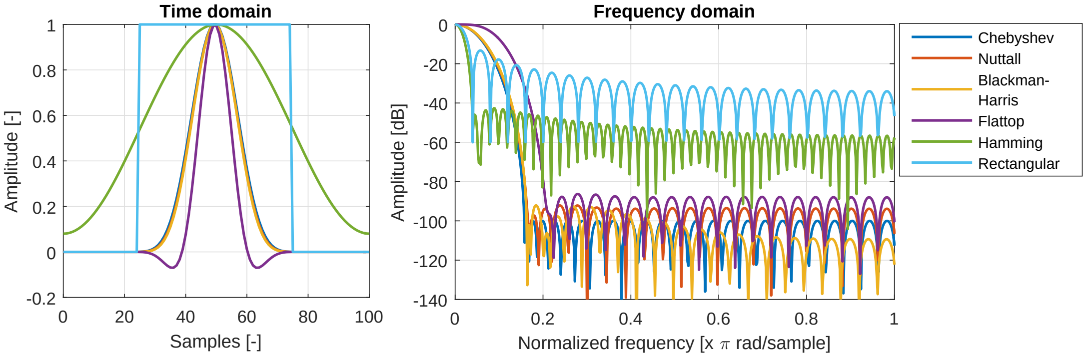

Figure 4.8: Traces of selected filtering windows.

Here, leakage factor represents ratio of power in the sidelobes to the total window power. Difference in height from the mainlobe peak to the highest sidelobe peak is described as relative sidelobe attenuation. Mainlobe width is then defined as width of the mainlobe at 3 dB below its peak value. It can be seen, that rectangular window has narrowest mainlobe among presented ones, however suffers from small

Table 4.2: Basic parameters of filtering windows.

Window name	Leakage (%)	Rel. sidelobes att. (dB)	Mainlobe width (-)
Chebyshev	0.00	-100.0	0.0547
Nuttall	0.00	-93.8	0.0586
Blackman-Harris	0.00	-92.1	0.0586
Flattop	0.00	-88.0	0.1172
Hamming	0.03	-42.5	0.0390
Rectangular	9.14	-13.3	0.0273

sidelobes attenuation. On the other hand, i.e. mainlobe width of Chebyshev window is wider but has significant sidelobes suppression. Both of these characteristics affect filtered signal in FD in different manner.

Whilst sidelobes attenuation of almost all used windows is sufficiently high and affect filtered signal negligibly, their width in TD, and accordingly in FD, can distort frequency response of signal. In the next figures (Fig. 4.9 and Fig. 4.10), there is presented influence of window width on the calculated RCS of metal plate at 10 GHz. Fig. 4.9 shows different widths of rectangular window that determine amount (length) of filtered signal - reflection from target - from which the RCS is subsequently calculated.

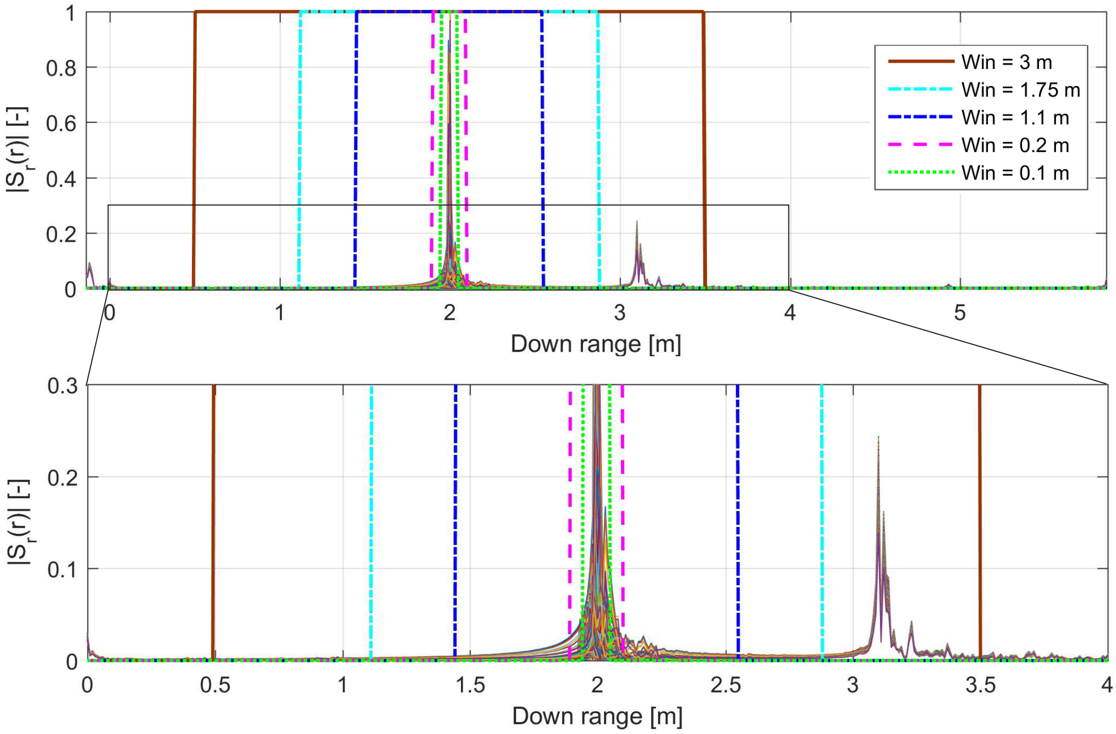

Figure 4.9: Different width of gating rectangular window.

In the Fig. 4.10 are then calculated RCS for such filtered signals. In the first case (width of window equals to 3 m), the reflection from back wall of the anechoic chamber is included into RCS calculation. It leads to significant errors in resolving sidelobes of the RCS pattern. Next extreme case shows filtering of the signal by narrow window (0.1 m), where parts of target reflection are not included in RCS calculation. It can be clearly seen that RCS is determined correctly within azimuthal range approx. ±44°. It means that only reflections, corresponding to target rotated towards to antenna more than ±44°, are filtered out.

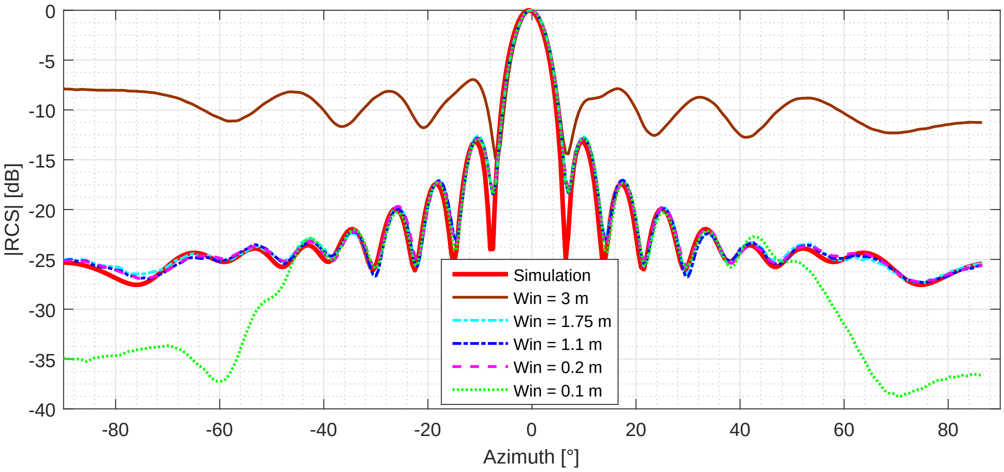

Figure 4.10: RCS of metal plate at 10 GHz - change of width of gating window.

Remaining window widths cover more or less target reflection and correct shape of RCS is obtained. Nevertheless, main limitation of gating technique results from fact, that in many cases there are no clear borders of target response. Furthermore, another reflections from adjacent object and their mutual interactions can be very close to main reflection from target that cannot be removed without loss of the part of required signal.

Among previously stated facts, another obvious error rises from using time gating technique. Multiplication of the signal and window in TD is represented in FD by convolution. Narrowing the window in TD accordingly broaden its mainlobe in FD, where it is convolved with frequency response of the signal. It leads to undesirable distortion (cutoffs) at the edges of filtered frequency response and RCS cannot be determined at corresponding frequencies, as it is shown in Fig. 4.11.

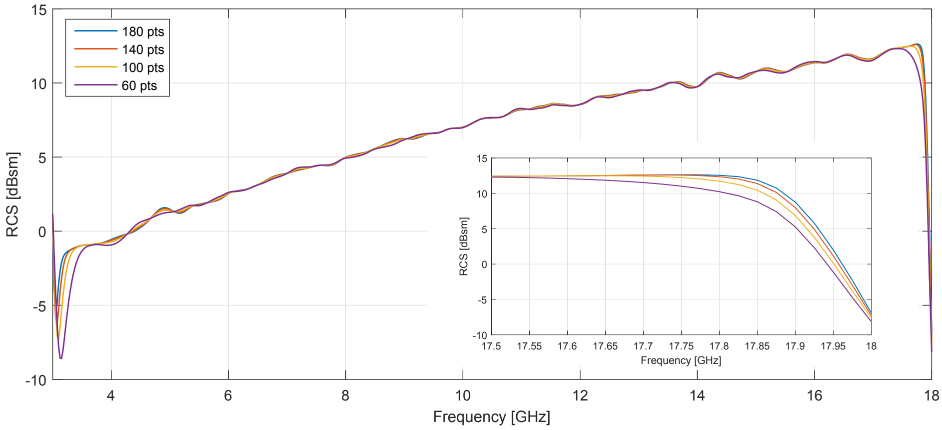

Figure 4.11: Reducing of usable frequency response of signal as a consequence of narrowing the gating window in TD.

In this case, usable frequency response of flat plate RCS is reduced with narrowing TD gating window, whereas remaining part of response remains unchanged.

This undesirable effect can be observed also with change of window type, see Fig. 4.12. Edges distortion of frequency bandwidth changes primarily with different mainlobes widths of same-length windows (Fig. 4.8). Furthermore, signal filtered by rectangular window contains considerable ripples due to its small sidelobes attenuation. That is also reason why the rectangular window is not often used.

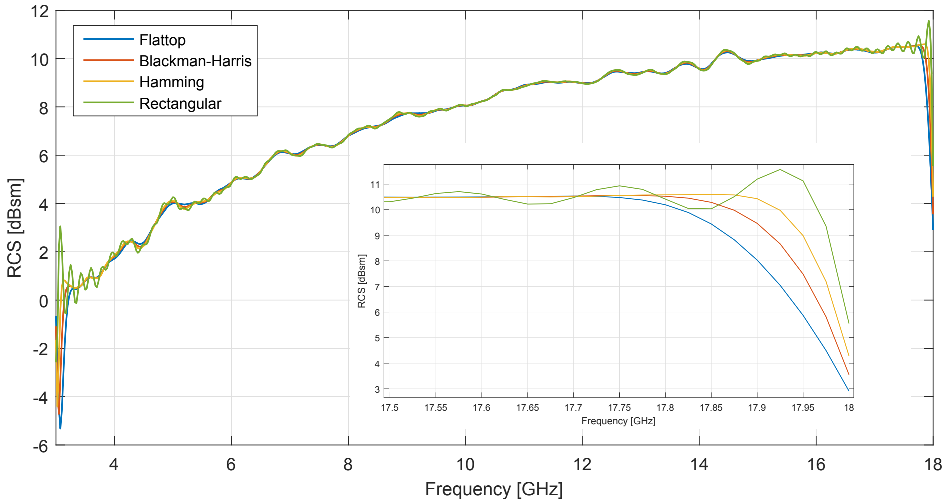

Figure 4.12: Impact of selected gating windows on filtered frequency response of signal.

4.2.4 RCS Normalization

Determination of correct mono-static RCS absolute value involves normalization (calibration) of measured data according to radar equation, see (Eq. 2.1)). Typical normalization scenario incorporates calibration method based on well known standard (sphere, cylinder). This approach relies on precise measurement and analytical knowledge of precisely fabricated standard, see Eq. (2.55). In case of sphere acting as calibration target, its appropriate diameter need to be chosen according measurement scenario and frequency range - circumference of the sphere should be 10 times greater than wavelength of incident wave in order to ensure its measurement in optical region. It results, however, in increasing measurement range where FF condition for such sphere is met. Contrary to that, spheres of smaller diameter are measured in resonant region where, besides of specular reflections, exist creeping waves interacting with specular ones or with surrounding objects.

From aforementioned facts indirect calibration with known standards seems to be difficult to apply for wideband, short range NF and FF measurements described in this thesis. Therefore, in next section RCS normalization technique based on antenna transfer function (or gain) measurements will be described. Furthermore, such measurement will be employed in NF to FF RCS reconstruction process, namely in antenna radiation pattern compensation.

Mono-static, FD reflection measurement scenario can be described from the simplified signal flow graph as follows, see Fig. 4.13. Target represented by its reflection coefficient $\Gamma_{obj}(\omega, \phi)$ is located in distance r from the Tx/Rx antenna, that is defined by 2-port and its S parameters. $\Gamma_{air(\omega)}$ then represents the reflection from air, exponential terms denote the wave propagation and $\Gamma_{obj}(\omega, \phi)$ includes reflections from the target and clutter. The measured data are then expressed as the total reflection coefficient $\Gamma_{meas}(\omega)$, see Eq. (4.6). This equation can be computed directly using Mason's rule, see Appendix B. For the clarity reasons, all variables will be stated without angular and azimuthal dependencies.

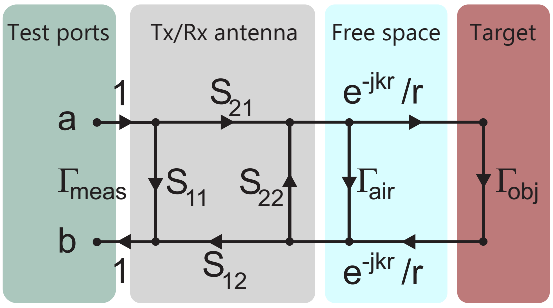

Figure 4.13: Flow chart of the monostatic RCS measurement.

$$\Gamma_{meas} = S_{11} + \frac{S_{21}S_{12}\left(\Gamma_{air} + \Gamma_{obj}\dfrac{\mathrm{e}^{-\mathrm{j}2kr}}{r^2}\right)}{1 - S_{22}\left(\Gamma_{air} + \Gamma_{obj}\dfrac{\mathrm{e}^{-\mathrm{j}2kr}}{r^2}\right)} \approx S_{11} + S_{21}S_{12}\Gamma_{obj}\frac{\mathrm{e}^{-\mathrm{j}2kr}}{r^2} \tag{4.6}$$

Since the S_{11} and S_{22} describe the connector and aperture reflections of the antenna, their influence can be removed from the data set by the process of time gating. Furthermore, Γ_{air} can be considered as equal to zero. The denominator can be then approximated by one due to its negligible exponential term. In the remaining relation, the $S_{12}S_{21}$ describes the antenna transmission parameters and the exponential term represents wave propagation (in both directions). To suppress additional reflections from Γ_{obj}, background vector subtraction can be utilized.

In order to extract the Γ_{obj} from this simplified equation, the second measurement, concerning only two antennas, is carried out in next step. The separation equals (in general) to the distance between the antenna and target. The signal flow graph of this scenario is depicted in Fig. 4.14.

Total transmission coefficient can be computed from this signal graph, see Eq. (4.7):

$$\frac{b}{a} = \frac{S_{21}S'_{12}\dfrac{\mathrm{e}^{-\mathrm{j}kr}}{r}}{1 + \Gamma_L A_1 + S_{22}S'_{22}\Gamma_{air}^2 - S_{22}\Gamma_{air} - S'_{22}\Gamma_{air} - S_{22}S'_{22}\dfrac{\mathrm{e}^{-\mathrm{j}2kr}}{r^2}} \tag{4.7}$$

Here, $A1$ is expressed by Eq. (4.8) as follows.

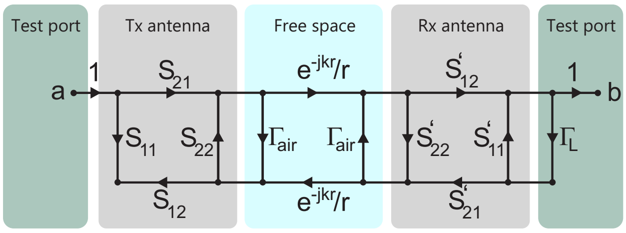

Figure 4.14: Flow chart of the transient measurement.

$$A1 = S'_{11}S_{22}\Gamma_{air} + S'_{11}S'_{22}\Gamma_{air} + S'_{12}S'_{21}S_{22}\Gamma^2_{air} - S'_{11}S'_{22}S_{22}\Gamma^2_{air} + \left(S'_{11}S'_{22}S_{22} - S'_{12}S'_{21}S_{22}\right)\frac{\mathrm{e}^{-\mathrm{j}2kr}}{r^2} - S'_{11} - S'_{12}S_{21} \tag{4.8}$$

Supposing two identical antennas, Eq. (4.7) and Eq. (4.8) are reduced to form of Eq. (4.9) and Eq. (4.10) respectively.

$$A1 = S_{12}S_{21}S_{22}\Gamma^2_{air} - S_{12}S_{21} - S_{11}\left(1 - S_{22}\Gamma_{air}\right)^2 + \left(S_{11}S^2_{22} - S_{12}S_{21}S_{22}\right)\frac{\mathrm{e}^{-\mathrm{j}2kr}}{r^2} \tag{4.9}$$

$$\frac{S_{21}S_{12}\dfrac{\mathrm{e}^{-\mathrm{j}kr}}{r}}{\Gamma_L A_1 + \left(1 - S_{22}\Gamma_{air}\right)^2 - S^2_{22}\dfrac{\mathrm{e}^{-\mathrm{j}2kr}}{r^2}} \tag{4.10}$$

When the resulting equation is simplified as in the first case, and, given the matched receiver ($\Gamma_L = 0$) and negligible backward transmission (exponential term), the transmission coefficient takes the final form as follows, see Eq. (4.11):

$$\frac{b}{a} \approx S_{21}S_{12}\frac{\mathrm{e}^{-\mathrm{j}kr}}{r} \tag{4.11}$$

Since described measurement is undertaken in anechoic chamber, above mentioned simplification can be taken into account. Final relation (Eq. (4.11)) can be de-convoluted from Eq. (4.6) and Γ_{meas} can be obtained with additional $1/r^2$ distance correction. Given method describes typical antenna gain and free-space loss compensation. Second transition measurement can be substituted by known antenna gain values (obtained typically from calibrated antenna measurements in main-beam direction) in case of FF RCS measurements. However, for the purpose of antenna pattern compensation of NF RCS, broadband, azimuth-dependent antenna transient responses S_{21} and S_{12} need to be known. Furthermore, in this particular case (when the distance between the target and antenna is 2 m), if the distance between antennas in transient response measurement equals to 4 m, the Γ_{obj} can be directly obtained by de-convolution of Eq. (4.11) from Eq. (4.6).

4.2.5 FF RCS Measurements - Validation of Pre-processing Techniques

RCS of selected simple targets, calculated from mono-static FF measurements are presented in this subsection to verify measurement process and correction techniques that are used in both, NF and FF processing techniques. Validity of measurements and correction techniques are verified by numerical simulations undertaken in CST Microwave Studio and FEKO full-wave software, that have been proven to give adequately precise results.

In order to obtain RCS of selected targets, aforementioned correction techniques are utilized to measured data according to following Fig. 4.15.

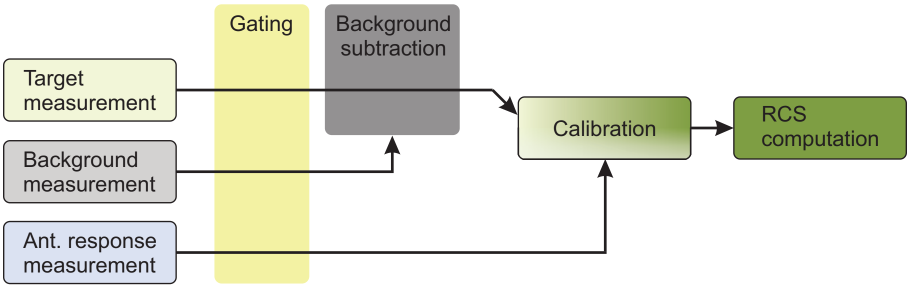

Figure 4.15: FF measurement and calibration process.

Firstly, OSM calibration standards are measured within specified frequency band by means of VNA to perform offline error vector correction of measured data. Mono-static reflections from target and background are subsequently measured in FD in selected azimuthal span with given sampling. According to FF criteria and dynamical range of system, distance between target and antenna R_0 is set to 2 m or 3.5 m. In case of uncalibrated antenna, its response is measured according to section 4.2.4. These three measurements are then subject of time gating process. Alternatively, background can be subtracted from target signal in FD at first and gated afterwards.

Suppressing overall system errors as possible during measurement and data correction, relative RCS of the target is obtained. In order to calculate its exact absolute value within given frequency bandwidth, RCS level equalization is performed based on known antenna gain or its measured frequency response and its distance to target. Metal plates of different dimensions are selected as test targets, see Fig. 4.16.

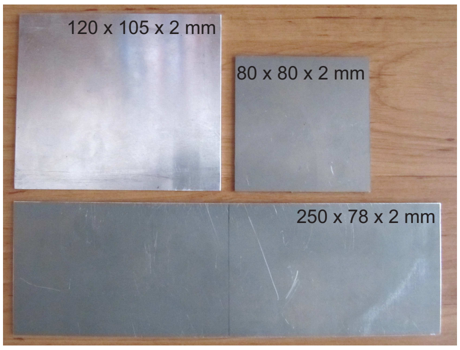

Figure 4.16: Metal plates used for FF RCS measurements.

Dimensions of the selected plates, as well as their dimensions in term of maximum and minimum wavelengths λ_{max}, λ_{min} (corresponding to lowest and highest frequencies 3 GHz and 18 GHz respectively), are stated in Tab. 4.3. Furthermore, corresponding minimum FF ranges R_{FF} and actual measurement ranges R_0 are also presented. They are expressed in terms of FF range (for λ_{max} and λ_{min}) as well.

Table 4.3: Dimensions of targets and distances min. R_{FF} and R_0.

Dim.(mm)	Dim. (xλ_{max}, xλ_{min})	R_{FF} (m)	R_0 (m)	R_0(xR_{FF})
80 x 80	0.80 x 0.80, 4.80 x 4.80	0.26 - 1.54	2.0	7.81 - 1.30
120 x 105	1.20 x 1.05, 7.20 x 6.30	0.51 - 3.05	2.0	3.93 - 0.66
250 x 78	2.50 x 0.78, 15.00 x 4.68	1.37 - 8.23	3.5	2.55 - 0.43

Minimum FF distances for maximum (diagonal) dimensions of plates are depicted in Fig. 4.17. It can be seen, that for 2 m measurement range (dashed line), only smallest plate meets FF criteria, whereas plate of dimensions 120x105 mm is measured in FF range R_{FF} up to 12 GHz and approximately up to 7.5 GHz in case of 250x78 mm plate. First two targets are measured at distance 2 m whereas long plate at 3.5 m (dashed line). Thus, in terms of R_{FF}, measurements of the targets are undertaken at distances approximately $\mathbf{7.81}R_{FF} - \mathbf{1.3}R_{FF}$, $\mathbf{3.93}R_{FF} - \mathbf{0.66}R_{FF}$ and $\mathbf{2.55}R_{FF} - \mathbf{0.43}R_{FF}$. According to Fig. 2.13, main- and sidelobes of resulting RCS should be properly determined, only nulls should be shallow.

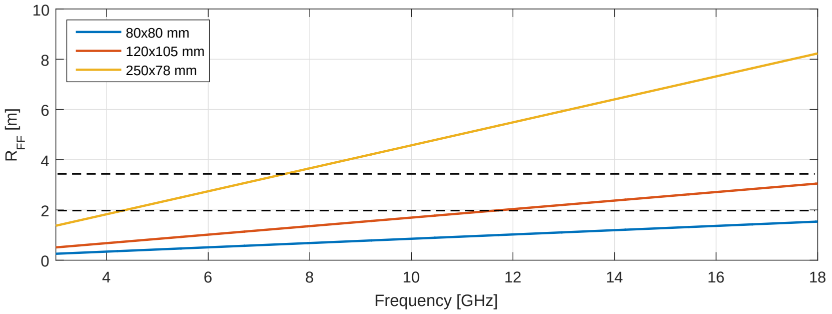

Figure 4.17: Minimum FF distances for maximal dimensions of plates.

RCS of measured targets are compared to results obtained from numerical CST models and with analytical formula for maximum mono-static RCS of the flat plates, that is written as:

$$\sigma_{plate} = \frac{4\pi w^2 h^2}{\lambda^2} \tag{4.12}$$

In the next part, resulting RCSs of metal plates of different sizes within given frequency span are presented. However, RCS cannot be determined correctly for utmost frequencies of bandwidth (3 and 18 GHz) due to time gating process. Therefore, only frequency range from 4 to 17 GHz will be use here for RCS comparison.

RCS of 80x80 mm Plate

Based on the RCS correction process outlined in Fig. 4.15, following figures represent comparison of measured RCS and their comparisons with numerical data obtained from CST model of the plate successively at selected frequencies 4, 5, 10, 15 and 17 GHz, see Fig. 4.18 - 4.22. Owing to symmetry of targets, results are depicted only within (-90°,90°) azimuthal span with step 0.5°. Furthermore, they are normalized to 0 dB for comparison purposes. Very good agreement of measured and modeled RCS can be observed at lower frequencies. Here, difference across whole azimuth is less than 0.5 dB. At higher frequencies (10, 15, 17 GHz) level of sidelobes differs about 1 dB or less.

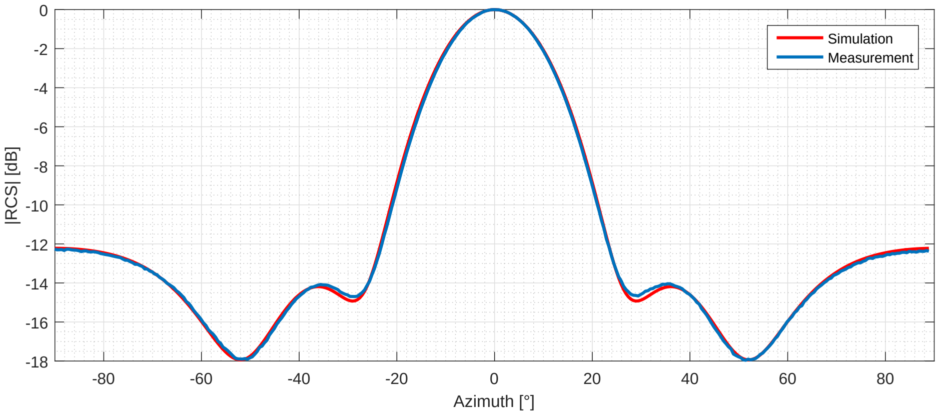

Figure 4.18: Measured RCS of 80x80 metal plate at 4 GHz and its num. model.

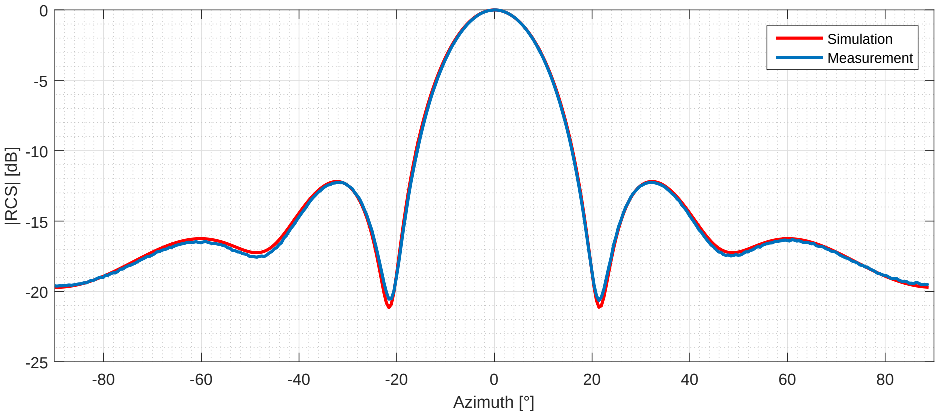

Figure 4.19: Measured RCS of 80x80 metal plate at 5 GHz and its num. model.

More considerable changes are evident in nulls of the patterns. Differences of sharp nulls of first few sidelobes are caused by both, insufficient distance of the target and antenna and wide azimuthal step (in measurement as well as in simulation). On the other hand, differences in slowly varying peaks and nulls (evident in Fig. 4.20 around ±60°) may be introduced by sum of uncertainties from measurement to data post-processing and also by finite accuracy of numerical model.

Observable ripples at higher frequencies occurring approx. below -23 dB and less signify that the signals were measured near noise level. Inaccurate initial positioning of target then gives a rise of slight asymmetry in RCS patterns.

Recovered absolute RCS values (within measured frequency span) by means of normalization technique presented above in subsection 4.2.4, are compared with

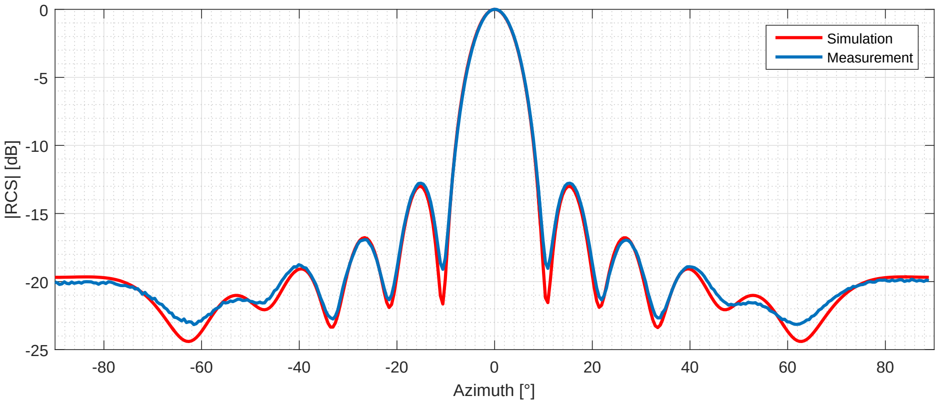

Figure 4.20: Measured RCS of 80x80 metal plate at 10 GHz and its num. model.

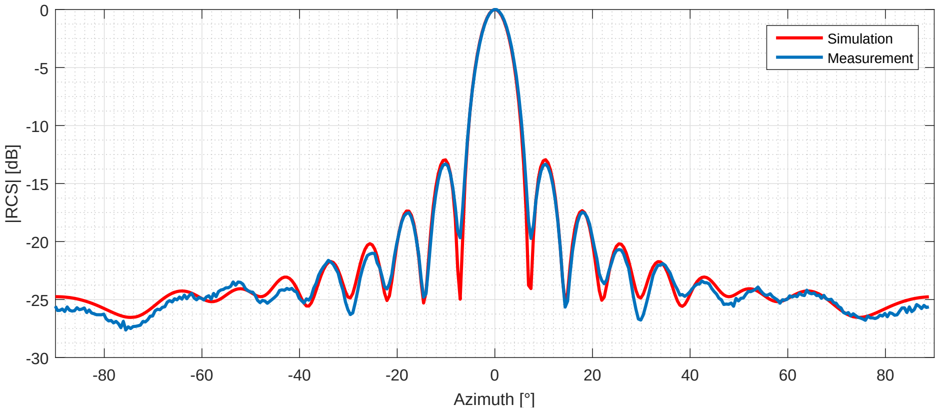

Figure 4.21: Measured RCS of 80x80 metal plate at 15 GHz and its num. model.

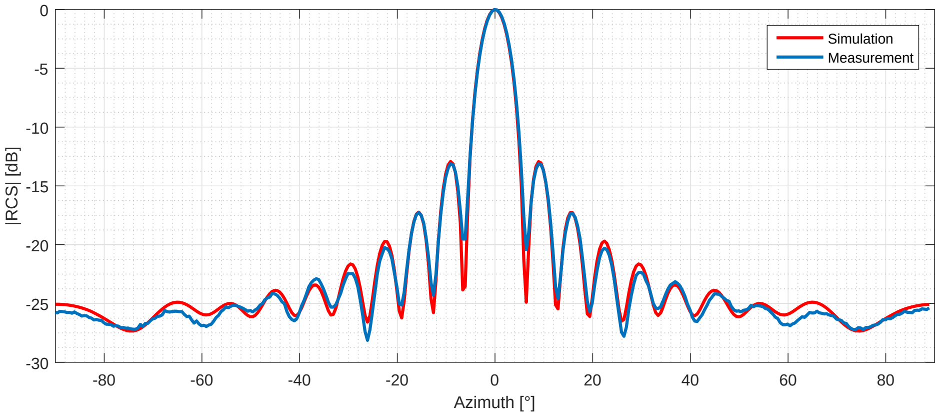

Figure 4.22: Measured RCS of 80x80 metal plate at 17 GHz and its num. model.

modeled case and with analytical model, see Fig. 4.23. Traces are valid for target oriented perpendicularly towards antenna (maximum RCS). Applying normalization process, the effect of free space loss (FSL) and two-path antenna response (or gain) is corrected. It need to be mentioned, that only antenna response at zero azimuth (at main radiation direction) is used. Time gating process and periodical spectrum

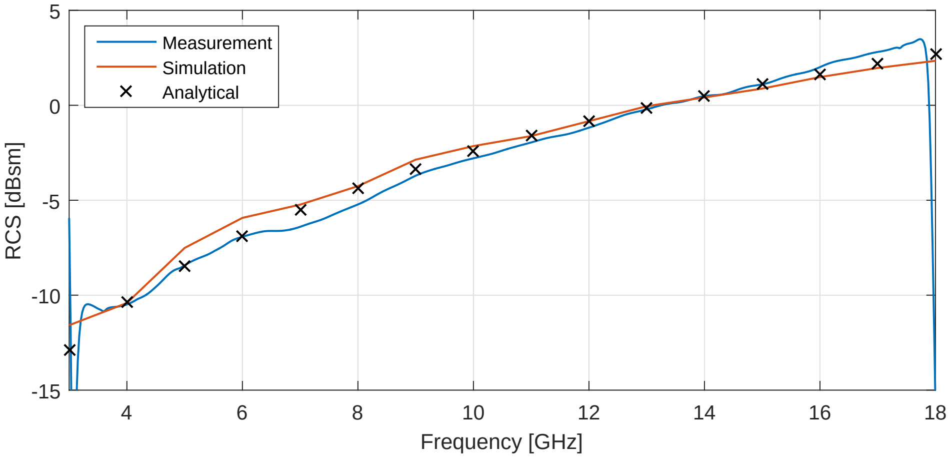

Figure 4.23: Maximum RCS of 80x80 mm metal plate measured in FF condition - comparison with its numerical model in CST and analytical value.

suppress the signal at the edges of frequency bandwidth. Mismatch of modeled and theoretical values comes out of from accuracy of simulation process - CST model, surface meshing, used integral solver employing MLFMM approach etc.

RCS of 120x105 mm Plate

FF RCSs of 120x105 mm plate are assumed to be computed from measured data up to approximately 12 GHz according to FF criteria. However, FF RCS should be correctly retrieved even at 18 GHz (that is actually measured $0.67R_{FF}$ away from atnenna), only nulls will have not as sharp minimum as "true" FF RCS patterns would have. It can be seen on following figures (Fig. 4.24 - 4.26), where measured RCS traces are depicted for frequencies 5, 10 and 15 GHz.

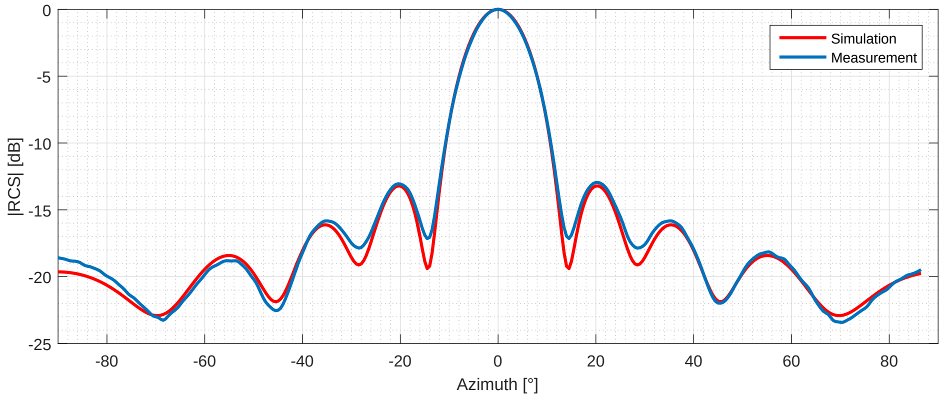

Figure 4.24: Measured RCS of 120x105 metal plate at 5 GHz and its num. model.

Figures show comparatively same results as in previous case except more shallow nulls as expected. Slight imbalance in RCS level at ±90° are caused by imperfect target centering on the turnable support or even centering of gating window and target response in data post-processing step. Levels of nulls increase as frequency

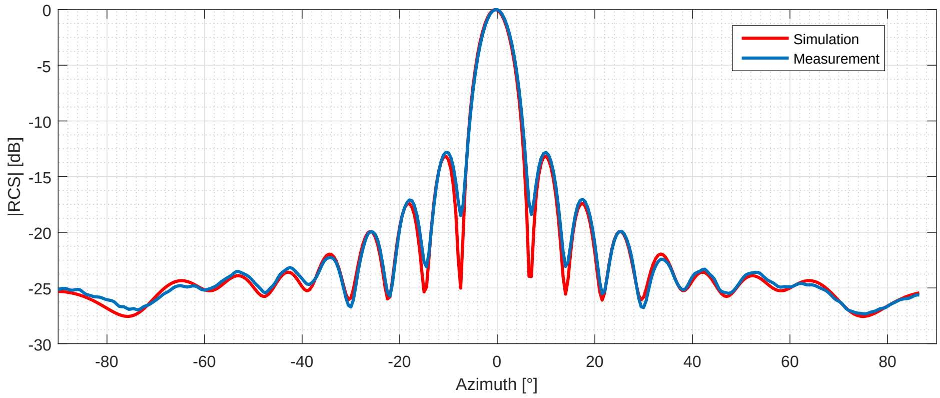

Figure 4.25: Measured RCS of 120x105 metal plate at 10 GHz and its num. model.

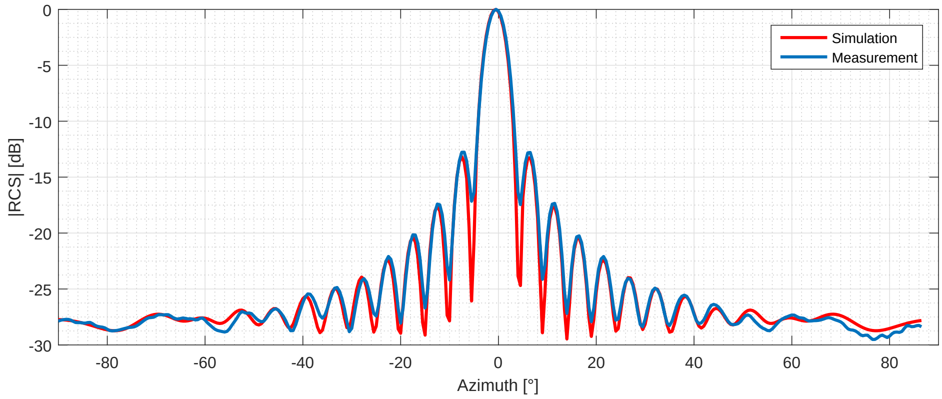

Figure 4.26: Measured RCS of 120x105 metal plate at 15 GHz and its num. model.

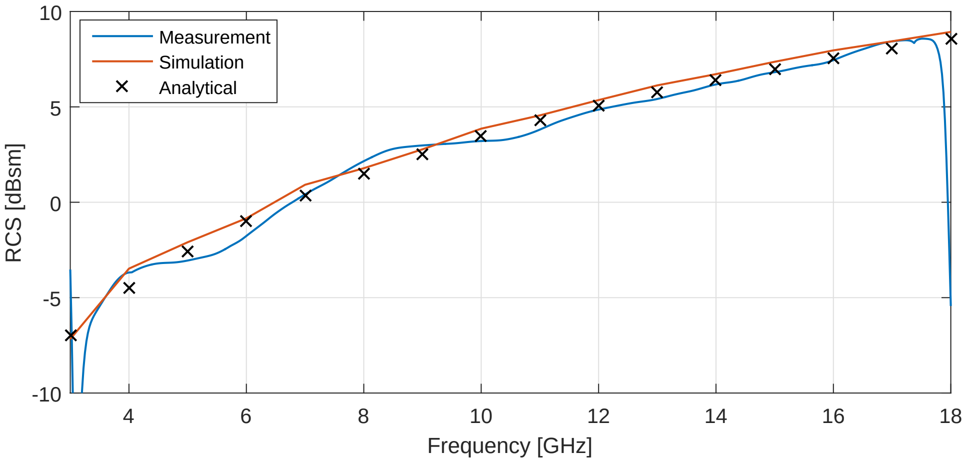

Figure 4.27: Maximum RCS of 120x105 mm metal plate measured in FF condition - comparison with its numerical model in CST and analytical value.

grows. Besides the evident NF effect, it can be also caused by insufficient azimuthal sampling.

Comparison of absolute RCS values versus frequency, shown in Fig. 4.27, is similar to case above with same errors that influence accuracy of result.

RCS of 250x78 mm Plate

Dependency of the measurement range on resulting RCS values is shown in the next case. The plate, 250 mm long and 78 mm high is employed as a target. RCSs are calculated from data measured at distances 3.5 m, 2.5 m and 1.5 m, that is $\mathbf{2.55}R_{FF} - \mathbf{0.43}R_{FF}$, $\mathbf{1.82}R_{FF} - \mathbf{0.3}R_{FF}$ and $\mathbf{1.09}R_{FF} - \mathbf{0.18}R_{FF}$ in terms of FF range. It is obvious, that the target is located more or less in NF even at 3.5 m. It can be seen in figures Fig. 4.28 - Fig. 4.30. With increasing frequency, nulls of first few sidelobes around mainlobe succesively vanishes, whereas levels of sidelobes are higher than modeled ones.

RCS measurements, carried out at distance 3.5 m, suffer from almost insufficient dynamic range for targets having low RCS. In Fig. 4.29 and 4.30 noticeable ripples occur around ±90° where the measured signals reach noise floor of measurement system.

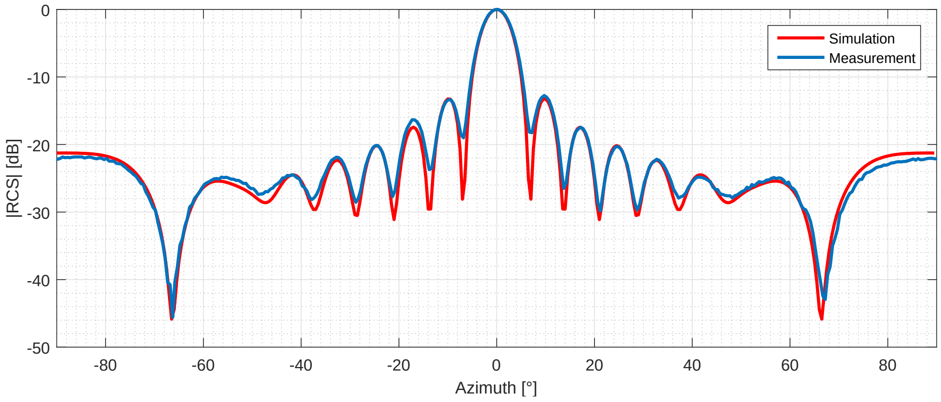

Figure 4.28: Measured RCS of 250x78 mm metal plate at 5 GHz and its num. model.

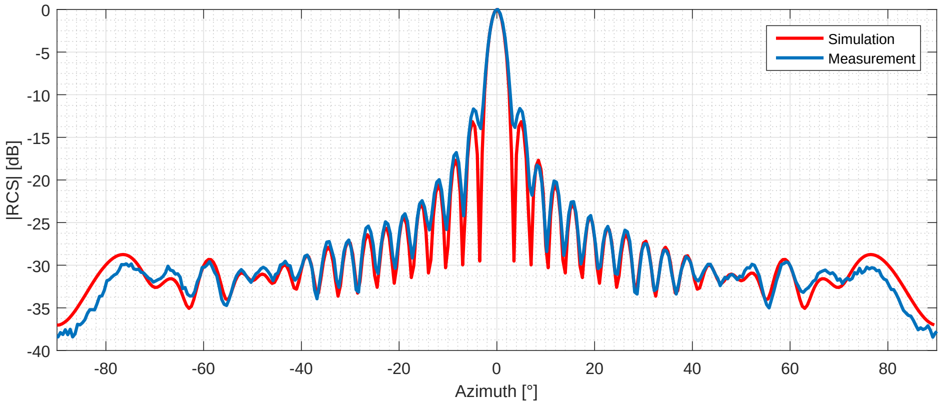

Figure 4.29: Measured RCS of 250x78 mm metal plate at 10 GHz and its num. model

Following figure (Fig. 4.31) outlines comparison of computed RCS values of the plate with respect to different measurement ranges at frequencies 5, 10 and 15 GHz respectively. NF effects are observable at all frequencies as the antenna approaches the target, however most significant changes occur around mainlobe as anticipated,

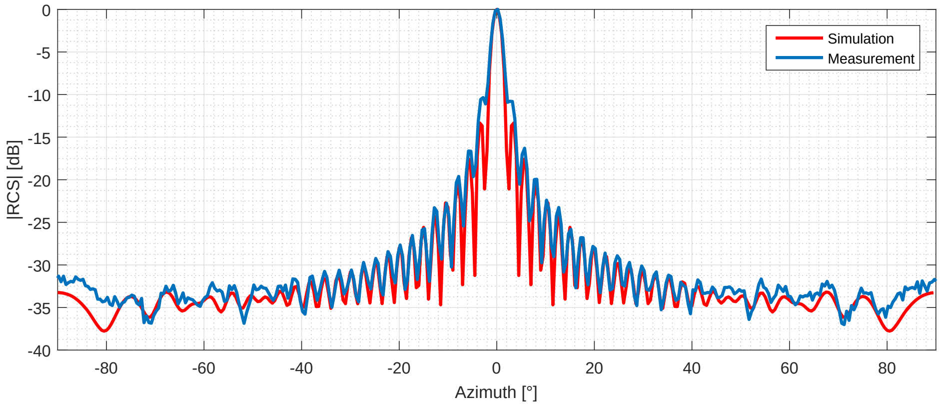

Figure 4.30: Measured RCS of 250x78 mm metal plate at 15 GHz and its num. model.

whereas rest of RCS patterns remain unchanged. Differences in patterns at the edges of azimuthal span represent sum of errors arisen from measurement and calculation process.

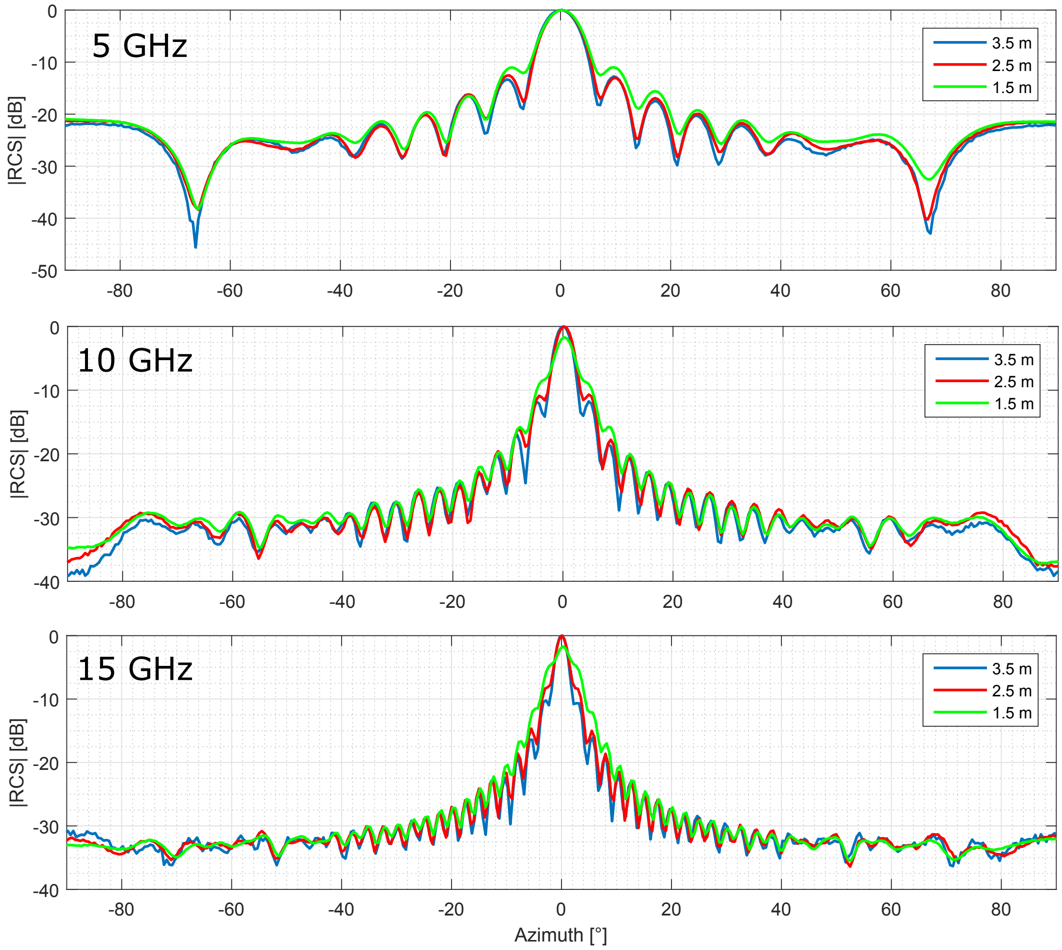

Figure 4.31: Comparison of 250x78 mm metal plate RCS at different distances - 3.5 m, 2.5 m and 1.5 m.

4.3 Intermediate Results Summary

In this part of thesis, methodology of calculating RCS patterns from high-resolution measurements, undertaken in short-range full anechoic chamber, has been proposed. Firstly, common test site has been described for both, FF and NF monostatic RCS measurements. In both cases, measured data suffer from many errors, caused mainly by unwanted reflections arisen from overall measurement path (impedance mismatches, reflections from objects surrounding the target under test, etc.). Therefore, well-known correcting techniques, namely time gating and background vector subtraction, have been described mathematically in TD and FD as well. Based on this representation, implementation of these techniques have been analyzed since their unapparent properties and restrictions (at first sight) can bring additional errors to processed data.

By implementing above mentioned techniques, accurate relative RCS values are obtained from FF measurements. Absolute RCS values are commonly retrieved from target measurements employing additional measurement of known target. However, such technique cannot be used in case of NF broadband measurement according to reasons, that have been described. Another RCS normalization technique has been proposed instead. It comprises correction of (unknown) two-way antenna response by means of transmission measurement of two identical antennas. This technique is utilized later in this thesis in antenna pattern compensation process.

Finally, validity of proposed processing scheme have been demonstrated on targets measured in FF conditions across wide frequency bandwidth. Achieved RCS patterns show agreement with numerical models of used targets.

Chapter 5

FF RCS Determination from NF Measurements

This chapter describes process of determination of FF RCS patterns obtained from NF measurements of basic targets. Basic targets are represented by objects having single-scattering characteristics - metal plates and prisms of different dimensions in this case. Firstly, proposed measurement and data correction scheme is stated. Based on CNFFFT data transformation (see section 2.3), corrected NF-FF RCS patterns of selected targets are then compared with their models.

5.1 NF-FF RCS Correction

NF to FF transformation, described in this part of thesis, is based on circular technique CNFFFT stated in section 2.3. This transform, derived from cylindrical NF measurements, comprise circular scanning of the target only in its one horizontal plane. The FF RCS is then approximated from NF data supposing additional demands and restrictions related primarily to target. While the scanning is performed only in one plane, the target height (dimension perpendicular to target rotation) is assumed to be sufficiently low - field backscattered from target is negligible in elevation compared to azimuthal plane, in which the target is scanned. Since the CNFFFT method is derived from scattering model of target, (total scattered field of the target can be described as a superposition of scattered fields from individual scattering centers distributed on target, representing its main reflective parts), only single-scattering mechanisms are taken into account. Therefore, multiple-scattering mechanisms (creeping waves, multiple reflections, waveguide modes etc.) are not taken into consideration in this case resulting in inaccurate RCS determination.

Overall computational scheme used here for NF to FF transform of NF data is outlined in Fig. 5.1. Data pre-processing (time gating, background vector subtraction) follows techniques mentioned in previous chapter.

Firstly, suppose ideal Tx/Rx antenna (infinitesimal dipole) is employed for obtaining scattered field of target (in all required azimuthal steps) as well as its background. Measured data are then gated and background signal is subtracted from

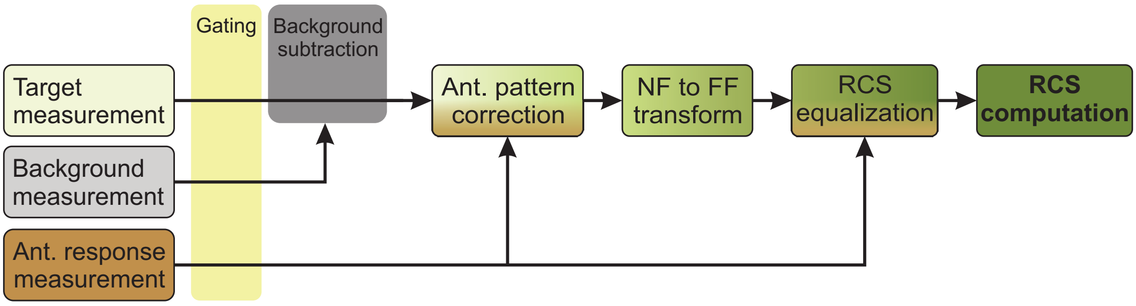

Figure 5.1: Proposed NF RCS measurement and calibration process.

target response. Then, NF to FF RCS transform is performed in order to obtain relative RCS patterns. Its scheme is depicted in Fig. 5.2, where main processing steps are stated according to section 2.3.

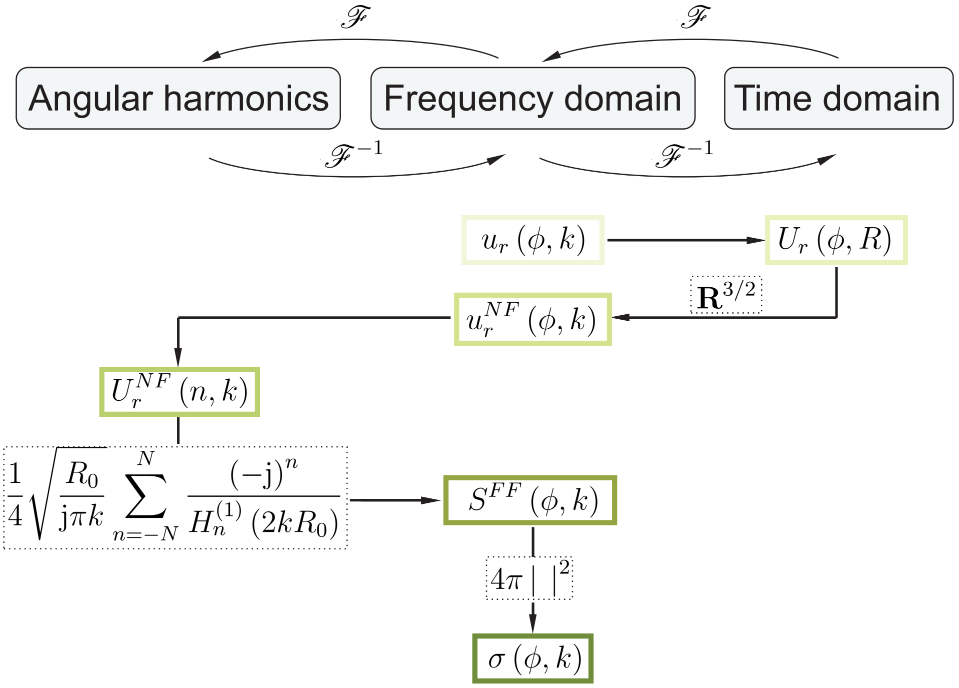

Figure 5.2: CNFFFT processing scheme.

Final estimates of relative RCS patterns $\sigma(\phi, k)$ are computed from received voltage signals $u_r(\phi, k)$ measured at particular azimuthal steps ϕ within frequency range 3 - 18 GHz (denoted by wavenumber k). These signals, transformed into TD by means of IFFT, are weighted by range factor $R^{3/2}$ and converted back into FD. This step transforms the two-way spherical wave to one-way incoming cylindrical wave - from target to antenna (Eq. (2.28)). Now, preprocessed data $u_r(\phi, k)$ need to be translated from NF to FF in angular harmonics domain. It represents Fourier image of preprocessed data along azimuthal dimension (ϕ). Now, the convolution kernel (incorporating Hankel function) is computed at each frequency point and multiplied with the corresponding angular harmonics of signal. Taking inverse FT of resulting product back to FD, FF estimation of backscattered signal $S_{FF}(\phi, k)$ is obtained.

To confirm performance of suggested aforementioned preprocessing and transformation techniques, set of NF measurements has been performed employing metal plate and two metal prisms located 1.5 m in front of measuring antenna and transformed into FF. Since the measured objects are symmetrical, only 180° azimuthal span is employed.

RCS of 250x78x2 mm Metal Plate

For the purpose of this work, metal plate of dimensions 250x78 mm, whose RCS values have been incorrectly evaluated in previous chapter, is used here in order to confirm validity of formerly proposed NF-FF transformation scheme. Following transformed RCS values result from measurement at distance 1.5 m from the antenna, that is $\mathbf{1.09}R_{FF} \ - \ \mathbf{0.18}R_{FF}$ in term of FF range for frequency span 3 - 18 GHz. Dimensions of the target are chosen to be smaller than width of mainlobe of the antenna radiation pattern in order to minimize its influence on the resulting data in whole frequency band.

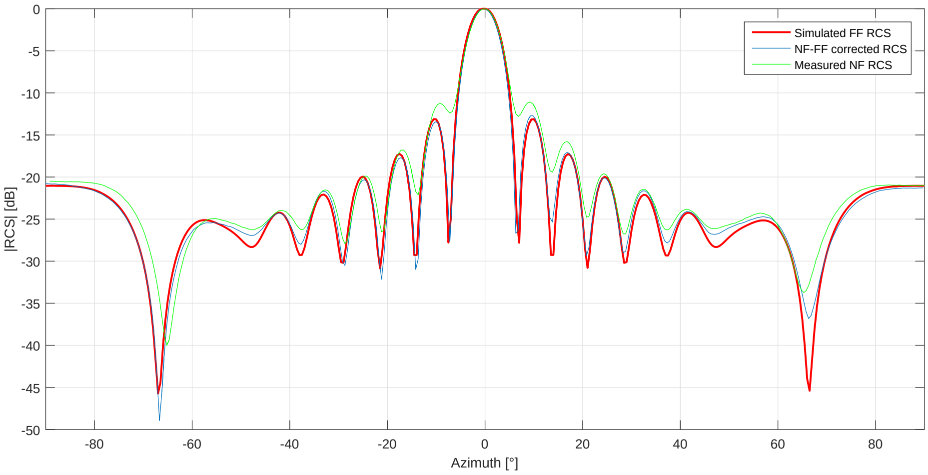

Figure 5.3: RCS of the 250x78 mm metal plate reconstructed from NF data at f = 5 GHz - comparison with CST simulation.

Fig. 5.3 depicts FF RCS result of transformation process of the plate at 5 GHz. Compared to modeled pattern, maximum error in resolving sidelobes levels is less than 0.45 dB, whereas in case of uncorrected values the error reaches up to 2.4 dB (first sidelobes level)). It is seen the nulls are restored as well across whole azimuthal range except those at ±47° due to errors arisen from inaccurate measurement and/or following post-processing, mainly by means of gating and background subtraction, since remaining correction steps do not change their settings in case of computing RCS of different targets (it can be seen on results outlined further in this section).

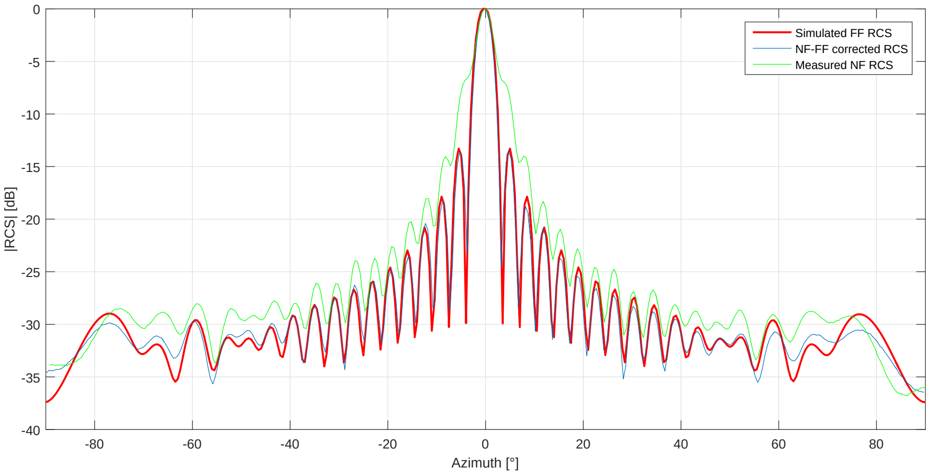

Figure 5.4: RCS of the 250x78 mm metal plate reconstructed from NF data at f = 10 GHz - comparison with CST simulation.

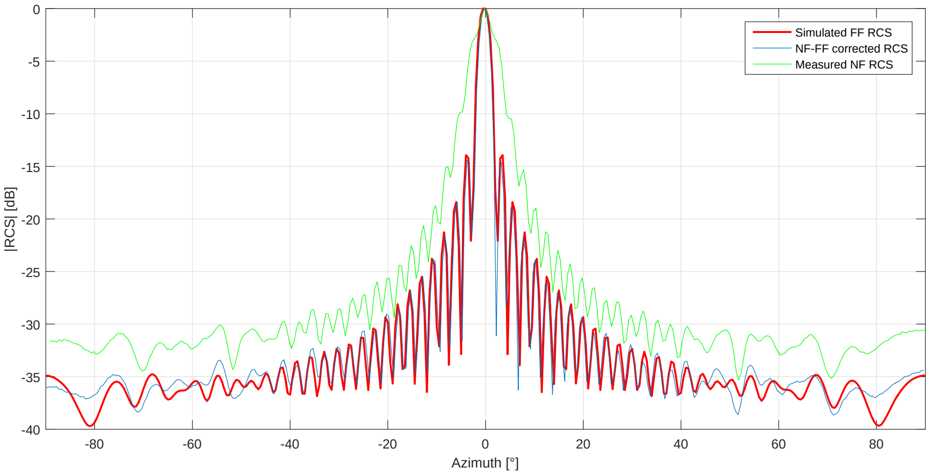

Figure 5.5: RCS of the 250x78 mm metal plate reconstructed from NF data at f = 15 GHz - comparison with CST simulation.

Analogously, comparison of NF and transformed data is depicted in Fig. 5.4 and Fig. 5.5 for 10 and 15 GHz. However, NF patterns (green lines) are normalized to their maximum values (mainlobe), even though the mainlobe level decreases with frequency due to strong NF effects, as it is outlined in Fig. 4.31. It results in incorrect sidelobe levels comparison of NF and FF data in this relative measure - sidelobes of these NF data thus seem to be higher compared to their actual position. Employing the NF-FF transform therefore increases mainlobe level that reflects on decreasing sidelobes in relative measure.

Predicted FF patterns show agreement (difference below 1 dB) with their numerical models within ±45° azimuthal range. Target positioning misalignment and additional reflections cause errors that are more significant at higher frequencies.

RCS of 425x80x80 mm and 870x40x40 mm Prism

In next step, two metal prisms (see Fig. 5.6) are measured in addition to metal plate since it has been measured at relatively far distance compared to its dimensions and only moderate NF effects have been observed.

Summary of targets lengths and ranges is tabulated in Tab. 5.1. Remaining the measurement distance unchanged (1.5 m), these targets are located only within $15\lambda_{max}$ - $91\lambda_{min}$ from the antenna. Here, λ_{max} refers to lowest frequency 3 GHz whereas λ_{min} corresponds to highest frequency 18 GHz of employed bandwidth. From the target lengths and measured distance it is obvious, that antenna is located in reactive NF of long targets. Arose errors will be discussed later.

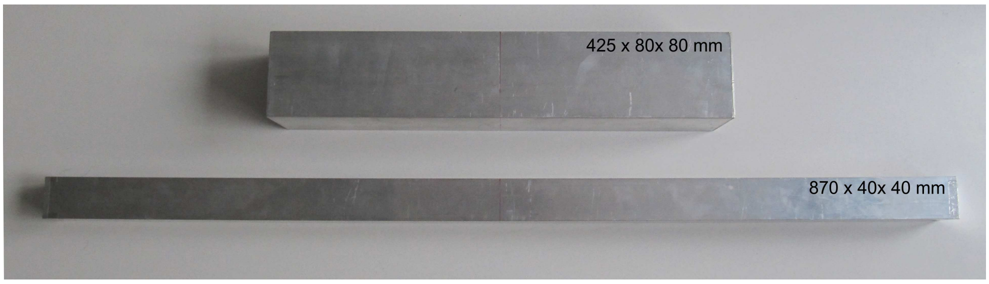

Figure 5.6: Metal prisms used for NF RCS measurements.

Table 5.1: Dimensions of targets and distances min. R_{FF} and R_0.

Dim.(mm)	Dim. (xλ_{max}, xλ_{min})	R_{FF} (m)	R_0 (m)	R_0(xR_{FF})
425 x 80 x 80	4.25 x 0.80, 25.50 x 4.80	3.74 - 22.44	1.5	0.535 - 0.089
870 x 40 x 40	8.70 x 0.40, 52.20 x 2.40	15.17 - 91.02	1.5	0.100 - 0.017

Targets are measured at distance 1.5 m that corresponds to $1.72L$ - $3.53L$ multiple of targets lengths L and $15\lambda_{max}$ - $90\lambda_{min}$ in wavelengths. However, their FF range R_{FF} is then 3.74 m - 22.44 m and 15.17 m - 91.02 m respectively. Thus, in terms of R_{FF}, measurements of the targets are undertaken at distance approximately $\mathbf{0.535}R_{FF} - \mathbf{0.089}R_{FF}$ or $\mathbf{0.1}R_{FF} - \mathbf{0.017}R_{FF}$. According to Fig. 2.13, values of both, nulls and maximums of main- and side-lobes should not be determined correctly in resulting NF RCS compared to FF case.

Following figures show RCS patterns of prisms before and after NF-FF transform for selected frequencies 5, 10 and 15 GHz. Results are compared to numerically evaluated RCS values using FEKO software.

Fig. 5.7 - 5.9 represent comparison of estimated RCSs of 425x80x80 mm prism with their theoretical (simulated) and NF RCS values. Depicted NF patterns are computed directly from measured data (only after gating and background subtraction).

As it is seen in Fig. 5.7, shorter prism is located relatively far from antenna in terms of FF range ($0.24R_{FF}$) compared to higher frequencies. Amplitude levels of main- and side-lobes are perfectly restored from NF data in azimuthal range ±40° with error less than 0.2 dB at main-lobes. Difference between reconstructed RCS and numerical model at around ±60° originates from the fact the target is oriented towards to antenna in way that reflected signal starts to interact with the surrounding objects (mainly flat absorbers in this case) and it results in interference of different backscattered signals. This is also indicated in RCS pattern by alternating levels of sidelobes. This phenomenon disappear when the target aligns parallel to antenna and its backscattered field from becomes stronger. This error grows with length of target and increasing frequency and it cannot be easily mathematically suppressed. It will be shown later on in this section.

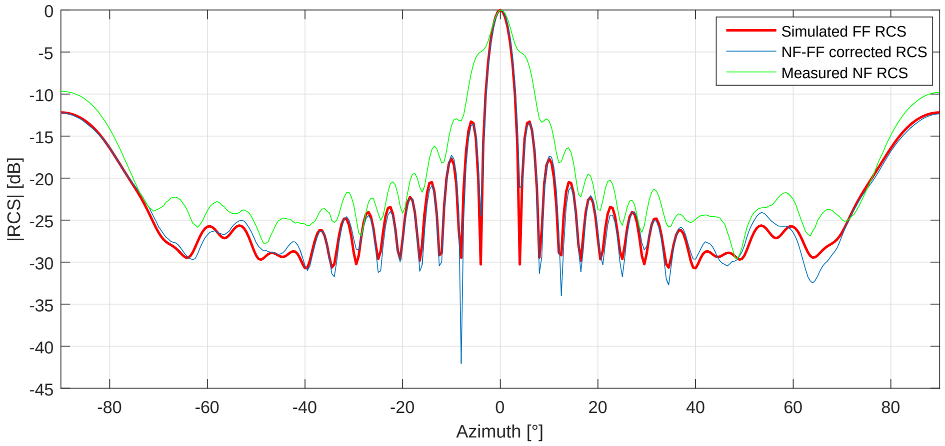

Figure 5.7: RCS of the 425x80x80 mm prism reconstructed from NF data at f = 5 GHz - comparison with FEKO simulation.

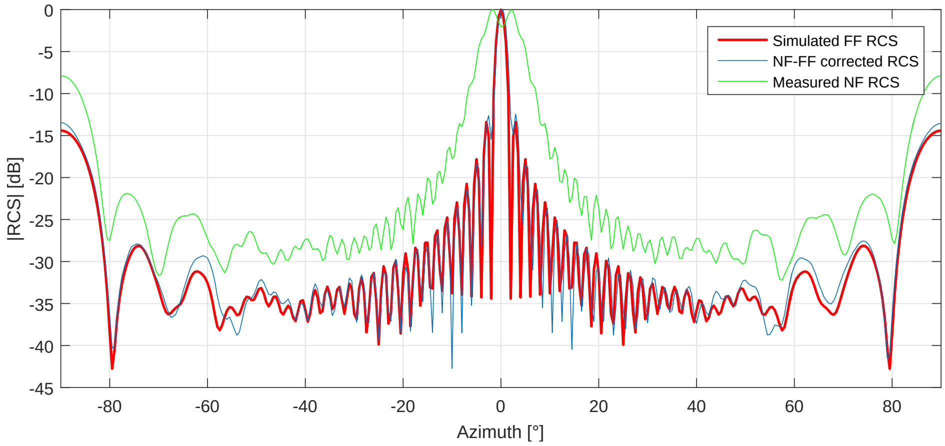

Figure 5.8: RCS of the 425x80x80 mm prism reconstructed from NF data at f = 10 GHz - comparison with FEKO simulation.

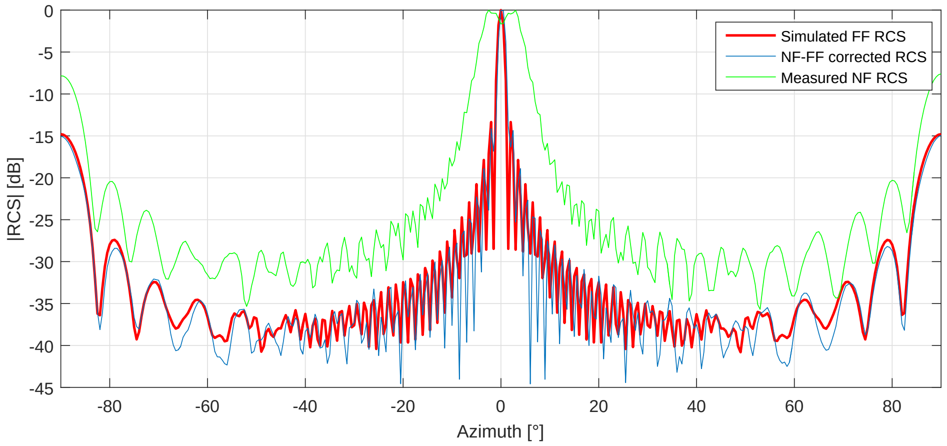

Figure 5.9: RCS of the 425x80x80 mm prism reconstructed from NF data at f = 15 GHz - comparison with FEKO simulation.

The interference error is also evident at higher frequencies, see Fig. 5.8 and Fig. 5.9), where RCSs of short prism are depicted for frequencies 10 and 15 GHz. In both cases, restored NF-FF RCSs correspond to their numerical values in almost whole azimuthal range. However, due to insufficient azimuthal sampling (in terms of plotting), amplitudes of side-lobes are incorrectly depicted. It occurs, when the spacing of adjacent nulls exceeds angular sampling step. Obvious side-lobes misalignment occurs more significantly at around ±60° compared to previous case.

Effect of NF-FF algorithm can be demonstrated by Fig. 5.10, where reconstructed RCS of short prism as a function of frequency and azimuth is stated.

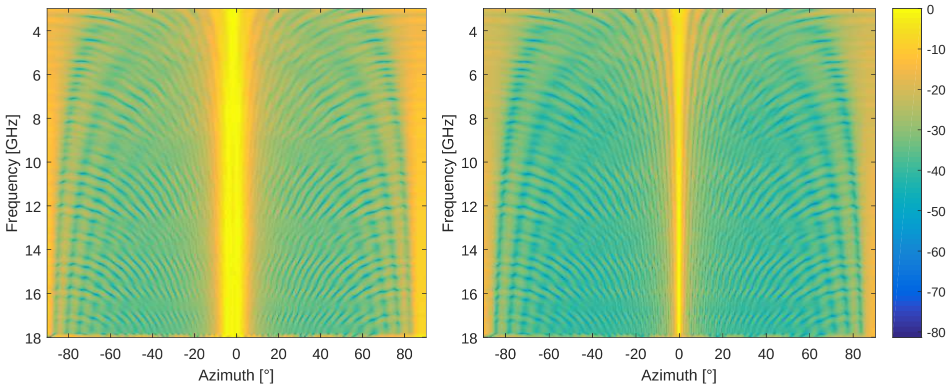

a) b)

Figure 5.10: RCS of the 425x80x80 mm prism - comparison of: a) NF RCS data with b) NF-FF corrected RCS patterns.

Absolute RCS values of the short prism across measured frequency bandwidth are shown in Fig. 5.11. Maximum difference of computed and modeled RCS does not exceed 1.5 dB in whole bandwidth except at utmost frequencies where RCS values are distorted by process of time gating.

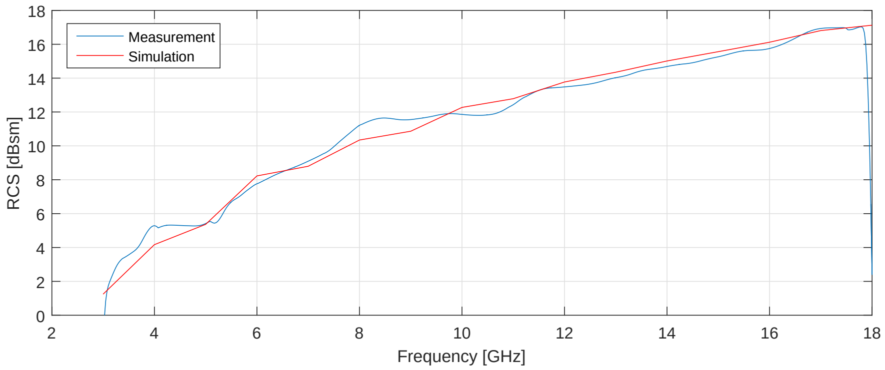

Figure 5.11: Maximum RCS of the 425x80x80 mm prism reconstructed from NF data - comparison with FEKO simulation.

Results concerning long, 870x40x40 mm prism are presented in same manner as in case of short one. It is measured at distances $0.1R_{FF} - 0.017R_{FF}$. It means that target is already measured in reactive NF. Such short measurement range leads to more inaccurate transformed FF RCS patterns (Fig. 5.12 - Fig. 5.14), since only one part of the field is measured (vertically polarized).

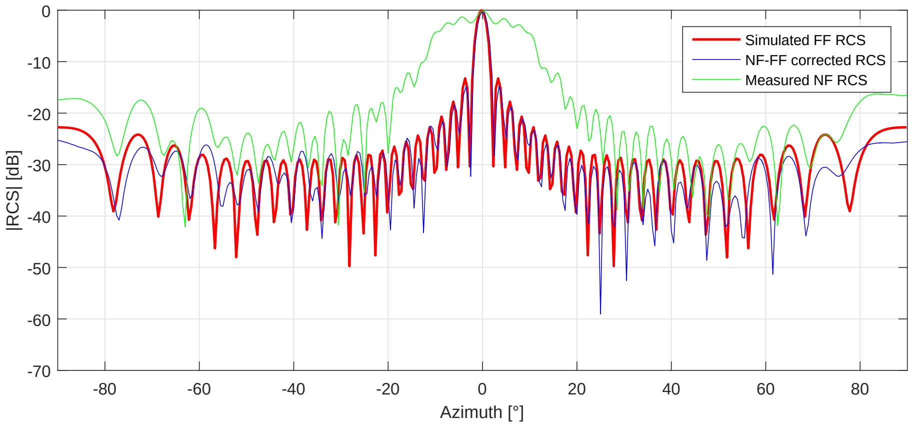

Figure 5.12: RCS of the 870x40x40 mm prism reconstructed from NF data at f = 5 GHz - comparison with FEKO simulation.

Both, amplitude and position of side-lobes are more misaligned compared to FF RCS values as measurement frequency increases. Besides the interference errors causing misalignment and asymmetrical amplitude level of the side-lobes, very short measurement range causes also their broadening. Therefore, these results cannot be used for precise localization of sidelobes positions. Nevertheless, their amplitude more-or-less corresponds to modeled patterns and can be thus utilized i.e. for statistical purposes.

In addition, impact of directional antenna pattern is observable in results: since the target is illuminated non-uniformly in amplitude and phase, scattered field suffers from tapering error, especially when the target is perpendicularly oriented to antenna in this case. It results typically in lower the utmost sidelobes levels of RCS pattern.

This error rises with frequency as the antenna mainlobe narrows. Moreover, asymmetry of computed patterns is caused mainly by misalignment of the target on rotary support and also by asymmetric arrangement of object located in vicinity of target.

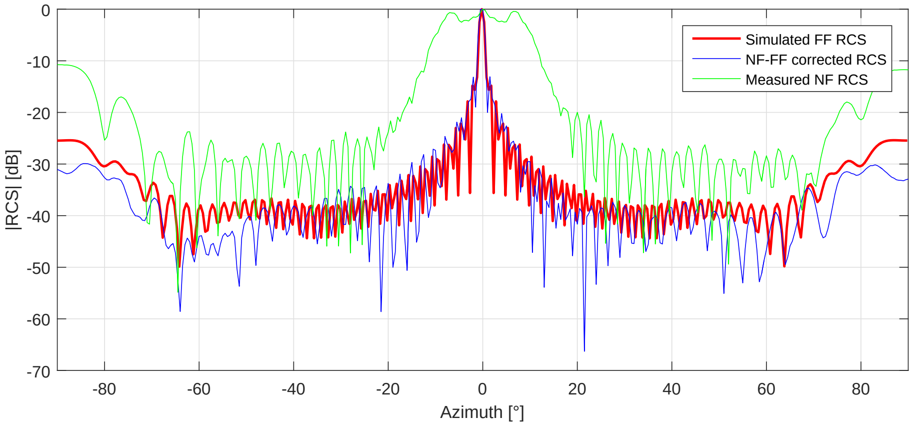

Figure 5.13: RCS of the 870x40x40 mm prism reconstructed from NF data at f = 10 GHz - comparison with FEKO simulation.

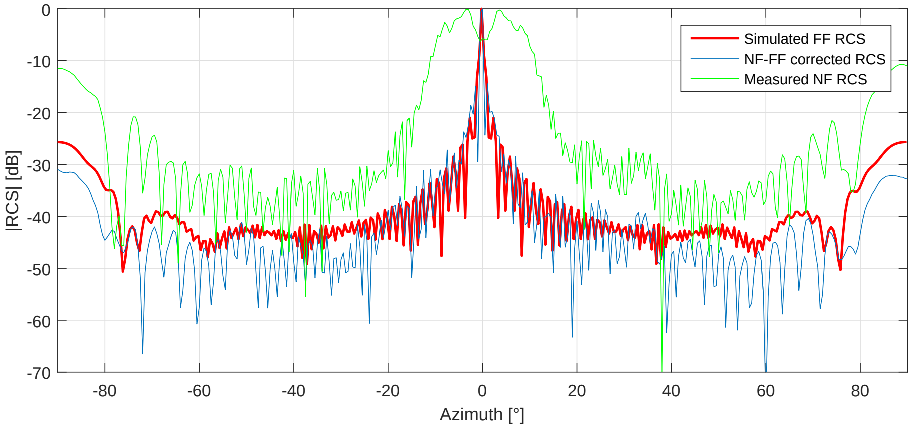

Figure 5.14: RCS of the 870x40x40 mm prism reconstructed from NF data at f = 15 GHz - comparison with FEKO simulation.

Reconstructed RCS of long prism as a function of frequency and azimuth (Fig. 5.15) shows artifacts, that remain unchanged compared to unprocessed data. These are introduced mainly by interference mechanisms as stated earlier. Frequency dependence of retrieved maximum absolute RCS pattern is depicted in Fig. 5.16). Obvious ripples are introduces by NF errors and measurement sensitivity.

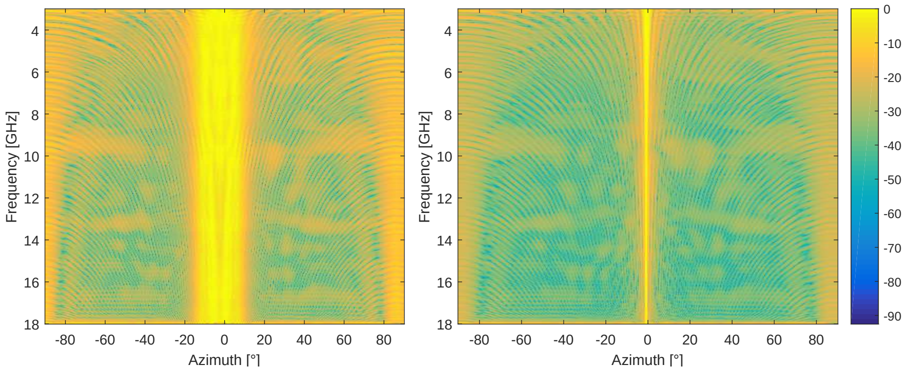

a) b)

Figure 5.15: RCS of the 870x40x40 mm prism - comparison of: a) NF RCS data with b) NF-FF corrected RCS patterns.

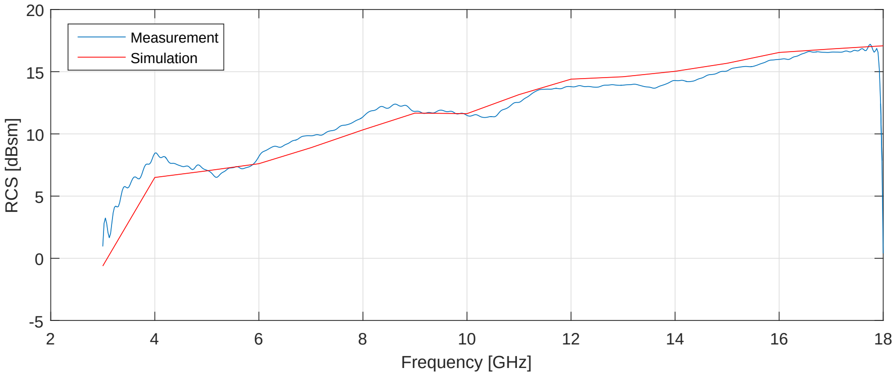

Figure 5.16: Maximum RCS of the 870x40x40 mm prism reconstructed from NF data - comparison with FEKO simulation.

5.2 Intermediate Results Summary

Existing full anechoic chamber at the department of Electromagnetic field at CTU in Prague allows to measure FF single-plain RCS patterns of targets having limited dimensions due to short test range. Practically, these restriction lead to employ NF measurement technique with subsequent FF extrapolation post-processing. Therefore, CNFFFT technique has been adopted in this thesis for transforming NF data into FF RCS pattern. Following stated theoretical background, NF to FF processing scheme has been outlined.

Till now, validity of this technique has been confirmed primarily by numerical simulations [60], [61], [84], [85] and only few papers deal with real measurements. Moreover, they show performance only in restricted azimuthal and frequency span. Based on these facts, broadband NF measurements (15 GHz span) of long test targets have been undertaken at very short distance that ranges from $0.4R_{FF}$ to $0.017R_{FF}$ according to frequency. Following that, targets have been measured in both, radiative and reactive NF and arisen differences with modeled FF RCS patterns have been discussed. Results of NF-FF processing still have shown very good correspondence with modeled targets. Furthermore, they have revealed errors caused by interactions of target and background objects and also impact of radiation patterns of test antenna. Last mentioned is subject of further compensation technique stated later on.

Chapter 6

Antenna Characterization and Compensation in NF-FF RCS Transformation

This thesis deals with measurement of electrically large targets (in azimuthal plane) compared to measurement distance. Furthermore, to obtain wideband reflection data, antenna with appropriate operational bandwidth need to be employed. In this case, broadband double-ridged horn antenna is used. It has relatively high directivity that increases with frequency. Contrary to FF RCS measurements, in NF this antenna thus performs a weighted spatial averaging of scattered field that is accordingly received. This phenomenon can lead to obtaining incorrect amplitude and phase of measured field and need to be suppressed by means of antenna compensation process.

This chapter therefore firstly describes novel method for calculation of antenna frequency/impulse responses from measurements undertaken in both, TD and FD. Based on this, broadband antenna radiation patterns are obtained. Furthermore, description of time (spatial) antenna characteristics brings another information usable in NF scanning. Accordingly, antenna compensation is implemented to NF-FF scheme.

6.1 Antenna Characterization by Means of its Impulse Response

Broadband RCS measurements involve employing antenna that can operate in whole required frequency bandwidth. Radiation pattern of such antenna varies with increasing frequency - main beam typically narrows together with increase of sidelobes number. In many cases, dimensions of the target are much larger than size of antenna aperture, that is mostly located in NF of the target. Therefore the target is unevenly illuminated by spherical wave. It can introduce significant errors in reconstruction of the FF RCS from NF measurements. These undesirable effects need to be compensated based on the knowledge of antenna radiation patterns across required frequency band.

Next part therefore proposes obtaining azimuth-dependent TD impulse responses of antenna based on three basic measurement methods:

- three antennas method,
- two identical antennas method,
- reference antenna method (gain transfer method).

Results are then compared with measurements carried out in FD domain.

6.1.1 Transmission Model Between Two Antennas

The transmission model between two antennas can be expressed by appropriate equations as a Linear Time Invariant (LTI) system. It is possible to elaborate the model separately for receive and radiation modes, [89], [90], [91]. The received voltage $u_{rx}(t)$ in the receive mode can be expressed in the time domain as follows:

$$\frac{u_{rx}(t)}{\sqrt{Z_C}} = h_{rx}(t,\phi_{rx},\theta_{rx}) * \frac{\mathrm{e}_i(t,\phi_i,\theta_i)}{\sqrt{Z_0}} \tag{6.1}$$

where Z_C is the characteristic port impedance, Z_0 denotes the characteristic impedance of free space (which equals 120 π), $e_i(t,\phi_i,\theta_i)$ stands for the electric field of incident wave in the time domain from the direction (ϕ_i,θ_i), $h_{rx}(t,\phi_{rx},\theta_{rx})$ represents the normalized effective height of the antenna in receive mode. The electric field $e_{tx}(t,r,\phi_{tx},\theta_{tx})$ of radiated waves at the distance r from the direction (ϕ_{tx},θ_{tx}) can be expressed by the following equation:

$$\frac{\mathrm{e}_{tx}(t,r,\phi_{tx},\theta_{tx})}{\sqrt{Z_0}} = \frac{1}{r}\delta\left(t-\frac{r}{c_0}\right) * \mathrm{a}_n(t,\phi_{tx},\theta_{tx}) * \frac{u_{tx}(t)}{\sqrt{Z_C}} \tag{6.2}$$

Z_C stands for the characteristic port impedance, while $u_{tx}(t)$ represents the voltage of transmit impulse. The factor $a_n(t,\phi_{tx},\theta_{tx})$, which includes the antenna directional, polarization and radiation properties, is formulated in the following manner:

$$a_n(t,\phi_{tx},\theta_{tx}) = \frac{1}{2\pi c_0}\frac{\partial}{\partial t}\mathrm{h}_{tx}(t,\phi_{tx},\theta_{tx}) \tag{6.3}$$

Here, $h_{tx}(t,\phi_{tx},\theta_{tx})$ corresponds to the normalized effective height of the transmit antenna. Consequently, the overall transmission model is depicted in Fig. 6.1. The transmission equation of this model can be, in both, time and frequency domains, expressed from Eq. (6.1) - (6.3) by the equations listed below. The variables $h_{ch}(t)$ and $H_{ch}(\omega)$ represent the impulse response and frequency response of the channel. For further considerations, impulse responses obtained at zero elevation and azimuth angles of transmit as well as receive antenna are going to be taken into consideration.

$$\begin{aligned} u_{rx}(t) = \sqrt{\frac{Z_{C,rx}}{Z_{C,tx}}}\mathrm{h}_{rx}(t,\phi_{rx},\theta_{rx}) * \frac{1}{2\pi r_{txrx} c_0}\delta\left(t-\frac{r_{txrx}}{c_0}\right) \\ * h_{ch}\left(t\right) * h_{tx}(t,\phi_{tx},\theta_{tx}) * \frac{\partial}{\partial t}u_{tx}(t) \end{aligned} \tag{6.4}$$

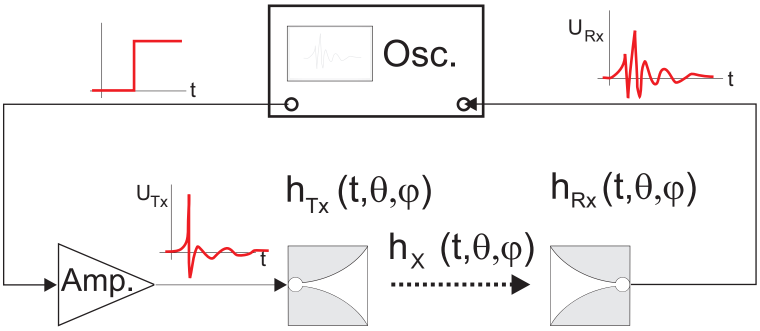

Figure 6.1: Transient channel of the impulse response measurement.

$$U_{rx}(\omega) = \sqrt{\frac{Z_{C,rx}}{Z_{C,tx}}} H_{rx}(\omega, \phi_{rx}, \theta_{rx}) \frac{\mathrm{e}^{-\mathrm{j}\omega r_{rxtx}/c_0}}{2\pi r_{rxtx} c_0} \cdot H_{ch}(\omega) \cdot \mathrm{j}\omega H_{tx}(\omega, \phi_{tx}, \theta_{tx}) U_{tx}(\omega) \qquad (6.5)$$

6.1.2 Transmission Measurement in Frequency Domain

The transmissions between two antennas in the frequency domain (FD) can be simply measured by means of the VNA ZVA40. The obtained parameters can be transformed into the time domain using the Fourier transform. The results are then impulse responses to the ideal Dirac impulse.

To correct systematic errors of transmission parameters measurement, the most common method, called Open-Short-Load-Transmission (SOLT) method, in other words also Open-Short-Match-Line (OSML), is used.

6.1.3 Transmission Measurement in Time Domain

The measurement in the time domain (TD) is carried out using the wideband scope Agilent DCAJ86100C with TDR/TDT module 54754A (with the frequency bandwidth of up to 18 GHz). The latter is used as a sharp step generator (its rise time is approx. 40 ps with amplitude of approx. 200 mV) in the TD transmission (TDT) mode. Commonly, the impulse response $h(t)$ of any measured circuits represents the circuit response simulated or measured with the Dirac impulse excitation. In case of the ideal step/edge excitation, the impulse response $h(t)$ equals the derivative of the step response (obtained with the ideal step excitation - measured by the TDT module). In this case, the sharp edge from TDT module is transformed to impulse and amplified by means of the wideband amplifier MINICIRCUITS ZVA-213-S+ working within the frequency range of 0.8 GHz - 21 GHz. The overall system is depicted in Fig. 6.2. The resulting signal is then used as the excitation impulse; see Fig. 6.3. Its spectrum is shown in Fig. 6.4. The usable parts of the spectra ranges from 0 to approximately 18 GHz. Higher spectral components with amplitudes that are hundred times smaller than the maximum can give rise to ambiguities in transmission scattering parameter calculation; see Eq. (6.5) and Eq. (6.6). This usable spectrum almost covers the operational bandwidth of measured antennas.

In the FD, it is possible to apply a correction method, such as SOLT or others. It is intended to correct the impedance imperfections and unwanted reflections. Only the cable lengths and dispersion were taken into account and corrected using the excitation impulse measurement through two cables (out of which the one is used for feeding of the transmitting antennas, while the other one for the receiving antenna), connected by a short adapter instead of antennas. This impulse response is consequently used as a reference for the transmission between a set of antennas. The coefficient $S_{ij}(\omega)$ signifies the evaluation by means of the Fourier transformation.

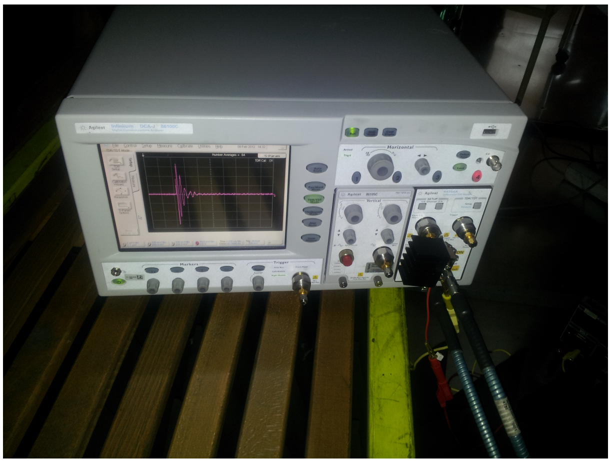

Figure 6.2: Transient response measurement with Agilent scope and low-noise amplifier.

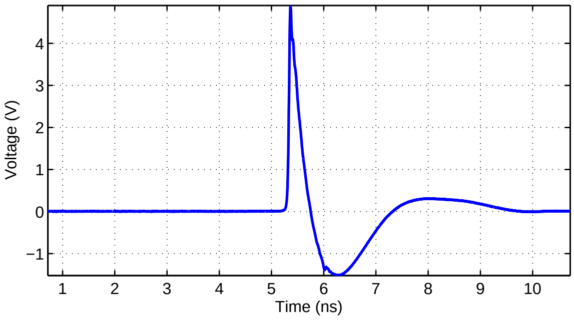

Figure 6.3: Excitation impulse in TD.

Both time and frequency domain measurements can be employed for characterization of the time or frequency domain antenna parameters. The main advantage of the time domain approach consists in the measurement speed (in the real-time scope) and direct gating of unwanted reflections. Contrary to that, the frequency domain measurements are highly beneficial in case of narrowband characteristics. In addition, a higher dynamic range can be reached with the help of VNA measurement (in FD).

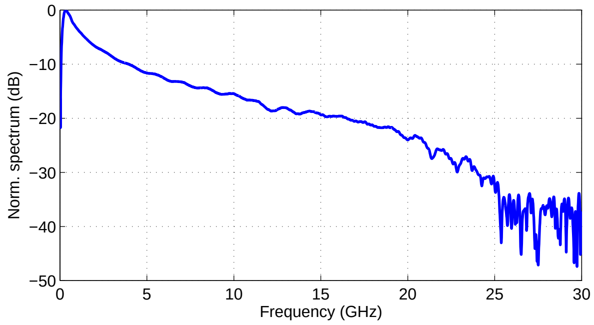

Figure 6.4: Excitation impulse in FD.

6.1.4 Three Antennas Method

The three antennas method represents a commonly used technique to precisely determine the absolute gain of three arbitrary antennas. Furthermore, it can be employed in order to obtain the TD impulse responses of antennas. In case of this method, it is required to solve three transmission equations (6.4) for all three possible pairs of antennas. Rather than performing de-convolutions, impulse responses are calculated in the FD and transferred back to the TD. With the known excitation and measured signal, the transmission scattering parameter $S_{rxtx}(\omega)$ can be evaluated from Eq. (6.5). In case of highly directive antennas and small distance between them, the channel response $H_{ch}(\omega)$ is considered to equal 1. In addition, assuming ideally co-polarized, matched antennas and equal port impedances, $S_{rxtx}(\omega)$ can be simplified and takes the following form:

$$S_{rxtx}\left(\omega\right) = H_{tx}\left(\omega\right) H_{rx}\left(\omega\right) \frac{\mathrm{j}\omega \mathrm{e}^{-\mathrm{j}\omega r/c_0}}{2\pi r c_0} \tag{6.6}$$

Impulse responses of three unknown antennas are then obtained from the measurement of all antennas combinations $S_{12}(\omega)$, $S_{23}(\omega)$ and $S_{31}(\omega)$ at a known fixed distance between the transmitting and receiving antennas:

$$h_1\left(t\right) = \mathscr{F}^{-1}\left\{\sqrt{\frac{S_{31}\left(\omega\right) S_{12}\left(\omega\right)}{S_{23}\left(\omega\right)} \frac{1}{K\left(\omega\right)}}\right\} \tag{6.7}$$

$$h_2\left(t\right) = \mathscr{F}^{-1}\left\{\sqrt{\frac{S_{12}\left(\omega\right) S_{23}\left(\omega\right)}{S_{31}\left(\omega\right)} \frac{1}{K\left(\omega\right)}}\right\} \tag{6.8}$$

$$h_3\left(t\right) = \mathscr{F}^{-1}\left\{\sqrt{\frac{S_{23}\left(\omega\right) S_{31}\left(\omega\right)}{S_{12}\left(\omega\right)} \frac{1}{K\left(\omega\right)}}\right\} \tag{6.9}$$

$K(\omega)$ denotes the constant that predominantly includes the signal differentiation and Green's function; see Eq. (6.10).

$$K\left(\omega\right) = \frac{\mathrm{j}\omega \mathrm{e}^{-\mathrm{j}\omega r/c_0}}{2\pi r c_0} \tag{6.10}$$

Equations (6.7) - (6.9) obviously show that the accuracy of the testing antenna impulse response evaluation depends on the operational bandwidth of the remaining two antennas. As the frequency components outside this operational bandwidth are mostly comparable to the noise spectrum, antennas with similar bandwidths should be used.

6.1.5 Two Identical Antennas Method

As this method calculates the impulse response of two identical antennas, it is less precise than the aforementioned technique due to "averaging" of the two responses. Nevertheless, since only one measurement is performed, errors originating from different measuring distances are eliminated. The calculation of the impulse response is then straight-forward; see Eq. (6.11).

$$h_{meas}(t) = \mathscr{F}^{-1}\left\{\sqrt{\frac{S_{21}(\omega)}{K(\omega)}}\right\} \tag{6.11}$$

6.1.6 Reference Antenna Method

This method, also known as the gain transfer technique, requires one antenna with exactly known parameters (gain or impulse response). In principle, it is necessary to undertake two measurements so that the measured antenna gain (response) can be calculated. First, the transmission between the unknown transmit antenna and reference antenna ($S_{ref}(\omega)$) is measured. Subsequently, the reference antenna (described by $H_{ref}(\omega)$) is replaced by the measured antenna and $S_{meas}(\omega)$ is measured. Its impulse response is then calculated employing the following equation:

$$h_{meas}(t) = \mathscr{F}^{-1}\left\{\frac{S_{meas}(\omega)}{S_{ref}(\omega)}H_{ref}(\omega)\right\} \tag{6.12}$$

In this case, although the channel response is canceled out, negligible reflections from an adjacent object being assumed, the channel response attains 1. In addition, the measured antenna response can be calculated only from one transmission measurement with reference antenna, see Eq. (6.12). As it is going to be indicated later in this text, the proposed method ensures over 99% agreement with the commonly applied method. It should be also noticed that the correct evaluation of the impulse response $h_{meas}(t)$ by Eq. (6.13) is valid only within the operational frequency bandwidth of the reference antenna. Otherwise negligible frequency components outside this bandwidth can give rise to significant errors.

$$h_{meas}(t) = \mathscr{F}^{-1}\left\{\frac{S_{21}(\omega)}{H_{ref}(\omega)K(\omega)}\right\} \tag{6.13}$$

6.1.7 Inpulse Responses Comparison

The differences in results computed from three aforementioned methods are evaluated by means of the so-called fidelity factor, which is mostly used to quantitatively describe the angular distortion of radiated pulse, with respect to the signal transmitted in the main beam direction, [92].

In this case, the fidelity factor is employed in order to compare the impulse responses obtained from the three measurement methods. This factor preserves the amplitude weighting and time shifting of signal and is defined as a maximal value of the weighted cross-correlation of the reference $h_{ref}(t)$ and measured response $h_{meas}(t)$; see (6.14). The weighting factor normalizes the input signals in the way ensuring their unit energies.

$$F = \max_{\tau} \left| \frac{\int\limits_{-\infty}^{\infty} h_{ref}\left(t\right) h_{meas}\left(t+\tau\right) dt}{\sqrt{\int\limits_{-\infty}^{\infty} \left|h_{ref}\left(t\right)\right|^{2} dt \int\limits_{-\infty}^{\infty} \left|h_{meas}\left(t\right)\right|^{2} dt}} \right| \tag{6.14}$$

The comparison of three basic measuring methods is demonstrated with three identical double ridged horn (DRH) antennas DRH20 operating in the bandwidth of 1.7 - 20 GHz [88], two larger Vivaldi antennas *V1* and *V2* designed by Sokol and Piksa [93] (3.1 - 10.6 GHz) and three small Vivaldi antennas *v1*, *v2* and *v3* (3.1 - 10.6 GHz); [94], [95], [96]. The last mentioned are non-identical due to their different feeding, where *v1* has a classical radial stub to circular stub transition and antennas *v2* and *v3* have a via to slot-line transition. All respective antennas are depicted in Fig. 6.5 and Fig. 6.6.

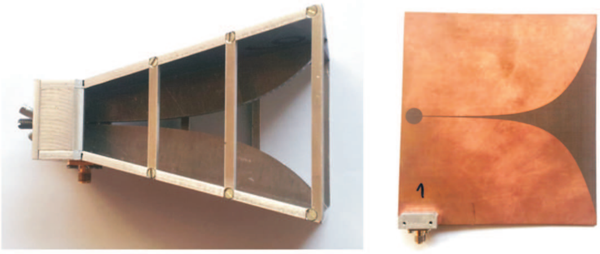

Figure 6.5: Measured antennas DRH20 and Vivaldi *V1*.

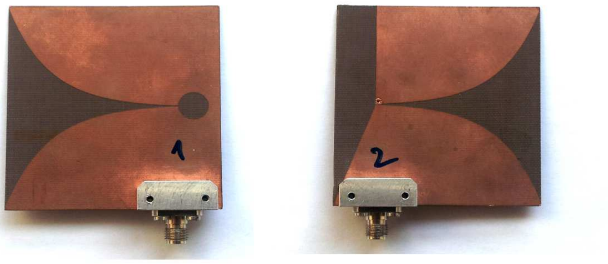

Figure 6.6: Measured antennas Vivaldi *v1* and *v2*.

The DRH antennas are chosen according to their wide operating frequency bandwidths. In principle, they show similar impedance and radiation characteristics to those of Vivaldi antennas, which are widely used in ultra-wideband (UWB) systems. The measurements are undertaken simultaneously in indoor conditions in both TD and FD using Agilent scope DCAJ86100C and VNA40. Time domain data are obtained at 4096 points with the sampling rate equal to 163.84 GHz, whereas frequency domain data are collected within the frequency range from 1 GHz to 26 GHz at 3201 frequency points. The closer description of particular systems was previously described. Transmitting and receiving antennas are attached to the 1.5 m high tripods with a separation of 3 m. In comparison to the frequency domain measurement, where the transmitting and receiving antennas are connected directly to VNA via coaxial cables, the nonlinear amplifier is connected between the Agilent scope and transmitting antenna in TD measurement arrangement. The amplifier then generates excitation impulses demonstrated in Fig. 6.3. For the in-depth comparison of results, all gathered data are processed in the same frequency bandwidth.

All measurements are summarized in Tab. 6.1. Each combination of three, two or one transmitting and receiving antenna(s) is measured. Three antennas method can be apparently performed in order to calculate the impulse response for all presented antennas by combining the measured transfer functions. The obtained results are used as a reference for the reference antenna method.

Table 6.1: Antenna measurement set-ups.

Meas. No.	Transmitting - receiving antenna		
1	DRH1 - DRH2	DRH2 - DRH3	DRH3 - DRH1
2	*v1* - *v2*	*v2* - *v3*	*v3* - *v1*
3	DRH1 - *V1*	DRH1 - *V2*	-
4	DRH2 - *V1*	DRH2 - *V2*	-
5	DRH3 - *V1*	DRH3 - *V2*	-
6	*V1* - *V2*	-	-

The comparison of normalized DRH20-1 antenna impulse responses calculated from the time and frequency domain data are indicated in Fig. 6.7 and Fig. 6.8. The used DRH antennas are assumed to be identical. This assumption is underpinned by the existence of very similar measured responses (Fig. 6.9). Therefore, further comparisons are going to be based uniquely on results related to one DRH antenna. In addition, Fig. 6.10 shows a good agreement of the DRH impulse responses calculated from both, time and frequency domain data.

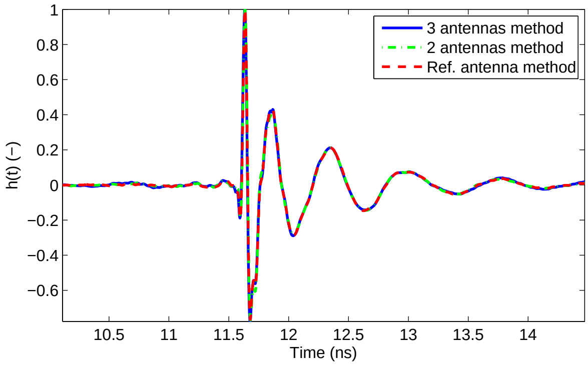

Figure 6.7: Impulse responses of DRH20 measured in TD.

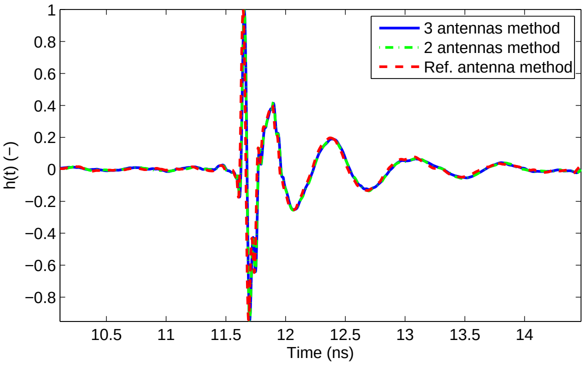

Figure 6.8: Impulse responses of three DRH20 antennas measured in FD.

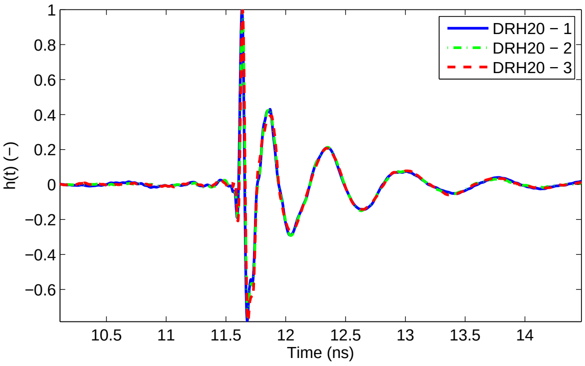

Figure 6.9: Comparison of DRH20 antennas measured in TD.

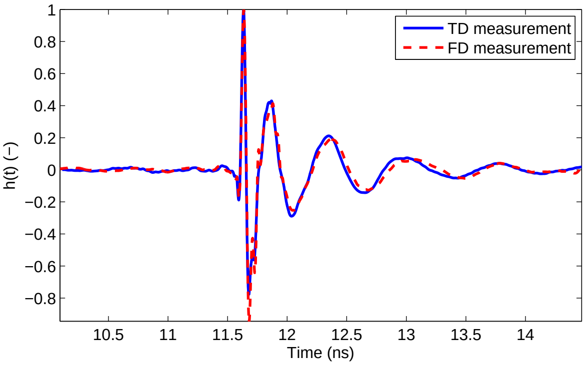

Figure 6.10: Comparison of DRH20 antennas measured in TD and FD.

Fig. 6.7 and 6.8 show a very good correspondence of acquired impulse responses of different methods. Reference antenna measurements are carried out according to the aforementioned one transmission measurement. Moreover, in comparison to the commonly used reference antenna method (Eq. (6.12)), the difference in results obtained from the proposed method (Eq. (6.13)) equals barely 0.07 %, see Fig. 6.11. In case of the rest of antennas, the difference fluctuates between 0.05 % and 0.09 %.

Three antennas method is employed for three transmission measurements of DRH20-3, *V1* and *V2*. The impulse responses of Vivaldi antennas are subsequently calculated. The agreement of this method with two antennas method and reference

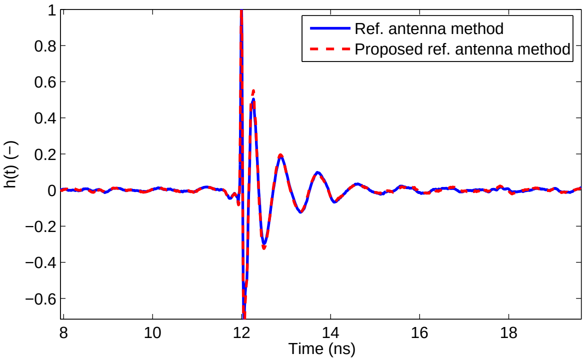

Figure 6.11: Comparison of commonly used reference antenna method (Eq. (6.12)) and proposed method for DRH20 antenna (Eq. (6.13)).

antenna method is shown in Fig. 6.12. The reference antenna method produces results that are slightly different from results of both previous methods.

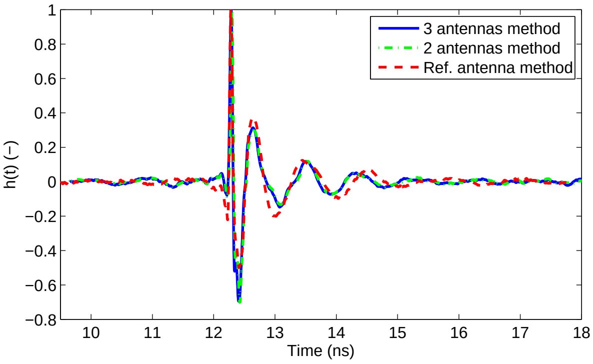

Figure 6.12: Impulse response of *V1* Vivaldi antenna obtained from TD data.

The impulse responses of small Vivaldi antennas *v1* and *v2* (*v3* are nearly identical to *v2*) are presented in Fig. 6.13 and 6.14.

Due to weighting of *v1* and *v2* responses, the different feeding of the first antenna leads to the incorrect calculation of its impulse response (in case that the two antennas method is applied), see Fig. 6.13. This phenomenon is obvious from the negative peak of response, which is suppressed.

The comparison of results shows a very good agreement of impulse responses computed by the aforementioned three basic methods from both time and frequency data.

The three antennas method ensures a high accuracy of results by measuring three pairs of three unknown antennas. Furthermore, all three impulse responses for these antennas can be calculated. The two identical antennas method also shows similar results, although the calculated impulse responses can differ from real ones in case of non-identical or only similar antennas. This is demonstrated in case of *v1* and *v2* Vivaldi antennas, where the first antenna comprises a classical radial stub to circular stub transition, while the other antenna (or even *v3*) involves a via to the slot-line transition. Yet the reference antenna method offers worse results, which is attributable to the fact that the presented impulse characteristics do not comprise

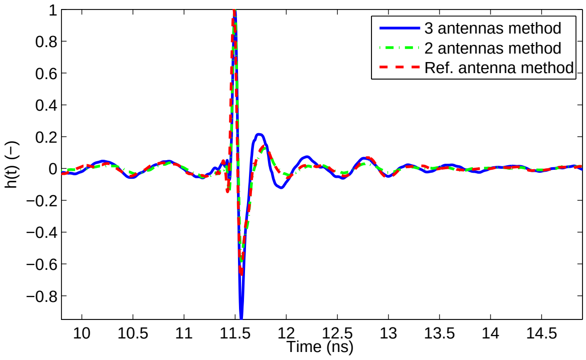

Figure 6.13: Impulse response of *v1* Vivaldi antenna obtained from TD data.

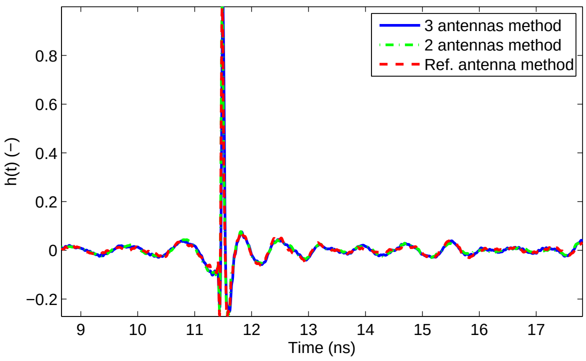

Figure 6.14: Impulse response of *v2* Vivaldi antenna obtained from TD data.

the excitation signal. Thus these responses depend substantially on the antennas frequency operating bandwidth. In case of two and three antennas methods, similar types of antennas are used, while in case of the reference antenna method, more heterogeneous types of antennas are employed.

6.2 Antenna Pattern Correction in NF-FF Transformation

Antenna compensation process (or antenna pattern correction) is typically performed involving first order algorithms, [97], [98], that assume limited spherical harmonics of the antenna radiation pattern. It follows, that only few (i.e. 1, 2 or 3) harmonics are utilized in order to compensate the antenna effect. However, this assumption has limited accuracy in case of broadband structures and full compensation need to be performed. The antenna compensation technique, used in this thesis, follows method derived in [99].

In this case antenna radiation pattern can be represented by superposition of cylindrical functions. Its relation to backscattered field is based upon Graf's addition theorem, (Eq. 2.35), which in cylindrical coordinate system states that a displaced cylindrical harmonic function can be constructed from a linear superposition of undisplaced cylindrical harmonic functions. Following [97] and CNFFFT technique, antenna pattern correction has form of Eq. (6.15).

$$S^{FF}(\phi, k) = \frac{1}{4}\sqrt{\frac{R_0}{j\pi k}} \sum_{n=-N}^{N} \frac{(-\mathrm{j})^n}{A_n(2kR_0)} U_r^{NF}(n,k)\, \mathrm{e}^{\mathrm{j}n\phi} \tag{6.15}$$

Convolution expansion kernel incorporates sum of weighted cylindrical harmonics $A_n(2kR_0)$, see Eq. (6.16).

$$A_n(2kR_0) = \sum_{m=-M}^{M} j^m a_m(k) H_{n+m}^{(1)}(2kR_0) \tag{6.16}$$

Here, each coefficient of kernel harmonic A_n is represented as a sum of Hankel funcions $H_{n+m}^{(1)}$ weighted by azimuthal harmonics of antenna radiation pattern $a_m(k)$. Number of pattern harmonics is limited by M, that is chosen as stated previously in this subsection. By omitting the antenna pattern correction, $m = 0$ and Eq. (6.16) transforms to form of Eq. (2.43).

In this case, measurement of antenna DRH20 is undertaken according to measurement scheme described in subsection 4.2.4) - RCS Normalization. Impulse or frequency responses are subsequently calculated following two identical antennas method (see Eq. 6.11). Coefficients $a_m(k)$ can be then acquired by taking 1D FFT of antenna frequency response or 2D FFT of its impulse response.

Measured and computed TD response (at mainlobe direction) and its envelope are depicted in Fig. 6.15. The envelope is obtained from analytical impulse response calculated by means of Hilbert transform. It actually localizes the energy distribution in time and it is hence a direct measure for the dispersion of an antenna. For high data rates transfer and high-resolution imaging purposes the width of envelope (expressed for its half power level) should not exceed hundreds of ps. Fig. 6.16 then shows change of the calculated envelope with azimuth. It follows, that most of energy is radiated within approximately ±38° azimuthal span. Radiated impulses are dispersed in other directions. This information is, beside radiation pattern, particularly useful in radar imaging.

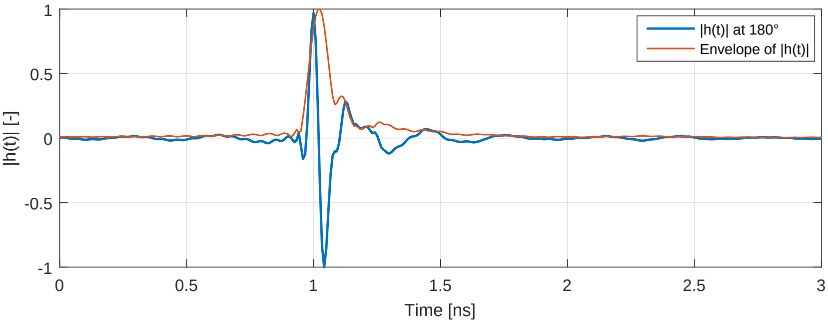

Figure 6.15: Impulse response of DRH20 and its envelope.

Additional oscillations of impulse response denote so called ringing caused by resonances due to energy storage and/or multiple reflections within antenna. Oscillation of radiated/received impulse then occur as consequence. Long duration of

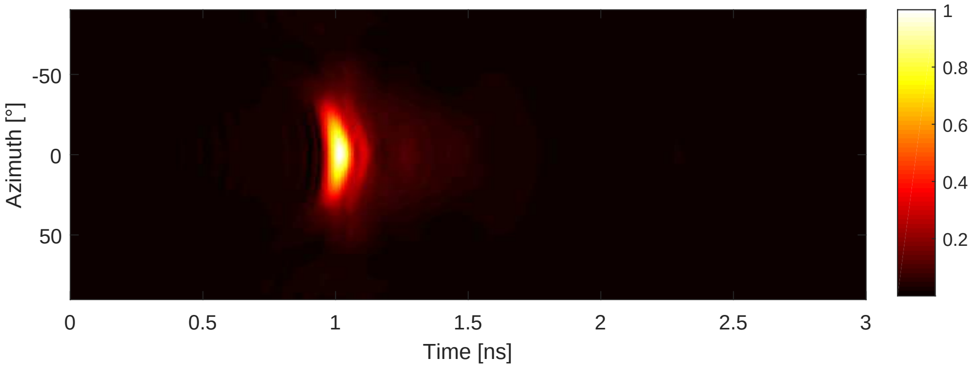

Figure 6.16: Azimuthal dependency of transient impulse response envelope of DRH20.

ringing can interfere with target reflections in case of very short distance between target and antenna (i.e. up to 1 m).

Based on the calculated responses other TD and FD antenna characteristics can be easily computed (antenna factor, radiation pattern, gain, etc.). Following fig. 6.17 depicts measured normalized radiation patterns at frequencies 5, 10 and 15 GHz with corresponding half power beamwidth (HPBW). It can be calculated, that targets measured at distance 1.5 m are still illuminated by main beam (approx. ±20°), nevertheless with significant taper.

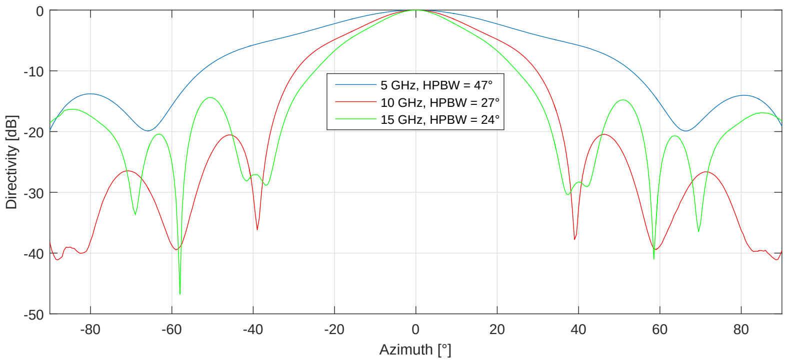

Figure 6.17: Measured radiation patterns of antenna DRH 20.

Angular harmonics of the antenna are then stated in Fig. 6.18. Number of significant harmonics grows with increasing frequency as expected. Following Fourier theory, azimuthal spectrum broaden as beamwidth narrows and vice versa.

Number of harmonics a_m used for RCS correction actually approximates antenna radiation pattern, see Fig. 6.19.

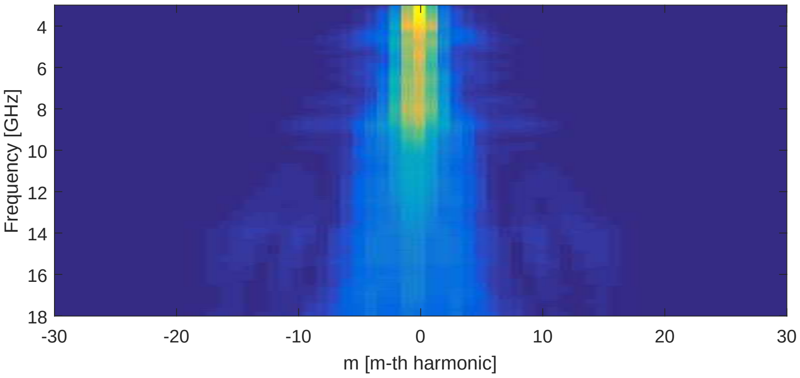

Figure 6.18: Azimuthal harmonics of radiation patterns of DRH20.

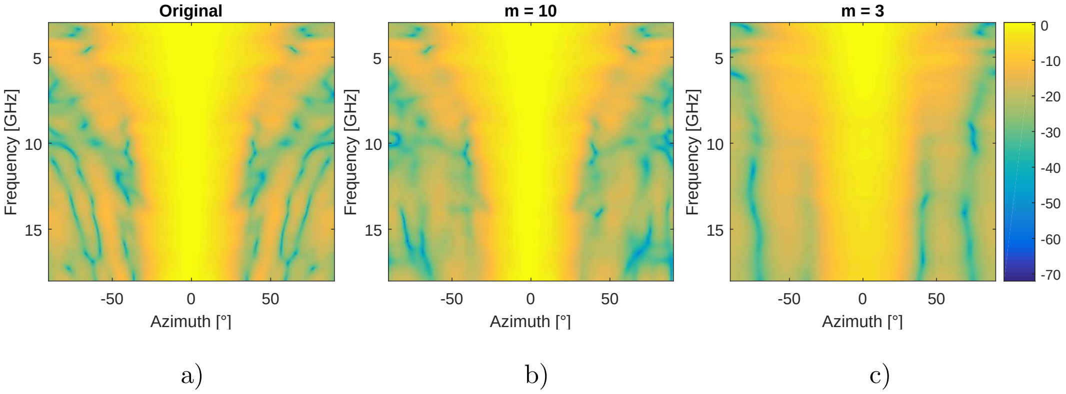

Figure 6.19: a) Original radiaton patterns compared to reconstructed patterns from: b) 10 harmonics and c) 3 harmonics.

Original radiation patterns are compared to those reconstructed from 3 and 10 fundamental harmonics. As 3-harmonics reconstruction narrows mainbeam at low frequencies and suppresses sidelobes, radiation patterns reconstructed from 10 harmonics show 95% fidelity with reference ones in azimuthal range ±40°. Thus, $m = 10$ harmonics is therefore used for antenna pattern (abbreviated as AP) compensation.

AP Corrected RCS of 870x40x40 mm Prism

Applicability of AP compensation method is demonstrated on NF-FF reconstruction of 870 mm long prism, see Fig. 6.20, where AP corrected RCS of the prism (blue line) is compared to uncompensated NF-FF RCS and RCS modeled in FEKO software (green and red line respectively).

Compared to AP uncompensated case, corrected pattern shows overall better correspondence with modeled RCS across frequency bandwidth. At 5 GHz, position and amplitude levels of sidelobes are restored. However, remaining alternating sidelobe levels cannot be compensated due to interference phenomenon (it will be obvious from restored images of the target stated later in this thesis). Improvement of sidelobe levels is observable at higher frequencies, see Fig. 6.21 and Fig. 6.22. In these cases, trend of patterns is particularly restored, nevertheless, errors described

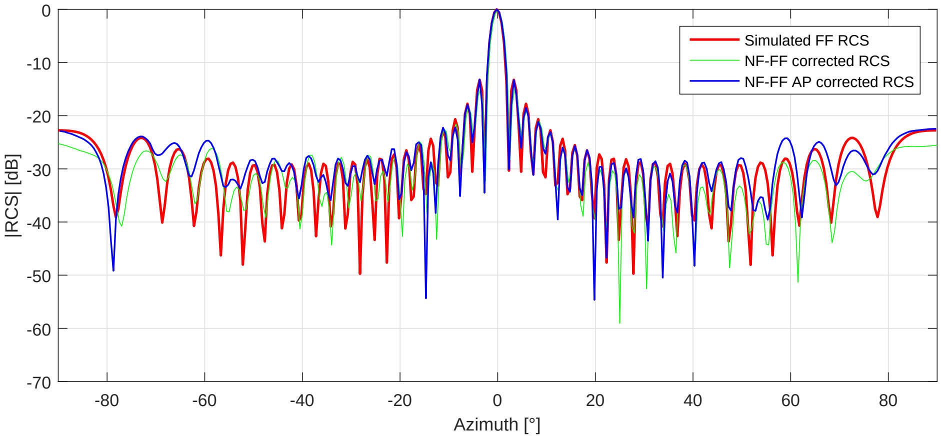

Figure 6.20: RCS of the 870x40x40 mm prism reconstructed from NF data at f = 5 GHz utilizing AP correction - comparison with FEKO simulation.

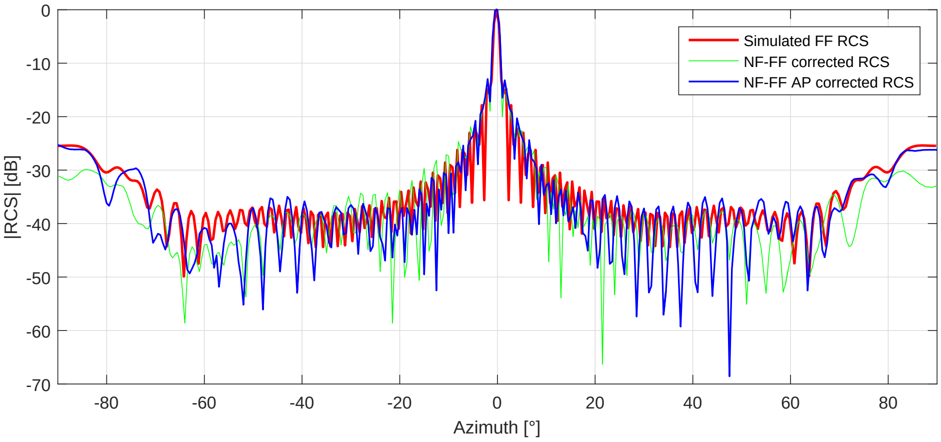

Figure 6.21: RCS of the 870x40x40 mm bar reconstructed from NF data at f = 10 GHz utilizing AP correction - comparison with FEKO simulation.

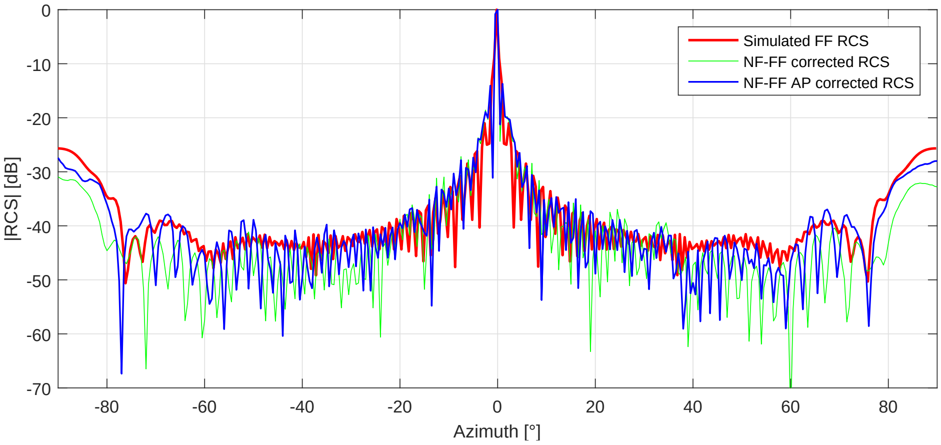

Figure 6.22: RCS of the 870x40x40 mm bar reconstructed from NF data at f = 15 GHz utilizing AP correction - comparison with FEKO simulation.

above rise with sensitivity of phase measurement at higher frequencies. In addition, low azimuthal sampling leads to uncertainties in sidelobe levels determination.

AP Corrected RCS of Antitank Missile PG-7M

CNFFFT technique is based on scattering model of the target. It assumes that target consists of individual scattering points without mutual interaction. In other words multiple reflections are treated as single one that leads to incorrect alignment of individual scattering points in image processing and also errors in RCS evaluation. Therefore antitank missile PG-7M is used in this thesis as a complex target containing multiple scattering parts. Test range with the target is depicted in Fig. 6.23. In the next Fig. 6.24, there is accurate model of PG-7M created in CST Microwave Studio.

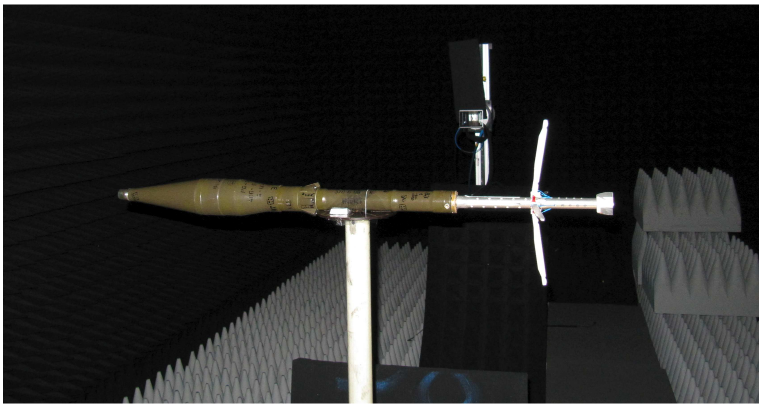

Figure 6.23: Measurement of PG-7M in anechoic chamber.

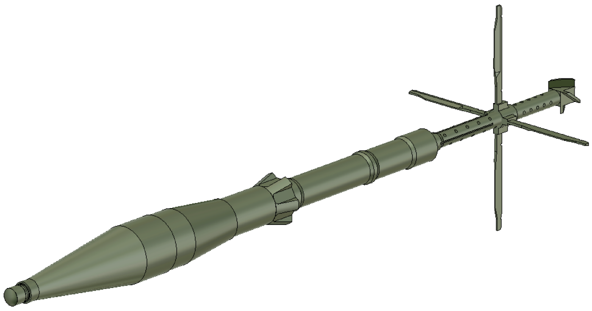

Figure 6.24: CST model of PG-7M.

The target is measured in the same configuration as in the case of long prism. However, additional absorbers located near the target are removed in order to eliminate mutual interactions.

Basic dimensions of PG-7M and its FF ranges are tabulated in Tab. 6.2. First dimension stands for length whereas second represents diameter of warhead.

Results presented in following figures Fig. 6.25 - Fig. 6.27 show reconstructed RCS of missile with AP corrected at frequencies 5, 10 and 15 GHz.

In the first one, measured NF RCS (light green line) and AP corrected NF-FF RCS (blue line) are compared to numerical RCS computed from CST model

Table 6.2: Dimensions of RPG and distances min. R_{FF} and R_0.

Dim.(mm)	Dim. (xλ_{max}, xλ_{min})	R_{FF} (m)	R_0 (m)	R_0(xR_{FF})
960 x 70	9.6 x 0.7, 57.0 x 0.7	18.43 - 110.59	1.5	0.081 - 0.014

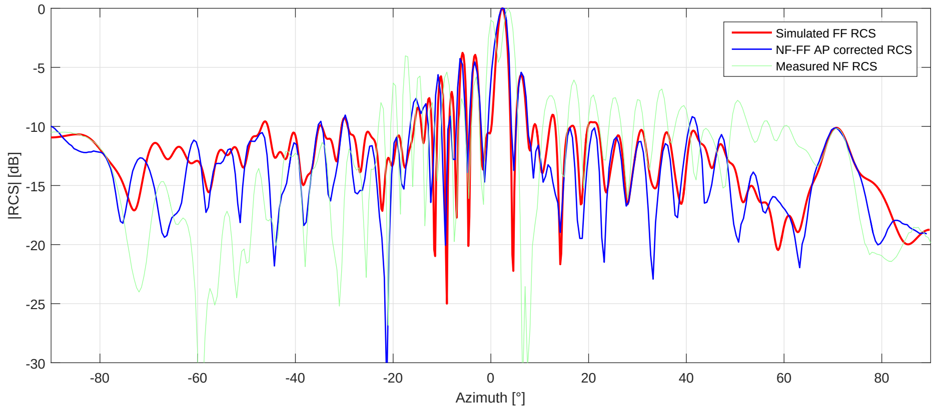

Figure 6.25: RCS of the PG-7M reconstructed from NF data at f = 5 GHz - comparison with CST simulation.

(red line). Measured NF traces will not be plotted in further figures due to clarity reasons. Values to $-90°$ position represent RCS computed form side to a tip positions of warhead whereas $+90°$ angle denotes RCS from stabilization propellers of the missile.

Reconstructed FF RCS of the target, even measured in its reactive-radiative field, corresponds in general with simulated values in this case. Multiple reflections, arisen from particular target components, create alternating and uneven sidelobes in resulting RCS pattern. It occurs mainly in azimuthal range $(-90, 0)°$. It is more obvious in case of reconstructed RCS at 10 and 15 GHz. Incorrect RCS values of front part of the missile can be accounted to both measurement and processing uncertainties.

Comparing to previous case, RCS calculated at 10 GHz shows generally better correspondence of corrected and simulated FF patterns. However, RCS pattern within $(-50, -15°)$ cannot be successfully restored due to rising complex scattering mechanisms at shorter wavelength and unpredictable field variations in reactive near-field. This phenomena can be observed in greater measure at 15 GHz, see Fig. 6.27. Size of some target components is comparable to actual wavelength (2 cm in this case). This in turn creates scattered field that cannot be translated to FF RCS by employed CNFFFT method. Furthermore, maximum values of sidelobes cannot be clearly determined owing to insufficient azimuthal sampling 0.5°. It need to be mentioned that simulated results are sampled 0.2°.

Relative NF-FF corrected RCSs of PG-7M for whole frequency bandwidth is depicted in Fig. 6.28. Fig. 6.29 then represents maximum absolute of RCS - note, that its maximum varies in azimuth with frequency.

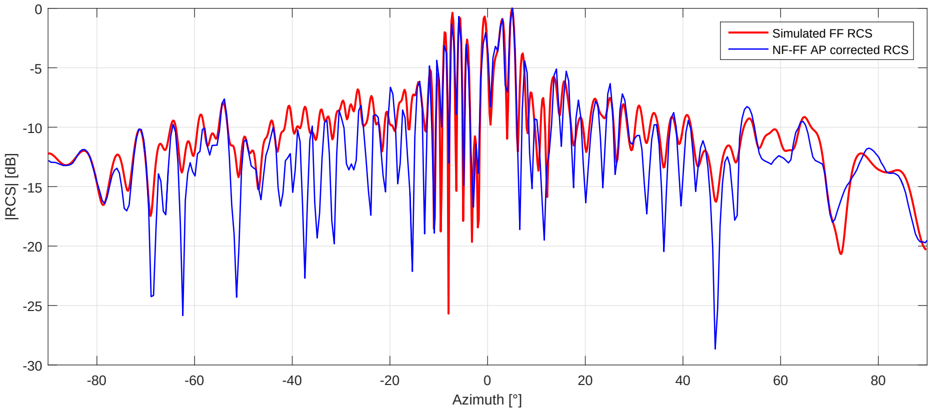

Figure 6.26: RCS of the PG-7M reconstructed from NF data at f = 10 GHz - comparison with CST simulation.

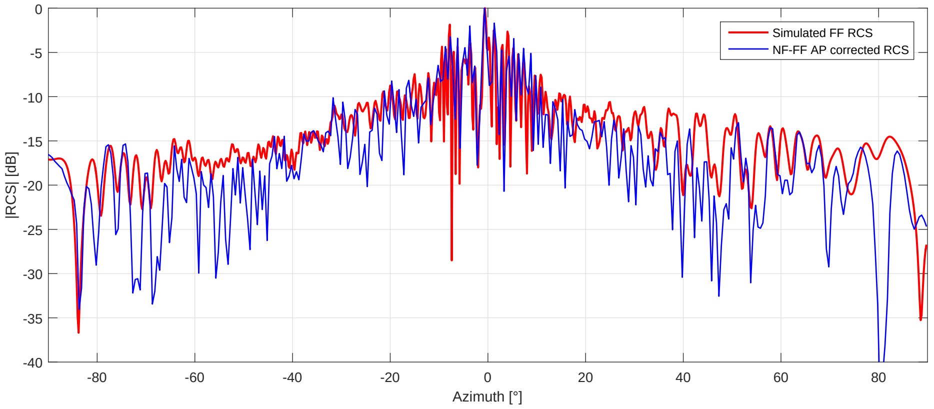

Figure 6.27: RCS of the PG-7M reconstructed from NF data at f = 15 GHz - comparison with CST simulation.

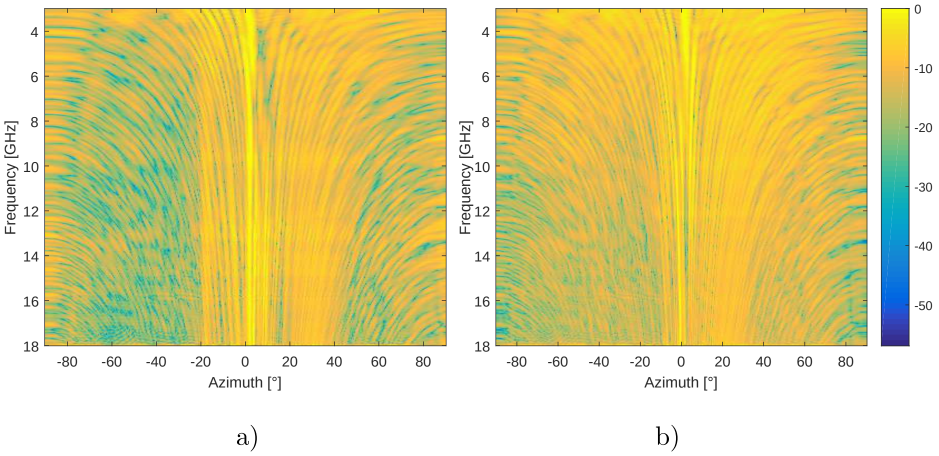

a)

b)

Figure 6.28: RCS of the PG-7M - comparison of: a) NF RCS data with b) NF-FF corrected RCS patterns.

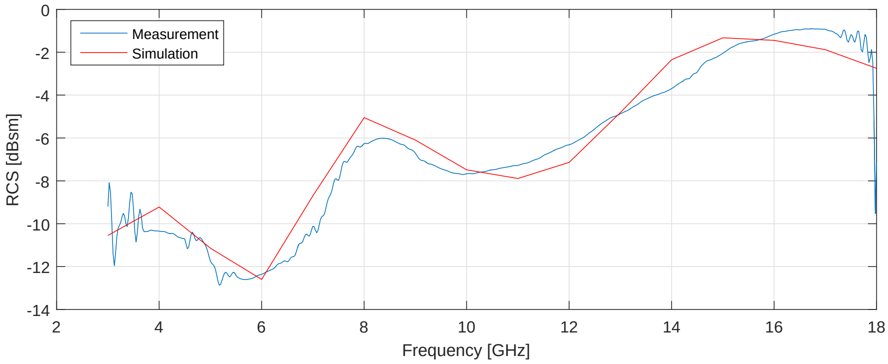

Figure 6.29: Absolute value of RCS of the PG-7M reconstructed from NF data - comparison with CST simulation.

6.3 Intermediate Results Summary

In this part of thesis, impact of broadband antenna radiation pattern on tapering of RCS patterns has been shown. In order to correct this influence, it is necessary to know a broadband radiation pattern of the antenna. Following this, measurement and calculation of impulse responses, based on TD and FD measurements, have been proposed in this thesis in order to obtain radiation patterns across wide frequency range. Validity of presented technique has been confirmed by comprehensive set of measurement employing different antenna structures. Furthermore, knowledge of obtained impulse responses are useful in short-range RCS (or SAR, ISAR) measurements since TD and FD antenna characteristics (as a signal dispersion, ringing, phase center, gain etc.) can be calculated from impulse responses. Based on obtained results, AP correction technique has been utilized in CNFFFT method. Since the applicability of this method has been poorly published and only shown on basic numerical models till now (thus under ideal conditions), [99], [100], AP compensation has been shown on measurement of long prism, where the pattern truncation became obvious. Furthermore, applicability of overall proposed correction scheme has been verified by measuring antitank missile PG-7M acting as target with complex scattering mechanisms. In addition, all obtained results will be used further in ISAR imaging.

Chapter 7

Objects Shape Reconstruction by ISAR Imaging

Inverse synthetic aperture Radar (ISAR) is still a powerful signal processing technique providing a high-resolution 2D image of a target of interest. ISAR images are created by coherent processing of signals backscattered from target. It is based on the same concept as SAR method, although they differ in the way of received signal processing and creating a focused image of target. To form an image, ISAR employs rotation of target so radar collects sequence of signals reflected successively from different views of target. As in case of SAR, it can be operated at very short ranges to scan object (area) of interest. It brings errors due to NF effects (discussed formerly in this thesis) defocussing image of target. ISAR processing actually images their scattering points that are moved to incorrect positions owing to spherical wave propagation.

7.1 ISAR Imaging

Based on this fact, images of selected targets will be computed by ISAR processing from formerly obtained NF-FF AP corrected data. NF errors will be also demonstrated at uncorrected data.

According to section 2.6, ISAR image $I(x', y')$ can be obtained from NF-FF corrected data $S^{FF}(\phi, k_r)$ in following way, see Eq. (7.1).

$$I(x', y') = \int_{0}^{\pi} \int_{-\infty}^{\infty} S^{FF}(\phi, k_r)|k_r| \mathrm{e}^{\mathrm{j}2\pi k_r (x' \cos(\phi) + y' \sin(\phi))} \mathrm{d}k_r \mathrm{d}\phi \tag{7.1}$$

Coordinates (x', y') determine position of each pixel in the image. This integral actually represents filtered back-projection of $S^{FF}(\phi, k_r)$ data, that are referred to individual projections in terms of ISAR imaging. Every slice - corrected frequency response of target is multiplied by ramp filter $|k_r|$, that in fact represents vector of frequency (down-range wavenumber) data. This high-pass filter provides de-blurring of final image $I(x', y')$. Integral can be resolved by inverse Radon transform, that is, together with filtered back-projection technique, described in Appendix C.

ISAR processing is used for both, NF data and NF-FF corrected signals of formerly presented targets in order to investigate errors caused by NF measurements and verify imaging capability of CNFFFT technique. Since all used targets are symmetrical and therefore measured only in $(0 - 180°)$ azimuthal span, presented images are mirrored for remaining angles and symmetrical around x axis as well. Resolution in both directions is $1\,cm$. It is calculated from Eq. (2.6).

Firstly, ISAR image of short prism is computed from NF data and then from NF-FF corrected values, see Fig. 7.1 and Fig. 7.2.

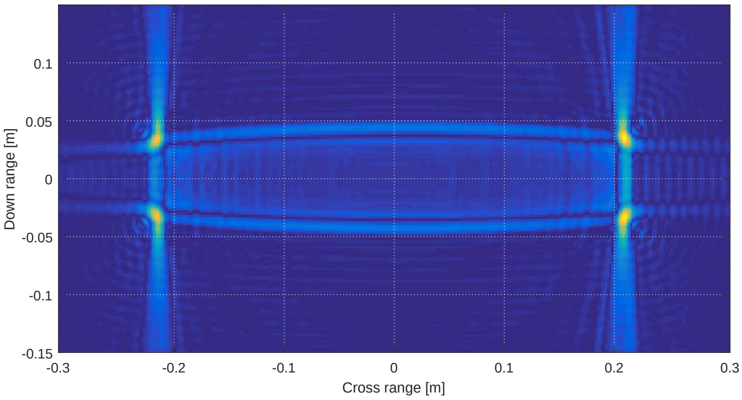

Figure 7.1: ISAR image of the 425x80x80 mm prism reconstructed from NF data.

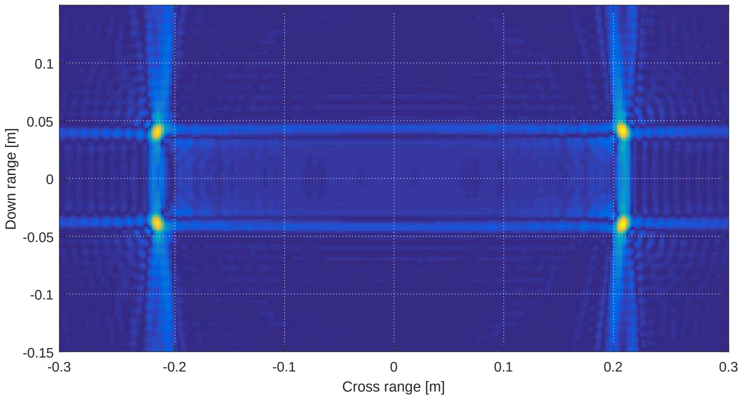

Figure 7.2: ISAR image of the 425x80x80 mm prism reconstructed from corrected NF-FF data.

Strongest spots are result of inverse Radon transform processing and represent edges of the prism. Their intensity reduces contrast of other parts of target. Other noticeable unwanted right-angled artifacts are consequence of very strong reflection from front and side part of the prism (when is turned parallel and perpendicularly to antenna). Shape of the uncorrected target show 8 mm displacement of prism corners in down-range direction due to NF effects. This phenomenon is reduced practically to zero (considering given resolution) after NF-FF data correction. Corners are also more localized.

In next step, images of long prism are calculated in the same manner as first case. Fig. 7.3 shows sinograms of unprocessed NF data compared to NF-FF corrected values. Sinogram is referred to arrangement of range profiles of reflectivity measurements (projections) for all azimuthal angles into matrix (Radon space). The term is derived from full 360 degree projections of the point scatterer located off-center that forms sine-like image of Radon space.

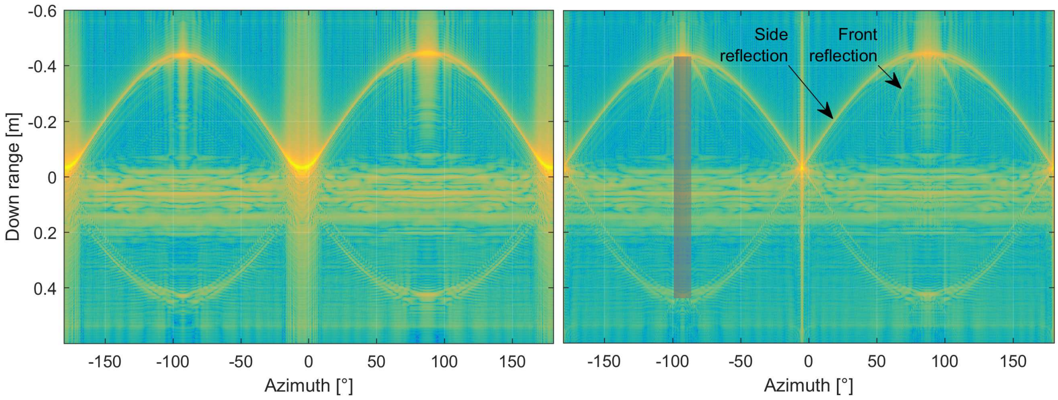

a) b)

Figure 7.3: Sinograms of the 870x40x40 mm prism - a) uncorrected and b) NF-FF corrected data.

Down range label is centered according to target rotation center. It is determined primarily from the knowledge of actual distance between antenna aperture and rotary support center. Exact target center is then corrected based on reflections from target oriented parallel and perpendicularly to antenna.

Sinogram of NF-FF corrected data shows localized reflections, mainly from perpendicular orientation of target (approx. 0°). Furthermore, reflections from front part of prism are restored for different azimuthal angles (observable at $\pm(60°-120°)$). In both cases, horizontal, almost unvarying reflections, represent interaction of target and near located objects, mainly rotary support, that could not be mathematically suppressed. On the other hand, vertical strong reflections are introduced by preprocessing steps. This error only increases overall noise floor in image domain and has negligible effect on resulting shape of target.

Effects of spherical wave are more noticeable in reconstructed images - Fig. 7.4 depicts uncorrected contours of long prism. Edges are translated in down range approximately 4.7 cm compared to actual positions. Taking into account width of prism 4 cm, reconstructed long sides are crossing and create spurious reflections in resulting image. Four distinct spots situated at approximate positions ±6.3 cm in cross range denote interactions of target and its support (round dielectric disc of 12 cm in diameter). Due to these mutual unwanted reflections, shape of this support is partially visible even though it has been canceled out from data by means of background subtraction.

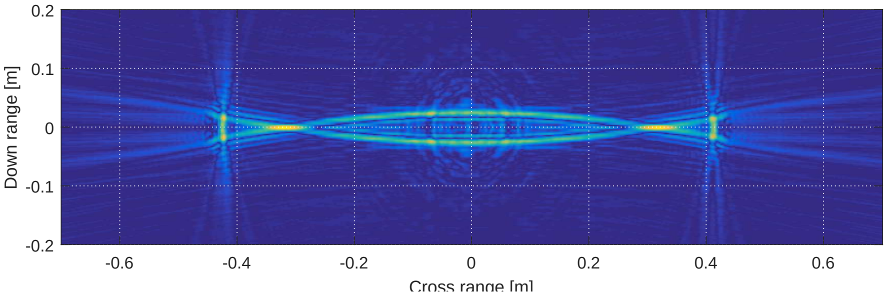

Figure 7.4: ISAR image of the 870x40x40 mm prism reconstructed from NF data.

Performance of employed correction process is demonstrated in Fig. 7.5, where the correct shape of prism is restored.

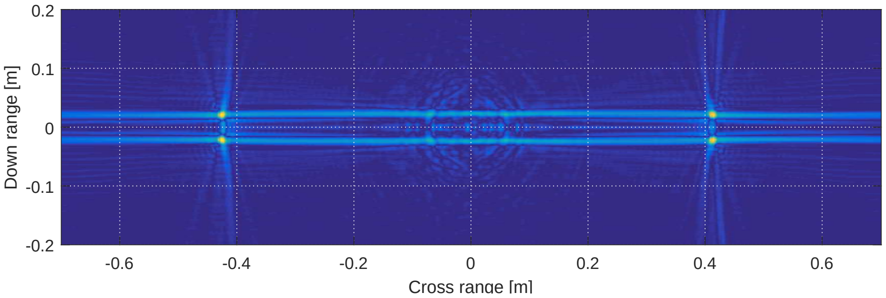

Figure 7.5: ISAR image of the 870x40x40 mm prism reconstructed from corrected NF-FF data.

Following results show image reconstruction of antitank PG-7M missile. Sinograms of uncorrected NF and NF-FF corrected data are depicted in Fig. 7.6 and Fig. 7.7) respectively.

Comparing these images, data are corrected in same manner as in case of long prism - NF errors are most noticeable at misaligned reflections from utmost parts of the target located at about ±25°. After NF-FF processing, not only positions of these reflections are corrected but also new reflections are observable. Silhouette of target is therefore superimposed to corrected sinogram (Fig. 7.7) in order to connect particular reflections with corresponding parts of target. It thus shows spatial distribution of these reflections related to target rotation from which contribution of individual parts to total scattered field can be determined. As expected, strongest scattering belong to parts where multiple or strong specular reflections occur - stabilization propeller part, motor jets (at around 0 m in downrange), cone-shaped warhead etc. In addition, stronger scattering from motor jets occurs due to their cavities when missile tail is pointing towards antenna $(-180°, 0°)$.

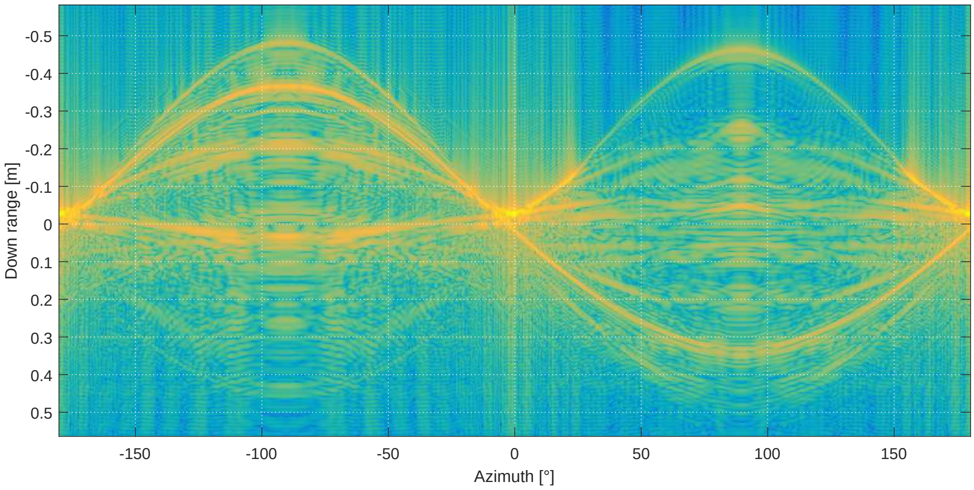

Figure 7.6: Sinogram of the PG-7M missile - uncorrected NF data.

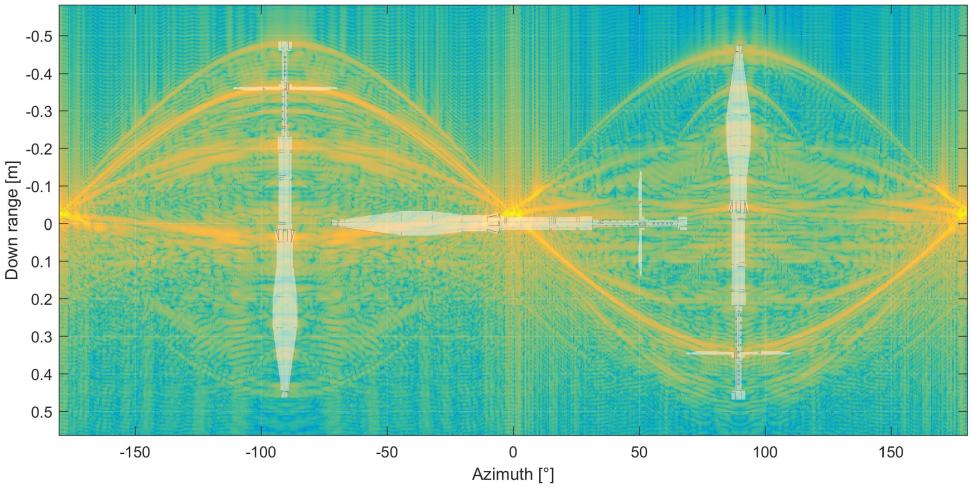

Figure 7.7: ISAR image of the PG-7M target reconstructed from corrected FF data.

ISAR image, corresponding to unprocessed sinogram, shows inaccurate determined target shape, mainly of its utmost parts, where NF error is highest, see Fig. 7.8. This effect actually dramatically shorten the target in image domain. Contrary to that, NF-FF processed image, stated in Fig. 7.9, shows considerable improvement of target shape, even though some parts are not retrieved correctly, i.e. front part of warhead and tail (after propellers) and also transition located at 0.2 m cross-range position. These errors are caused by incorrectly determined FF signals from NF data by means of CNFFFT algorithm, as stated in Fig. 6.25 - 6.27, depicting absolute value of RCS patterns. These can be also addressed to complicated scattering mechanisms.

In the last Fig. 7.10, silhouette of missile is superimposed into retrieved image (Fig. 7.9). Shape of reconstructed target corresponds with real object in general. Another clutter reflections located around the target are product of inverse Radon transform and are connected to those in sinogram.

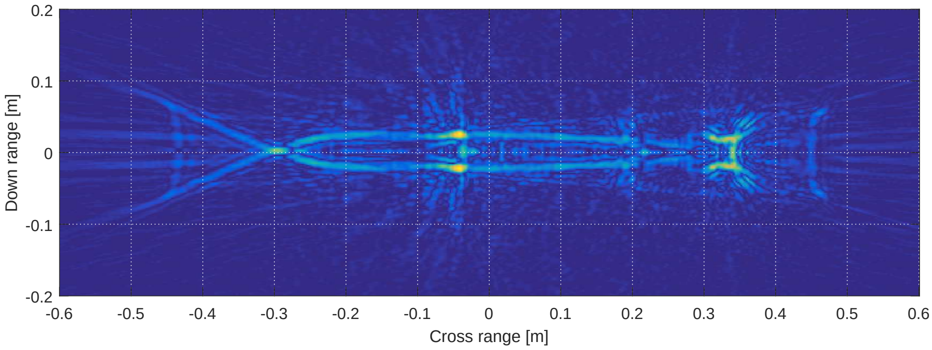

Figure 7.8: ISAR image of the PG-7M target reconstructed from uncorrected NF data.

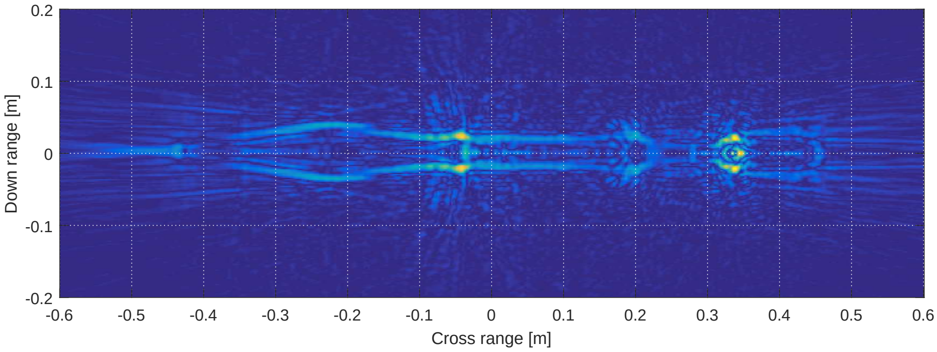

Figure 7.9: ISAR image of the PG-7M target reconstructed from corrected NF-FF data.

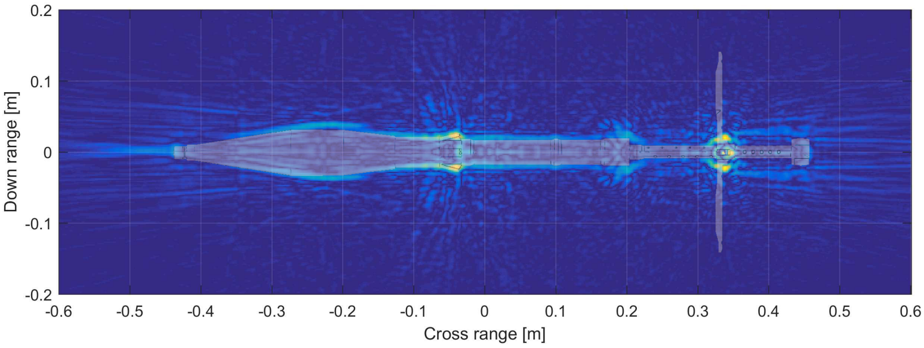

Figure 7.10: ISAR image ofthe PG-7M target reconstructed from corrected FF data.

7.2 Images Noise Reduction by Means of Principal Component Analysis

In the field of RCS measurement and analysis, large amount of data is often needed in order to obtain required correct characteristics. Data are typically collected for several target or measuring antennas configurations on one or more frequencies within defined azimuthal extent. Sampling in both, down-range (or frequency) and azimuth, depends on the required downrange resolution, unambiguous range and azimuthal resolution. Most of the targets have numerous scattering centers causing complex scattering mechanisms that result in many sidelobes in RCS pattern. Furthermore, by increasing frequency, the number of sidelobes grows thus they can be separated from each other by less than 1°, see Fig. 6.22 or Fig. 6.27 for instance.

To avoid a "smoothing" of the RCS pattern in this case, data need to be measured with azimuthal step even smaller than 0.1°. Such measurements are important for both, precise RCS determination for research purposes and also for further processing in statistical analysis (such as determining RCS average value, its standard deviation etc.) or radar imagery. In last mentioned case, very high-resolution (even sub-mm) images of target under test can be obtained using appropriate methods. However, resolving the shape of target, where lot of its scattering points are located, requires suppressing of the overall clutter reflections, that are present in each image. In case of ISAR imaging, reflections located far from target can be gated out from signals. Remaining clutter reflections near target or even interfering with it cannot be simply suppressed. These can reduce clarity of image and also lower contrast of target shape.

One of the often used technique in clutter reduction is smoothing, that is used to approximate the data set by means of some transformation convolution kernel. It results basically in reducing additive noise and also capturing the important pattern in the original data set. The most common transformation algorithm, among other (Kalman, Butherworth, low-pass filters etc.), is moving-average, that replaces each point by sliding unweighted mean of the n adjacent points. In the term of RCS the weighting window and angular slide step need to be chosen according to the variation of nulls and maximum of sidelobes and depending on objective criteria. Nevertheless, these techniques can suppress successfully only random clutter.

Except methods mentioned above, more sophisticated technique Principal component Analysis (PCA), based on statistical approach, is used here in order to reduce clutter (random as well as static errors) in ISAR images and also for dramatical reduction of dimensionality of resulting data sets. It is based on assumption, that each image (or data set) consists of patterns separable from each other. Usability of proposed technique has been proven earlier by eliminating backscattered field from obstacles (mainly wall) in though-wall imaging and even by ground removal in case of buried objects detection, see [78].

According to stated fact and theoretical background presented in section 2.7, selected targets, namely 425x80x80 mm prism and missile PG-7M, are subject of PCA. Here, ISAR images of targets are used rather then their sinograms since PCA-processed sinograms introduce significant errors (mainly shape distortion, absence of contours) in subsequent ISAR images.

ISAR image of target represents in terms of PCA data set $\mathbf{X}$, that can be transformed into new matrix $\mathbf{Y}$ through transformation matrix $\mathbf{S}$. Contrarily, original data set can be then obtained via PCA transform, see Eq. (7.2). Matrix $\mathbf{Y}$ actually states for mutually uncorrelated output data and $\mathbf{S}$ represents set of principal components (PC).

$$\tilde{\mathbf{X}} = \mathbf{S}_n^T \mathbf{Y}_n \tag{7.2}$$

Here, new data set $\tilde{\mathbf{X}}$ can be restored from original one employing only n output data vectors according to n PCs. Maximum amount of components is selected, based on cumulative sum of their variances. In this case, first n most significant PCs, that account for $90\% - 95\%$ of total variance, are selected. This value is determined, regarding to formerly performed experiments, in order to maintain relevant data in image and to suppress unwanted clutter as well.

PCA of Short 425x80x80 mm Prism

As stated formerly in this section, PCA decomposition of short prism image is performed firstly to demonstrate principle of clutter and dimensionality reduction. Fig. 7.11 represents most significant PCs with percentage contribution of each PC to total variance. Here, number of PCs is limited to 35, even though maximum number corresponds to number of image columns. It can be observed, that data belonging to first component yield about 95% of total variance, see Fig. 7.12. Therefore, image restored only from first PC carries most of information of original image. This is outlined in Fig. 7.13, where images are restored utilizing first, second and third PC respectively.

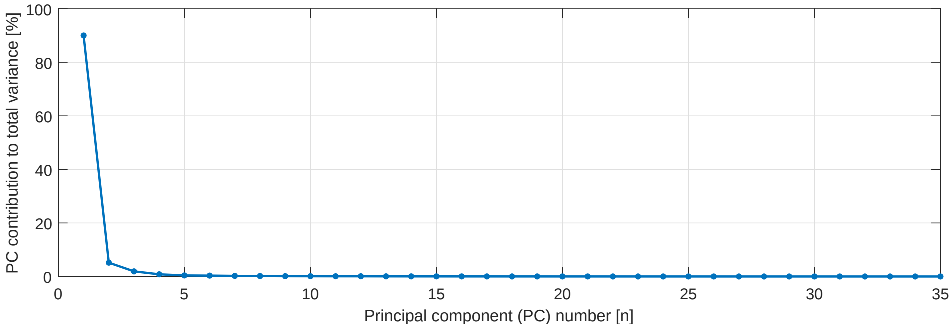

Figure 7.11: Contribution of principal components to total variance.

Owing to very strong reflection from side of the prism (perpendicularly oriented towards antenna), considerable artifacts arise outside of shape of prism during ISAR process (Radon transform) and therefore account for a first PC result.

Comparison of original image of prism and image restored from three aforementioned components is illustrated in Fig. 7.14. Employing PCA technique, evident artifacts are suppressed in case of restored image. The rest of unused PCs is therefore assumed to be a clutter part with no useful information for detection purposes. It is obvious, that unwanted artifacts or patterns, corresponding geometrically and in amplitude to reconstructed shape, cannot be simply eliminated by PCA method.

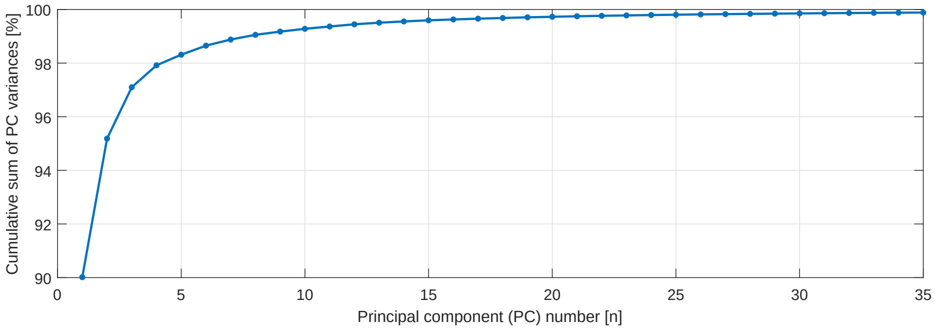

Figure 7.12: Cumulative sum of the partial variances of principal components.

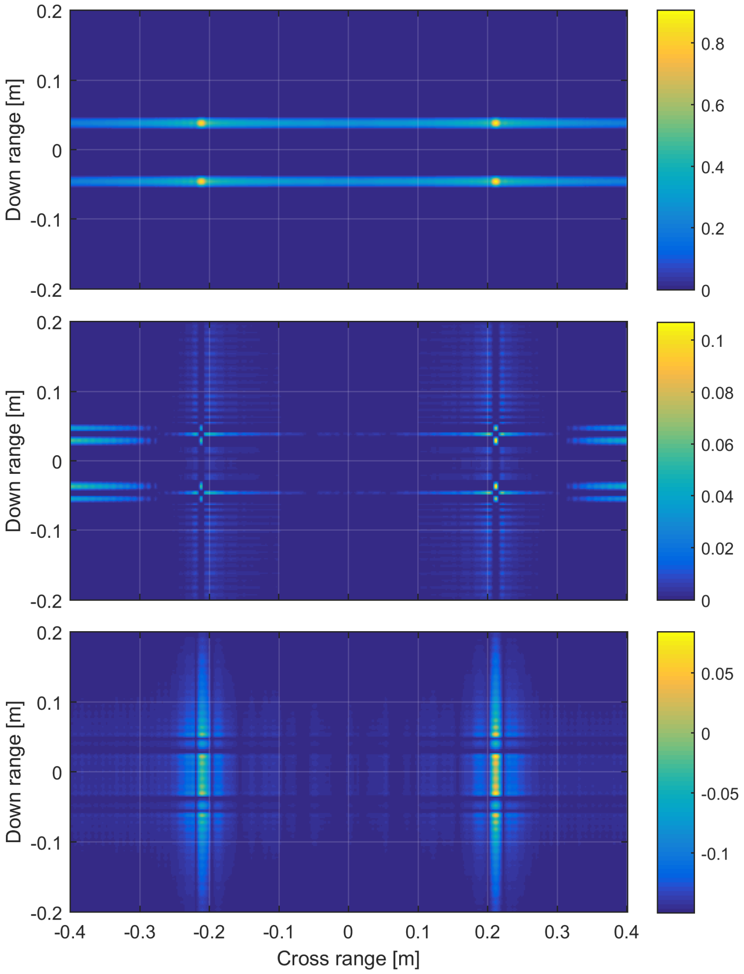

Figure 7.13: Prism 425x80x80 mm restored only from 1., 2. and 3. PC.

In this case, dimensionality of data used can be dramatically reduced. Suppose rectangular image of 800x800 pixels yielding 640000 data points in total. Using PCA, only 800x6 (4800) data points are needed for reconstruction (involving 3 PCs).

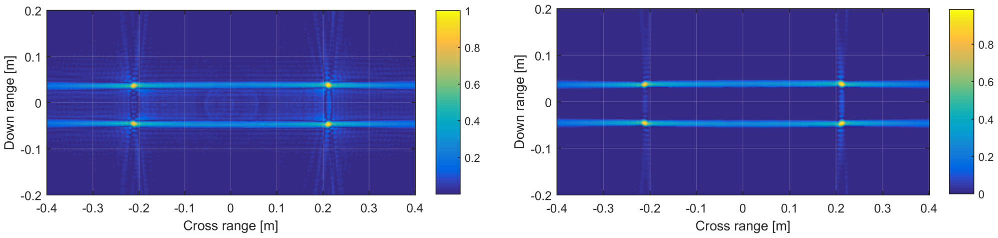

a) b)

Figure 7.14: Comparison of a) original and b) restored image only from first 3 PCs.

PCA of PG-7M Missile

ISAR, CT based imaging technique produces false reflections in image domain, mainly in case of targets whose scattered field is based on complex scattering mechanisms, see i.e. Fig. 7.17. Image of missile contains extensive amount of artifacts surrounding the target shape, that can be eliminated by means of PCA.

Calculated variances of PCs of missile image are depicted in Fig. 7.15. This trace does not evince observable break between variance contribution of particular PC. Therefore, more PCs are involved in target shape reconstruction. In order to obtain image retaining at least 90% of total variance, 15 or more PCs need to be used in reconstruction, see Fig. 7.16.

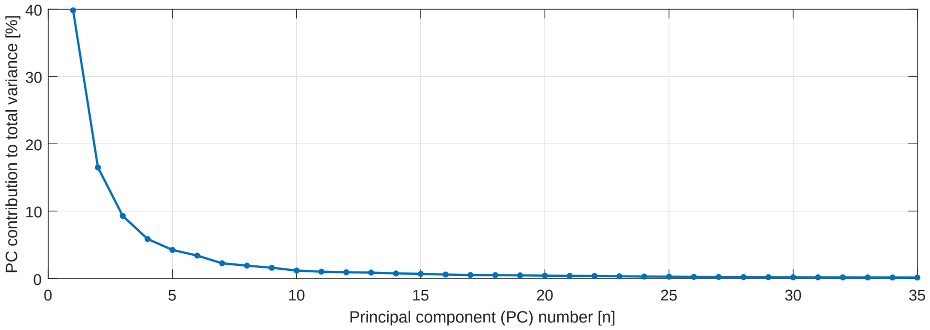

Figure 7.15: Contribution of principal components to total variance.

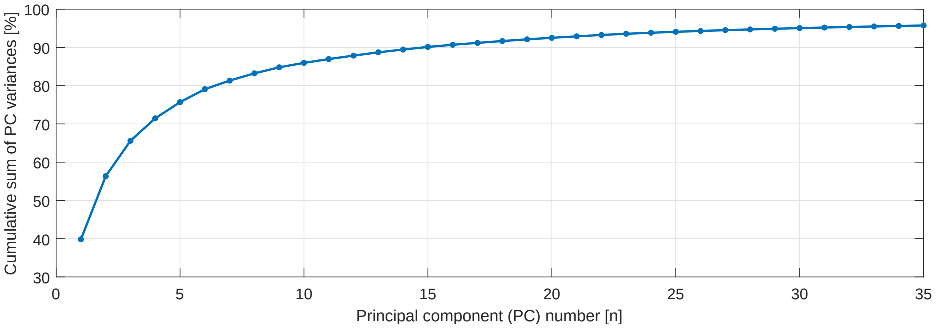

Figure 7.16: Cumulative sum of the partial variances of principal components.

Image of missile reconstructed form all PCs is stated in Fig. 7.17. Difference of such reconstructed image from original one is in order of $1^{-15}\%$. Contrarily, image of target involving only 15 PCs is depicted in Fig. 7.18. Most of minor artifacts is suppressed whereas important parts of target shape are retained. Difference of this reconstructed image with original one is less then 19%, where most significant error accounts for reflections from propeller part of missile, see Fig. 7.19. Comparison of restored images with corresponding PCA errors is stated in Appendix D. Furthermore, PCA of another target image - Malyutka anti-tank missile - is also presented, see Appendix D.2.

In addition, assuming the same number of image points as in previous case, only 24000 values are needed for image reconstruction using 15 PCs.

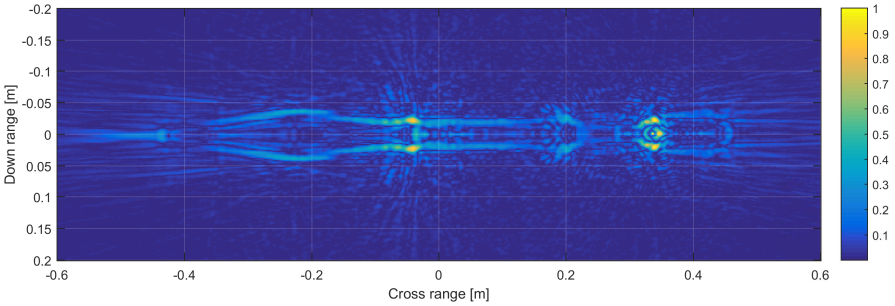

Figure 7.17: PG-7M restored from all PCs.

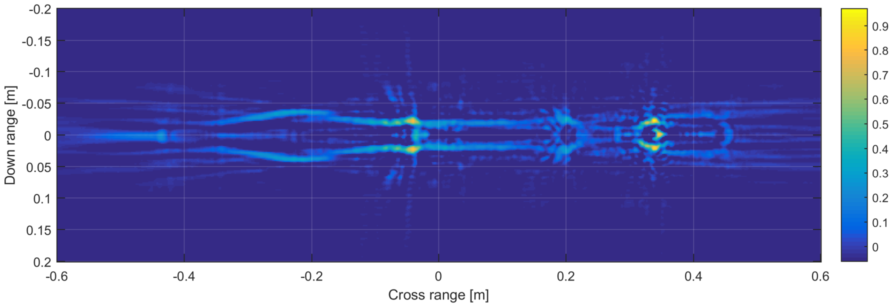

Figure 7.18: PG-7M restored only from first 15 PCs.

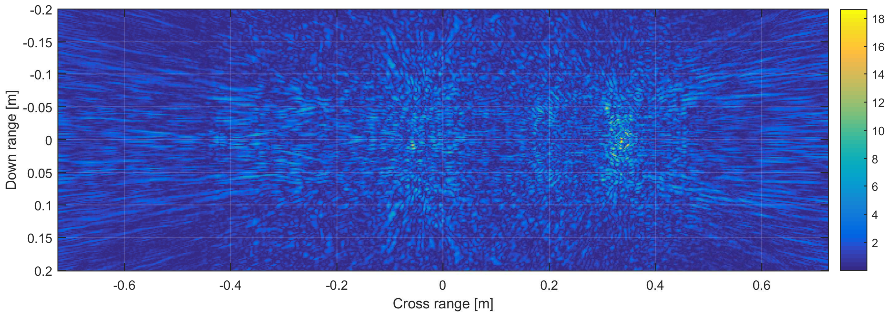

Figure 7.19: Difference between original image and restored one from 15 PCs (in %).

7.3 Intermediate Results Summary

In this chapter, proposed NF-FF correction scheme has been utilized in order to restore high-resolution ISAR images of selected targets since applicability of CNFFFT technique have not been presented yet for imaging purposes. Firstly, images of short and long metal prisms have been calculated by means of inverse Radon transform from uncorrected (NF) and NF-FF corrected data. It has been shown, that proposed technique is well-applicable even for targets measured at very short distances in terms of reactive and radiative field of targets. Next, image of PG-7M missile has been restored. Impact of errors related to measurements and processing have been discussed. Last mentioned can bring undesirable or false reflections to resulting images. Therefore, PCA technique has been utilized as a clutter suppression method. Its usability has been formerly described in [78].

Chapter 8

Conclusion

This thesis deals with objects characterization by means of wideband signals, that leads to determination of objects RCS and even shape based on their scattering properties. Knowledge of RCS parameters is important across industry and military applications worldwide. However, more available short-range sites, together with increasing test frequencies, lead to near field measurements of targets and subsequent far field RCS extrapolations of acquired data. Near-to-far field transformation techniques are still subject of interest and development since complete and optimal solution have not been found yet. Wideband measurements in near field imply another challenges in targets characterization.

Following above mentioned facts, main aim of this thesis can be divided into several consecutive parts. At first, it comprises far field RCS retrieval from broadband measurements undertaken in vicinity of the target. It focuses on one-plain circular near field measurements with subsequent image-based far field RCS approximation (CNFFFT), that has been validated utilizing mostly numerical simulations till now. Furthermore, non-ideal probing antenna introduces tapering and other errors into measured data and thus it is object of further correction. According to outlined correction process, next aim involves calculation of targets high-resolution images.

Results achieved and presented in this thesis can be summarized into following parts:

- **NF - FF RCS approximation from broadband measurements**
  Firstly, methodology of RCS pattern calculation from broadband measurements, undertaken in short-range full anechoic chamber, has been proposed as prerequisite for further processing of both, NF and FF data. More detailed analysis of basic correction techniques (namely time gating and background subtraction) has been presented, since their improper utilization can introduce several errors to resulting FF RCS patterns. Next, FF RCSs of test targets have been measured and calculated to verify proposed pre-processing scheme. It has been shown, that accurate absolute values of RCS can be evaluated without need of indirect measurement with known reference target.
  Following this, NF, mono-static, broadband measurements of electrically large targets (comprising metal prisms) have been undertaken at very short distance that ranges from $0.4R_{FF}$ to $0.017R_{FF}$ of their actual FF range (according to frequency) in order to calculate their FF RCS utilizing proposed NF-FF RCS

correction scheme. Acquired results then show very good correspondence with simulated patterns in CST and FEKO simulation software. Furthermore, they have revealed errors caused by interactions of target and background objects and also impact of radiation patterns of test antenna. Nevertheless, proposed scheme has been proven to be suitable technique used for determining FF RCS of electrically large objects ($4.25\lambda - 52.2\lambda$).

- **Correction of antenna pattern influence**
  In case of short-range measurements of electrically large objects, test antenna is located in their NF and introduces tapering errors in estimated FF RCS patterns. For purpose of this thesis, broadband antenna radiation patterns thus need to be known. Therefore, novel calculation of impulse responses, based on TD and FD measurements, have been proposed in order to obtain radiation patterns across wide frequency range. Validity of presented technique has been confirmed by comprehensive set of measurements employing different antenna structures. Knowledge of obtained impulse responses are also useful in short-range RCS (or SAR, ISAR) measurements since TD and FD antenna characteristics (as a signal dispersion, ringing, phase center, gain etc.) can be calculated from these responses. Acquired results have been then utilized in antenna pattern correction in CNFFFT scheme. Applicability of this method has been poorly published in papers and has been shown mostly on basic numerical models till now. Furthermore, in most cases the antenna effects are neglected.

  Therefore, antenna pattern compensation has been applied in this thesis to data acquired from measurement of long prism, where the pattern truncation became obvious. Improvement of sidelobe levels can be observed at selected frequencies so trend of these RCS patterns corresponds to simulated values. Nevertheless, multiple reflections from adjacent objects, short measurement range together with low azimuthal sampling lead to uncertainties in sidelobe positions and level determination, that cannot be suppressed by any of presented methods. In addition, applicability of overall proposed correction scheme has been verified by measuring antitank missile PG-7M acting as target with complex scattering mechanisms.

- **Objects shape reconstruction from FF-restored data, clutter and dimensionality reduction of obtained images**
  Effects of NF measurements have been demonstrated on calculated ISAR images. Phase differences of incident wave at target plane cause misalignment of scattering centers and even formation of false scattering centers of target in image domain. Practically, distortion of target contours can lead to its incorrect identification. Based on proposed overall NF-FF scheme presented in the thesis, above described distortion has been suppressed thus ISAR images of targets correspond to their real shape. In this case, images of short and long prisms, as well as PG-7M missile have been successfully reconstructed. In addition, image of another antitank missile has been computed. Measurements and subsequent data processing introduce errors in images in form of clut-

ter - artifacts arisen mostly from unfiltered reflections. Other then originate from imaging technique (inverse Radon transform) itself. These errors have been eliminated from respective images by means of PCA technique. Advantages and disadvantages of this approach have been also discussed. Besides, data needed for image reconstruction have been dramatically reduced utilizing PCA.

In conclusion, this thesis brings approach and solution to objects characterization in terms of their monostatic RCSs and TD responses applied to image reconstruction process, based on measurements in near radiative/reactive field of respective objects in full anechoic chamber. It shows applicability of proposed measurement and subsequent calculation scheme. Since it connects several correction techniques, whose properties have been formerly presented and tested incorporating only basic simulations in most cases, this thesis deals with measurements in real, non-ideal conditions. It reveals problems related to respective techniques that cannot be fully covered here. These facts, together with presented results, therefore create **new possibilities for further work**, such as:

- sensitivity analysis of particular parts of proposed scheme,
- analysis of accuracy of NF-FF technique according to different dimensions of measured targets,
- utilization of measurements for differently polarized test antenna and describing cross-polarization effects,
- antenna tapering effects would be investigated using different antenna structures,
- investigating of new clutter reduction techniques.

Bibliography

[1] Pavlovic, M., S., Tasic, M., S., Mrdakovic, B., L., Kolundzija, B., M.: *Monostatic RCS Analysis of Fighter Aircrafts*, 10th European Conference on Antennas and Propagation (EuCAP), Davos, 2016, pp. 1-4.

[2] Fan, X., et al.: *Research on the Bistatic RCS Characteristics of Stealth Aircraft*, Asia-Pacific Microwave Conference (APMC), Nanjing, 2015, pp. 1-3.

[3] Miacci, M., A., S., Martin, I., M., Rezende, M., C.: *Indoor and Outdoor Evaluation of Missile Prototype Scattering Diagrams*, SBMO/IEEE MTT-S International Conference on Microwave and Optoelectronics, Brasilia, 2005, pp. 566-569.

[4] Buller, W., Wilson, B., Ebling, J., van Nieuwstadt, L., Hart, B.: *Radar Measurements of NHTSA's Surrogate Vehicle "SS V."*, Report to Sponsored/Monitored by Garrick Forkenbrock, National Highway Traffic Safety Administration.

[5] Buller, W., Leblanc, D.: *Radar Characterization of Automobiles and Surrogate Test-Targets for Evaluating Automotive Pre-Collision Systems*, IEEE International Symposium on Antennas and Propagation and USNC/URSI National Radio Science Meeting, Chicago, IL, USA, 2012.

[6] Suzuki, H.: *Measurement Results of Radar Cross Section Of Automobiles For Milimeter Wave Band*, Proceedings of the 7th world congress on intelligent systems, Turin, Italy, 2000.

[7] Taylor, J., D.: *Introduction to Ultra-Wideband Radar Systems*, CRC Press, 1994, ISBN 9780849344404.

[8] Curlander, J., C., McDonough, R., N.: *Synthetic Aperture Radar: Systems and Signal Processing*, Wiley-Interscience:Series in Remote Sensing, New York, 1991.

[9] Massonnet, D., Souyris, J.-C.: *Imaging With Synthetic Aperture Radar*, EFPL Press, 2008.

[10] Kabourek, V., Cerny, P., Mazanek, M.: *Landmine Detection Using Ground Penetrating Radar and Polarimetric Synthetic Aperture Radar*,

Proceedings of the 5th European Conference on Antennas and Propagation (EUCAP), Rome, 2011, pp. 34-38.

[11] Martorella, M.: *Introduction to Inverse Synthetic Aperture Radar*, IEEE Radar Conference, Cincinnati, OH, 2014, pp. 28-28.

[12] Knott, E., F.: *The world's First Comparison of Outdoor RCS Test Ranges*, IEEE Antennas and Propagation Society International Symposium. 1999 Digest. Held in conjunction with: USNC/URSI National Radio Science Meeting (Cat. No.99CH37010), Orlando, FL, USA, 1999, pp. 1988-1991 vol. 3.

[13] Shields, M.: *The Compact RCS / Antenna Range at MIT Lincoln Laboratory*, 3rd European Conference on Antennas and Propagation, Berlin, 2009, pp. 939-943.

[14] Yamada. Y., Michishita, N., Nguyen, Q., D.: *Calculation and Measurement Methods for RCS of a Scale Model Airplane*, International Conference on Advanced Technologies for Communications (ATC 2014), Hanoi, 2014, pp. 69-72.

[15] Tusă, L., Nicolaescu, I., Moni, M., Banciu, M., G.: *Time-Frequency Domain Radar Cross Section Evaluation of an IAR 99 Scaled Model Aircraft*, 7th International Conference on Electronics, Computers and Artificial Intelligence (ECAI), Bucharest, 2015, pp. 1-4.

[16] Sefer, A., Uslu, M., A., Sevgi, L.: *MATLAB-Based 3-D MoM and FDTD Codes for the RCS Analysis of Realistic Objects [Testing Ourselves]*, IEEE Antennas and Propagation Magazine, Aug. 2015, vol. 57, no. 4, pp. 122-148.

[17] Spurgeon, W., A., Bossoli, R., B., Hirth, N., Ferreira, K.: *RCS Predictions From a Method of Moments and a Finite-Element Code for Several Targets*, Army Research Laboratory, July 2010.

[18] Yaghjian, A.: *An Overview of Near-field Antenna Measurements*, IEEE Transactions on Antennas and Propagation, Jan. 1986, vol. 34, no. 1, pp. 30-45.

[19] Mie, G.: *Beiträge zur Optik Trüber Medien, Speziell Kolloidaler Metallösungen*, Annalen der Physik, 1908, 330 (3): 377–445.

[20] Page, R., M.: *The Origin of Radar*, Doubleday, 1962.

[21] Skolnik, M., I.: *Radar handbook (2nd ed.)*, Mc Graw Hill, New York, 1990, USA, ISBN 0-07-057913-X.

[22] *RCS of Selected Targets*, [online]. Available at: http://www.globalsecurity.org/military/world/stealth-aircraft-rcs.htm. Cited 2016-01-17.

[23] Knott, E., F.: *Radar Cross Section, Second Edition*, corrected reprinting, Raleigh, N.C.: SciTech Pub., 2004.

[24] Balanis, C., A.: *Antenna Theory: Analysis and Design, 3rd Edition*, Wiley-Interscience, 2005, ISBN: 9780471667827.

[25] Collin, R., E.: *Antennas and Radiowave Propagation*, Mcgraw Hill Series in Electrical and Computer Engineering, 1985.

[26] Gregson, S., F., McCormick, J., Parini, C., Van Rensburg, D., J.: *Theory and Practice of Modern Antenna Range Measurements*, IET electromagnetic waves series 55, The Institution of Engineering and Technology, 2014, ISBN: 978-1-84919-563-8.

[27] Stimson, G., W.: *Introduction to Airborne Radar*, 2nd edition, SciTech Pub., 1998, ISBN: 9781891121012.

[28] *List of Radars*, [online] Available at:
https://en.wikipedia.org/wiki/List_of_radars. Cited 2017-01-12.

[29] Bezousek, P., Schejbal, V.: *Bistatic and Multistatic Radar Systems*, Radioengineering, Vol. 17, No. 3, September 2008.

[30] Cherniakov, M. (ed): *Bistatic Radar: Principles and Practice*, Wiley, 2007, ISBN 0-470-02630-8.

[31] Glaser, J., I.: *Bistatic RCS of Complex Objects Near Forward Scatter*, IEEE Transactions on Aerospace and Electronic Systems, Jan. 1985, vol. AES-21, no. 1, pp. 70-78.

[32] Bezousek, P., Schejbal, V.: *Radar technology in the Czech Republic*, IEEE Aerospace and Electronic Systems Magazine, 2004, Vol. 19, No. 8, p. 27-34.

[33] Boerner, M. -W., Brand, H., et.al.: *Direct and Inverse Methods in Radar Polarimetry, Part 1*, Springer Netherlands, 1992, ISBN: 978-94-010-9245-6.

[34] Schone, G., Riegger, S., Heidrich, E.: *Wideband polarimetric radar cross section measurement*, 1988 IEEE AP-S. International Symposium, Antennas and Propagation, Syracuse, NY, USA, 1988, pp. 537-540, vol.2.

[35] Norland, R., Gundersen, R., Skjonhaug, S., Skottene, A., Sveli, C., Dyroy, B.: *Polarimetric frequency agile FMCW RCS measurement radar*, 2007 IET International Conference on Radar Systems, Edinburgh, UK, 2007, pp. 1-4.

[36] Ai, X., Zhao, F., Liu, J., Yang, J., Gu, Z.: *Full-Polarization Bistatic Scattering Characteristics Analysis of Stealth Aircraft*, 2016 Progress in Electromagnetic Research Symposium (PIERS), Shanghai, 2016, pp. 2059-2059.

[37] Gau, J., R., J., Burnside, W., D.: *New Polarimetric Calibration Technique Using a Single Calibration Dihedral*, IEEE Proceedings - Microwaves, Antennas and Propagation, Feb. 1995, vol. 142, no. 1, pp. 19-25.

[38] Xu, X., Sun, S.: *A Background Extraction Technique for Polarimetric RCS Measurement*, 2013 International Conference on Radar, Adelaide, SA, 2013, pp. 394-397.

[39] Jankiraman, M.: *Design of Multi-Frequency CW Radars*, Scitech Publishing, Inc. 2007. ISBN: 1891121561.

[40] Stove, A.: *Linear FMCW Radar Techniques*, IEEE Proceedings For Radar and Signal Processing, 1992, vol. 139, no. 5, pp. 343–350.

[41] Cam, N., Joongsuk, P.: *Steped-Frequency Radar Sensors*, Springer, 2016. ISBN: 9783319122717.

[42] Weiss, J., M.: *Continuous-Wave Stepped-Frequency Radar for Target Ranging and Motion Detection*, Proceedings of MICS symposium, 2009.

[43] Amin, M., G.: *Through-the-Wall Radar Imaging*, CRC Press, Dec. 2010. ISBN: 9781439814765.

[44] Daniels, D., J.: *Ground Penetrating Radar, 2nd Edition*, The institution of Engineering and Technology, London, 2007, ISBN: 0863413609.

[45] Swandstrom, J., Puri, J., Kwan, B., Anderson, K.: *Antenna and RCS Measurement Configurations Using Agilent's New PNA Network Analyzers*, AMTA Proceedings, 2003, pp. 573-579.

[46] *Antenna Measurements, RCS Measurements and Measurements on Pulsed Signals with Vector Network Analyzers R&S ZVM, R&S ZVK.* Application Note, [online]. Available at: www.rohde-schwarz.com. Cited 2016-12-04.

[47] Ciattaglia, M., Marrocco, G.: *Approximate Calculation of Time-Domain Effective Height for Aperture Antennas*, IEEE Transactions on Antennas and Propagation, March 2005, vol. 53, no. 3, pp. 1054-1061.

[48] O'Connor, S.: *US Restricted and Classified Test Sites*, [online]. Available at: http://geimint.blogspot.cz/2007/08/us-restricted-and-classified-test-sites.html. Cited 2016-09-14.

[49] O'Connor, S.: *Foreign RCS Ranges*, [online]. Available at: http://geimint.blogspot.cz/2009/12/foreign-rcs-ranges.html. Cited 2016-09-14.

[50] Fordham, J., A., Baggett, M.: *RCS Measurements in a Compact Range*, Microwave Product News, p.1, August 2005.

[51] *Raytheon Test Facility*, [online]. Available at: http://www.raytheon.com/capabilities/products/atf/. Cited 2016-09-17.

[52] *NavAir test facility*, [online]. Available at: http://www.navair.navy.mil/ibst/index.html. Cited 2016-09-17.

[53] Birtcher, C., R., Balanis, C., A., Vokurka, V., J.: *RCS Measurements, Transformations, and Comparisons Under Cylindrical and Plane Wave Illumination*, Transactions on Antennas and Propagation, March 1994, Vol. 42, No. 3.

[54] Li, N.,-J., Chen, W., -J., et.al.: *Investigation on the RCS Measurement Techniques of Large Objects at Near Distance*, Progress In Electromagnetics Research Symposium, Hangzhou, China, 2008.

[55] Hansen, T., B., Marr, R., A., Lammers, U., H., W., Tanigawa, T., J., McGahan, R. V.: *Bistatic RCS Calculations From Cylindrical Near-Field Measurements—Part I: Theory*, IEEE Transactions on Antennas and Propagation, Dec. 2006, vol. 54, no. 12, pp. 3846-3856.

[56] Stratton, J., A.: *Electromagnetic Theory*, New York: McGraw-Gill, 1941.

[57] Bucci, O., M., Gennarelli, C., D'Agostino, F.: *A new and Efficient NF-FF Transformation With Spherical Spiral Scanning*, Proceedings of IEEE Antennas and Propagation Society International Symposium, Jul. 2001.

[58] D'Agostino, F., Ferrara, F., Gennarelli, C., Guerriero, R., Migliozzi, M.: *An Innovative Direct NF-FF Transformation Technique with Helicoidal Scanning*, International Journal of Antennas and Propagation, vol. 2012.

[59] LaHaie, I.,J., LeBaron, E.I.: *Discrete Implementation of an Image-Based Algorithm for Extrapolation of Radar Cross-Section (RCS) from Near-Field Measurements*, Proc. of the 17th Annual Meeting of the Antenna Measurement Techniques Association (AMTA 95), Williamsburg, VA, pp. 149-154.

[60] N. J. Li, C. F. Hu, L. X. Zhang, and J. D. Xu: Overview of RCS Extrapolation Techniques to Aircraft Targets, Progress In Electromagnetics Research B, Vol. 9, Vol. 9, 249-262, 2008.

[61] LaHaie, I., J.: *An Improved Version of the Circular Near Field-to-Far Field Transformation (CNFFFT)*, Proceedings of the 27th Annual Meeting of the Antenna Measurement Techniques Association (AMTA'05), 196–201, Newport, RI, 2005.

[62] Abramowitz, M., Stegun, I., A.: *Handbook of Mathematical Functions with Formulas, Graphs, and Mathematical Tables*, Dover, New York, 1964.

[63] Korsch, H., J., Klumpp, A., Witthaut, D.: *On Two-Dimensional Bessel Fuctions*, J. Phys. A: Math. Gen. 39, 14947, 2006.

[64] Bracewell, R.: *Fourier Analysis and Imaging*, Springer Science & Business Media, 2004, ISBN 0-306-48187-1.

[65] Jensen, F., Frandsen, A.: *On the Number of Modes in Spherical Wave Expansions*, Proc. 26th AMTA, Stone Mountain Park, GA, Oct. 17-22, pp. 489-94.

[66] Dybdal, R., B.: *Radar Cross Section Measurements*, Proceedings of the IEEE, vol. 75, April 1987, pp. 498-516.

[67] Boersma, J.: *Computation of Fresnel Integrals*, Mathematics of Computation, vol. 14, National Academy of Sciences, National Research Council, Washington, D.C., 1960, p. 380.

[68] Mielenz, K., D.: *Computation of Fresnel Integrals. II*, J. Res. Natl. Inst. Stand. Technol. 105, 589, pp 589-590, 2000.

[69] Muth, L, A.: *Calibration Standards and Uncertainties in Radar Cross Section Measurements*, Proceedings of the 1999 IEEE Radar Conference, Radar into the Next Millennium (Cat. No.99CH36249), Waltham, MA, 1999, pp. 326-331.

[70] Kent, B. M., Chizever, H. M., Soerens, R.: *On Reducing Primary Calibration Errors in Radar Cross Section Measurements*, Proceedings of the 18' Annual Symposium. Antenna Measurement Techniques Association, October 1996, pp383-388.

[71] Chen, V. C., Martorella, M.: *Inverse Synthetic Aperture Radar Imaging: Principles, Algorithms and Applications*, Radar, Sonar, Navigation and Avionics, 2014.

[72] Avinash, C., K., Slaney, M.: *Principles of Computerized Tomography*, Classics in Applied Mathematics, 2001, ISBN: 978-0-89871-494-4.

[73] Saba, L.: *Computed Tomography - Special Applications*, InTech, 2001, ISBN 978-953-307-723-9.

[74] *Computed Tomography*, [online]. Available at:
http://www.rapiscansystems.com/technologies/real_time_tomography

[75] Wells, K., Bradley, D., A.: *A Review of X-ray Explosives Detection Techniques for Checked Baggage*, Applied Radiation and Isotopes, Volume 70, Issue 8, August 2012, Pages 1729-1746, ISSN 0969-8043.

[76] Mellakh, M., A., Petrovska-Delacretaz, D., Dorizzi, B.: *Using Signal/Residual Information of Eigenfaces for PCA Face Space Dimensionality Characteristics*, 18th International Conference on Pattern Recognition (ICPR'06), Hong Kong, 2006, pp. 574-577.

[77] Peng, P., Alencar, P., Cowan, D.: *A Software Framework for PCa-Based Face Recognition*, 2016 IEEE International Conference on Software Science, Technology and Engineering (SWSTE), Beer-Sheva, 2016, pp. 7-16.

[78] Kabourek, V., Cerny, P., Mazanek, M.: *Clutter Reduction Based on Principal Component Analysis Technique for Hidden Objects Detection*, Radioengineering. 2012, 21(1), 464-470. ISSN 1210-2512.

[79] Jackson, J., E.: *A User's Guide to Principal Components*, A Wiley-Interscience Publication, 1991.

[80] Shlens, J.: *A Tutorial on Principal Component Analysis, 2th version*, Institute for Nonlinear Science, University of California, 2005.

[81] Jolliffe I.T.: *Principal Component Analysis*, Series: Springer Series in Statistics, 2nd ed., Springer, NY, 2010, 487 p. 28 illus. ISBN 1441929991

[82] Warne, R., T., Larsen, R.: *Evaluating a Proposed Modification of the Guttman Rule for Determining the Number of Factors in an Exploratory Factor Analysis*, Psychological Test and Assessment Modeling, 56, 104-123, 2014.

[83] Solanas, A., Manolov, R., Leiva, D., Richard's, M., M.: *Retaining Principal Components for Discrete Variables*, Anuario de Psicologia 41, Dec. 2011.

[84] LaHaie, I., J.: *Overview of an Image-Based Technique for Predicting Far-Field Radar Cross Section from Near-Field Measurements*, IEEE Antennas and Propagation Magazine 45(6):159 - 169, January 2004.

[85] Osipov, A., Kobayashi, H., Suzuki, H.: *An Improved Image-Based Circular Near-Field-to-Far-Field Transformation*, IEEE Transactions on Antennas and Propagation, vol. 61, no. 2, pp. 989-993, Feb. 2013.

[86] *R&S ZVA Vector Network Analyzer*, [online], Available at: https://www.rohde-schwarz.com/cz/product/zva-productstartpage_63493-9660.html, Cited 2017-1-11.

[87] *NSI-MI Technologies*, [online] Available at: http://www.nsi-mi.com/ Cited 2016-12-4.

[88] *DRH20 antenna*, [online]. Available at: http:/rfspin.cz/en/antennas/ Cited 2012-1-15.

[89] Sörgel, W., Wiesbeck, W.: *Influence of the Antennas on the Ultra-Wideband Transmission*, EURASIP Journal on Applied Signal Processing, 2005, No. 3, pp. 296-305.

[90] Zwierzchowski, S., Okoniewski, M.: *Antennas for UWB Communications: A Novel Filtering Perspective*, Antennas and Propagation Society International Symposium, 2004, pp. 2504-2507.

[91] Duroc, Y., Ghiotto, A., Vuong, T., P., Tedjini, S.: *UWB Antennas: System With Transfer Function and Impulse Response*, IEEE Transactions on Antennas and Propagation, May 2007, Vol. 55, No. 5, pp. 1449-1451.

[92] Pancera, E., Zwick, T., Wiesbeck, W.: *Spherical Fidelity Patterns of UWB Antennas*, IEEE Transactions on Antennas and Propagation, 2011, Vol. 59, No. 6.

[93] Piksa, P., Sokol, V.: *Small Vivaldi Antenna for UWB*, Proceedings of the Conference RADIOELEKTRONIKA, Brno, 2005.

[94] Nevrly, J.: *Design of Vivaldi Antenna*, Diploma thesis, Prague, 2007.

[95] Cerny, P., Nevrly, J., Mazanek, M.: *Optimization of Tapered Slot Vivaldi Antenna for UWB Application*, Applied Electromagnetics and Communications, IceCOM2007, Dubrovnik, 2007.

[96] Cerny, P., Mazanek, M.: *Optimization of Transient Response Radiation of Printed Ultra Wideband Dipole Antennas (Using Particle Swarm Optimization Method)*, Radioengineering – Proceedings of the Czech and Slovak Technical Universities and URSI Committees, June 2007, Vol. 16, No. 2, Brno, pp. 9-14.

[97] Hansen J., E., (ed.): *Spherical Near-Field Antenna Measurements*, Peter Peregrinus Ltd., on behalf of IEE, London, United Kingdom, 1988.

[98] *Recommended Practice for Near-Field Antenna Measurements*, IEEE Std P1720™/D2 (Draft).

[99] Coleman, C.M., LaHaie, I., J., Rice, S., A.: *Antenna Pattern Correction for the Circular Near Field-to-Far Field Transformation (CNFFFT)*, Proc. of the 27th Annual Meeting of the Antenna Measurement Techniques Association (AMTA), Newport, RI, 2005.

[100] Yang, Z., Liuge, D., Naizhi, W.: *Antenna Pattern Correction Technique for Near-Field RCS Measurement Based on Image*, IEEE 12th International Conference on Electronic Measurement and Instruments, 2015.

List of Candidate's Publications

Stated authors participate equally in listed publications.

Publications Related to This Thesis

Publications in Impacted Journals

[1] Kabourek, V., Černý, P., Mazánek, M.: *Clutter Reduction Based on Principal Component Analysis Technique for Hidden Objects Detection*, Radioengineering. 2012, 21(1), 464-470. ISSN 1210-2512.

Cited in:

- Smitha, N., Singh, V.: *Clutter Reduction using Background subtraction of Ground Penetrating Radar for Landmine Detection*, 2015 IEEE Asian Pacific Conference on Postgraduate Research in Microelectronics and Electronics (PRIMEASIA), pp. 11 - 16, 2015.
- Park, S., Kim, K., Ko, KH.: *Multi-Feature Based Multiple Landmine Detection Using Ground Penetration Radar*, Radioengineering, vol. 23, no. 2, pp. 642 - 651, 2014. ISSN 1210-2512.
- Riaz, MM., Ghafoor, A., Sreeram, V.: *Fuzzy C-Means and Principal Component Analysis based GPR Image Enhancement*, 2013 IEEE Radar Conference (RADAR), 2013, ISBN 978-1-4673-5794-4; 978-1-4673-5792-0. ISSN 1097-5764.
- Riaz, MM., Ghafoor, A.: *Ground Penetrating Radar Image Enhancement Using Singular Value Decomposition*, 2013 IEEE International Symposium on Circuits and Systems (ISCAS), pp. 2388 - 2391, 2013. ISBN 978-1-4673-5762-3; 978-1-4673-5760-9. ISSN 0271-4302
- Montero-de-Paz, J., Garcia-Munoz, LE., Segovia-Vargas, D.: *A 300 GHz "Always-In-Focus" Focusing System for Target Detection*, Radioengineering, vol. 22, no. 2, pp. 610 - 617, 2013. ISSN 1210-2512.

Publications Not Related to This Thesis

Other Publications

[2] Kabourek, V., Černý, P., Mazánek, M.: *Landmine Detection Using Ground Penetrating Radar and Polarimetric Synthetic Aperture Radar*, In: Proceedings of the 5th European Conference on Antennas and Propagation (EuCAP). Piscataway: IEEE, 2011, pp. 42-46. ISBN 978-88-8202-074-3.

[3] Kabourek, V., Černý, P.: *SAR and Stolt Migration Processing for Plastic Landmine Detection*, In: Proceedings of 20th International Conference Radioelektronika 2010. Brno: VUT v Brně, FEKT, Ústav radioelektroniky, 2010, pp. 163-166. ISBN 978-1-4244-6319-0.

[4] Kabourek, V., Černý, P., Piksa, P., Studecký, T., Kania, P., Urban, Š.: *Prague's Emission Fourier Transform Microwave Spectrometer – Design and Preliminary Results*, Radioengineering. 2013, 2013(4), 1288-1295. ISSN 1210-2512.

[5] Černý, P., Kabourek, V., Zvánovec, S., Piksa, P., Kořínek, T., *Emission spectroscopic measurement in Fabry-Perot resonator: Different methods of spectra evaluation*, In: Proceedings of the 6th European Conference on Antennas and Propagation (EUCAP 2012). Piscataway: IEEE, 2012, pp. 577-580. ISBN 978-1-4577-0918-0.

[6] Černý, P., Piksa, P., Zvánovec, S., Kořínek, T., Kabourek, V.: *Improved axial feeding of Fabry-Perot resonator for high-resolution spectroscopy applications*, Microwave and Optical Technology Letters. 2011, 53(11), 2456-2462. ISSN 0895-2477.

Appendices

Appendix A

Measurement Setup in Anechoic Chamber

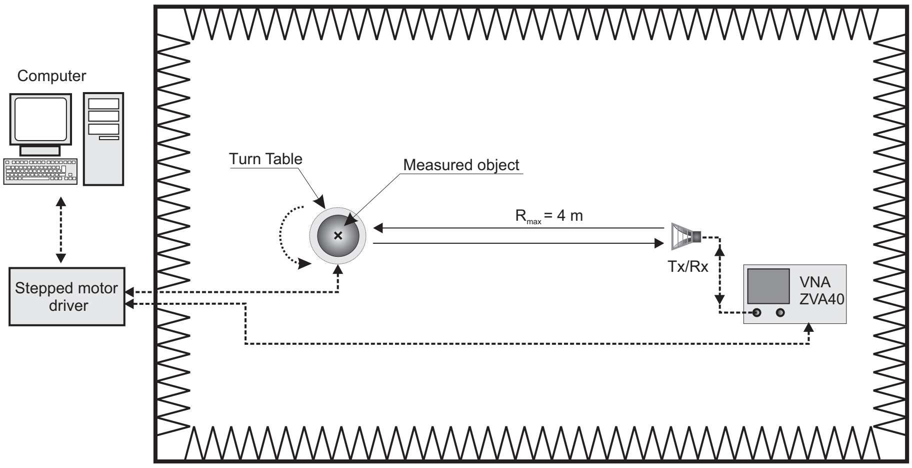

Figure A.1: Monostatic measurement scheme in anechoic chamber

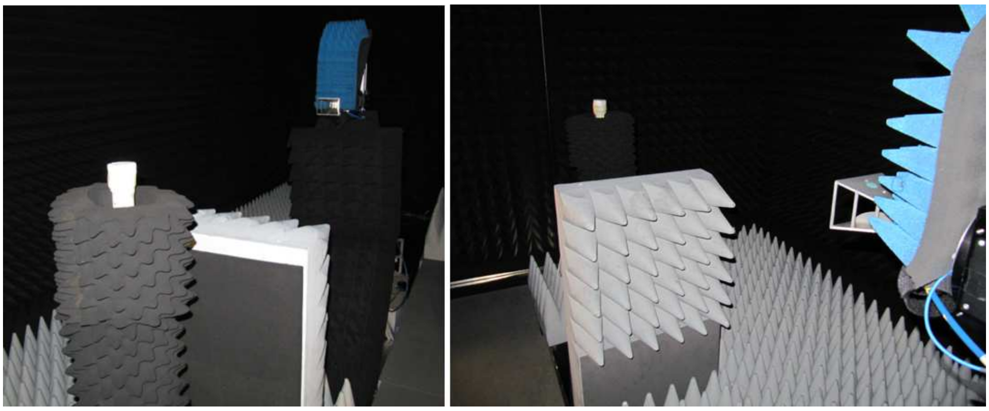

Figure A.2: Rotary support and test antenna in anechoic chamber.

Appendix B

Mason's Rule

The Mason's rule or Mason's formula represents a method to obtain a transfer function of the linear system from so-called signal flow graph. In the Fig. B.1 there is the graph of the general two-port device (transmission line, amplifier, attenuator etc.), where a_1, a_2, b_1 and b_2 represent nodes of the flow graph while the connections of nodes (S_{11}, S_{12}, S_{21} and S_{22}) stand for a paths.

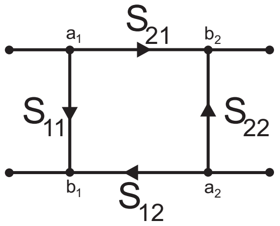

Figure B.1: Flow chart of the 2-port device.

The Mason's formula that describes a transfer function $\frac{b}{a}$ of the general linear system is stated in Eq. (B.1).

$$\frac{b}{a} = \frac{\sum_{m=1}^{M} P_m \left(1 + \sum_{n=1}^{N|_m} (-1)^n \Sigma L(n)^{(m)}\right)}{1 + \sum_{k=1}^{K} (-1)^k \Sigma L(k)} \tag{B.1}$$

P_m is the m-th path from a to b. The path is defined as a sequence of branches that are oriented from the a to b through the nodes, where no node is encountered more than once within the path.

$\Sigma L(n)$ represents the sum of the n-th order loops. The **loop of first order** is defined as a product of the consecutive same-oriented branches connected to the loop.

The **second-order loop** is defined as a product of any two non-touching loops of the first order. Similarly, the **loop of the third order** is created as a product of any three non-touching loops of the first order etc.

$\Sigma L(n)^{(m)}$ denotes the sum of the n-th order loops, that do not touch the m-th loop.

Appendix C

Radon Transform, Projection Slice Theorem

C.1 Radon Transform

Radon transform, or rather its inverse form is widely used in the field of image reconstruction, especially computed tomography, magnetic resonance imaging and also ISAR processing. The transform was originally developed for medical imaging to provide 2D cross-sectional images of 3D object from a set of X-ray transmission measurements collected over 360 degree directions around the object. The forward Radon transform $R_\phi(r)$ of an image represented by the 2D function $f(x, y)$ can be defined as a series of line integrals computed through the image at different distances $r_1 - r_n$ from the origin for a given rotation angle ϕ. Mathematical expression is stated in Eq. (C.1) and overall situation is depicted in Fig. C.1.

The results of the received signals measured from various angles are then integrated to form the image, by means of the Projection Slice Theorem.

$$R(p, \tau) = \int_{-\infty}^{\infty} f(x, \tau + px)\mathrm{d}x = \iint_{-\infty}^{\infty} f(x, y)\delta\left[y - (\tau + px)\right]\mathrm{d}y\mathrm{d}x = U(p, \tau) \qquad \text{(C.1)}$$

Here, variables p and τ represent the slope of line r and intercepts of the integration line with y respectively.

A more frequently used and directly applicable form of the transform can be defined by Eq. (C.2).

$$R(r, \phi) = \iint_{-\infty}^{\infty} f(x, y)\delta(x\cos(\phi) + y\sin(\phi) - r)\mathrm{d}x\mathrm{d}y \qquad \text{(C.2)}$$

This equation utilizes sampling property of Dirac delta function δ - it is nonzero only if the argument of the Dirac function equals zero. The set of integrated lines represents one projection at given rotation angle ϕ. Projections for all azimuthal angles then create matrix (Radon space) referred to as a sinogram, since full 360 degree projections of the point scatterer located off-center forms its sine-like data set.

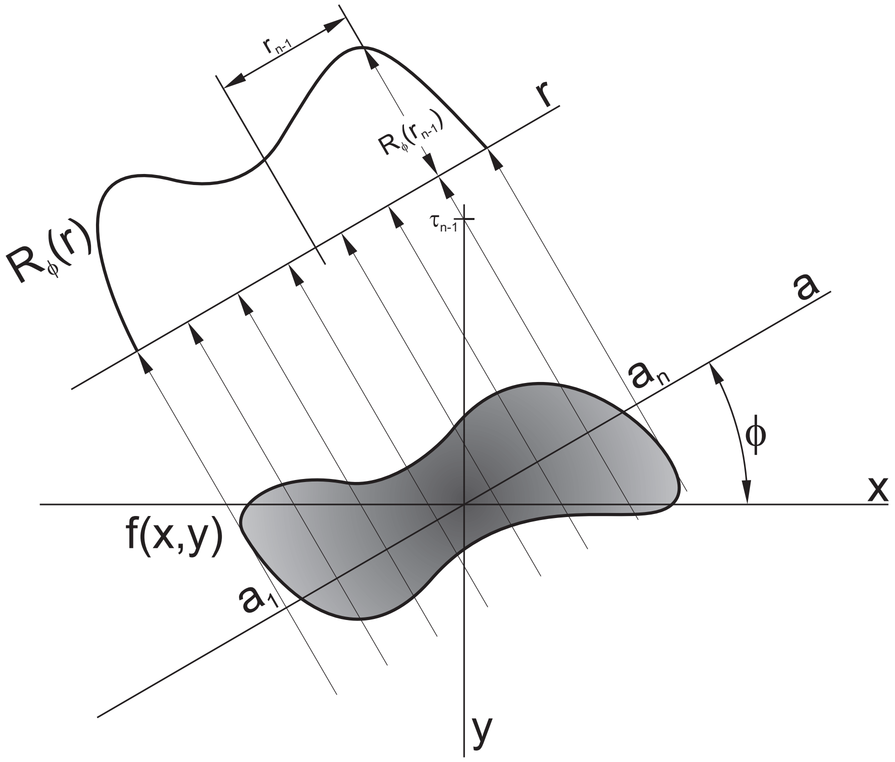

Figure C.1: Schematic derivation of Radon transform.

To reconstruct the image of the object from the sinogram, the inverse Radon transform is applied. There are several techniques by which the inverse transform can be calculated but the most common is Filtered Back Projection that is based on Projection (or Central) Slice Theorem.

C.2 Projection Slice Theorem

Projection slice theorem relates the image of object and its Fourier k-space representation (spatial harmonics) via pairs of Fourier transforms. It states that 1D FT of given projection $P(k_r, \phi)$ is equal to the slice of 2D FT of the image at the same azimuthal angle ϕ as the respective projection. It is more obvious from Fig. C.2 and Eq. (C.3). Function $I(x, y)$ represents back-projected image and k_r is vector of spatial harmonics along line r.

Following this, the image is reconstructed firstly by transforming of measured projections into their spatial harmonics by means of FT. This data set needs to be subsequently mapped and interpolated from circular into Cartesian coordinates and transformed back to image (spatial) domain via 2D IFT. It can be shown, that this transform actually represents filtered back-projection.

$$I(x,y) = \int_{0}^{\pi} \int_{-\infty}^{\infty} P(k_r, \phi)|k_r| \mathrm{e}^{j2\pi k_r (x\cos(\phi) + y\sin(\phi))} \mathrm{d}k_r \mathrm{d}\phi \tag{C.3}$$

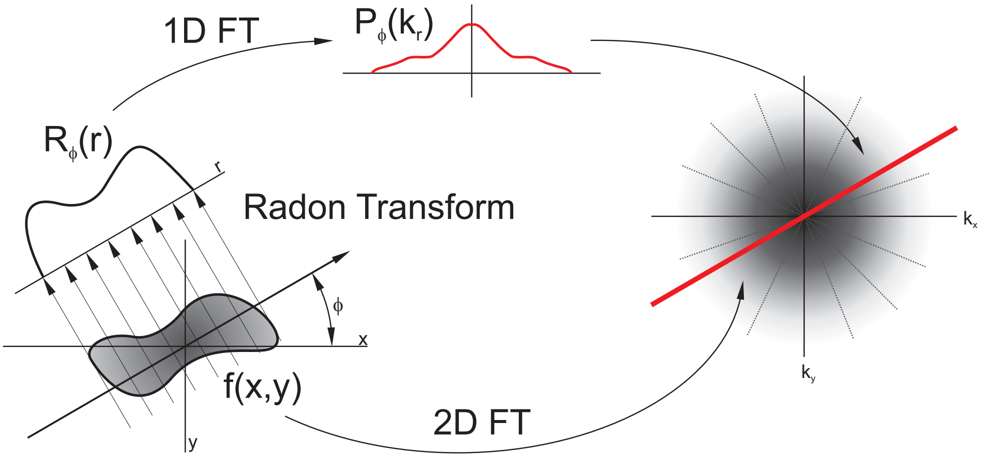

Figure C.2: Projection slice theorem.

C.3 Filtered Backprojection

Filtered backprojection algorithm arises directly from projection slice theorem mentioned above and it is also described by Eq. (C.3). It is split into two phases, filtering and projection. The term $|k_r|$ represents actually ramp filter function. Reconstructed image in k-space domain is thus filtered basically by high-pass filter and subsequently transformed into image domain. The backprojection lies on filling a matrix (representing image space) by particular transformed slice $P(k_r, \phi)$ subsequently for whole angular span $\phi = 0 - 360°$. However, from the principle of Radon transform, the coordinates of scattering centers cannot be exactly determined, only their positions on the integration lines $a_1 - a_n$ (Fig. C.1). The backprojected image is therefore created as depicted in Fig. C.2.

Appendix D

PCA of Reconstructed Images

D.1 PG-7M Missile

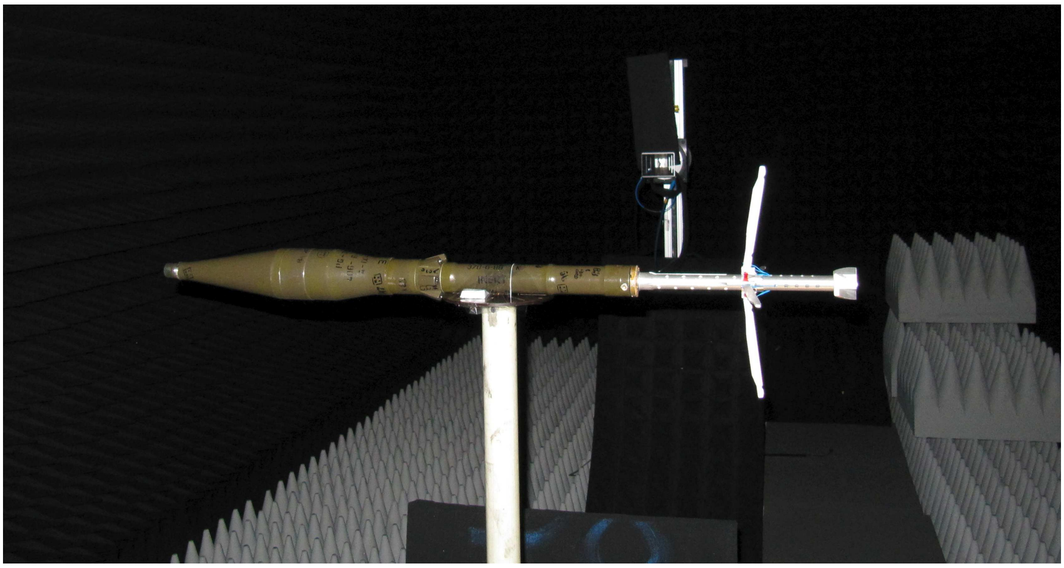

Figure D.1: Image of PG-7M missile in anechoic chamber.

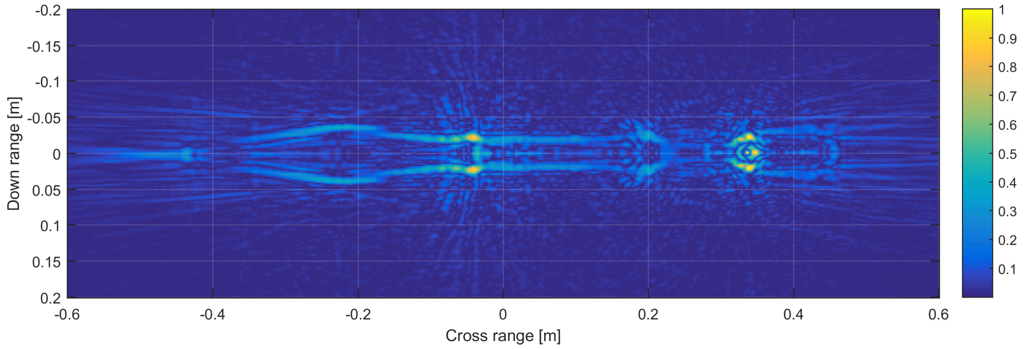

Figure D.2: Reconstructed image of PG-7M from all principal components.

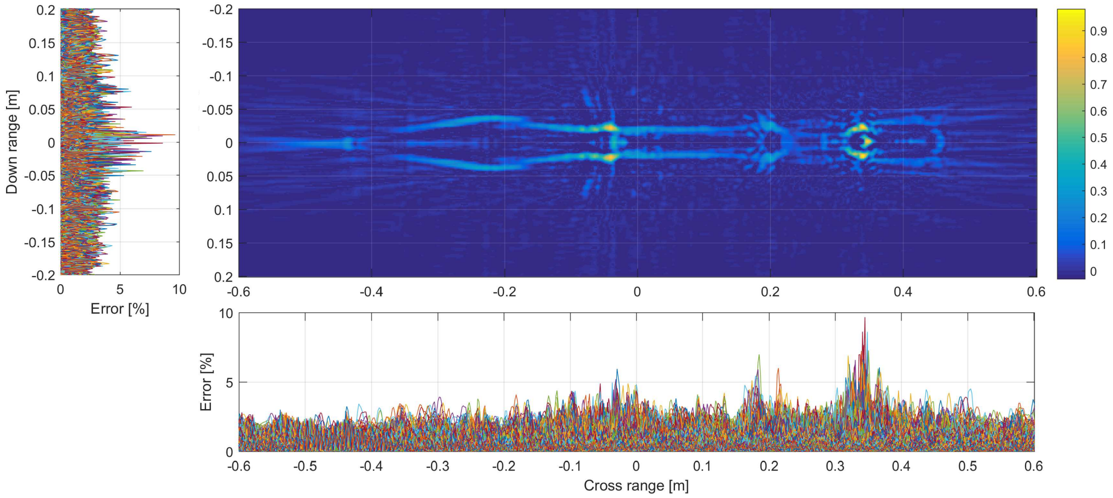

Figure D.3: Reconstructed image og PG-7M from 30 principal components, error below 9.66 %.

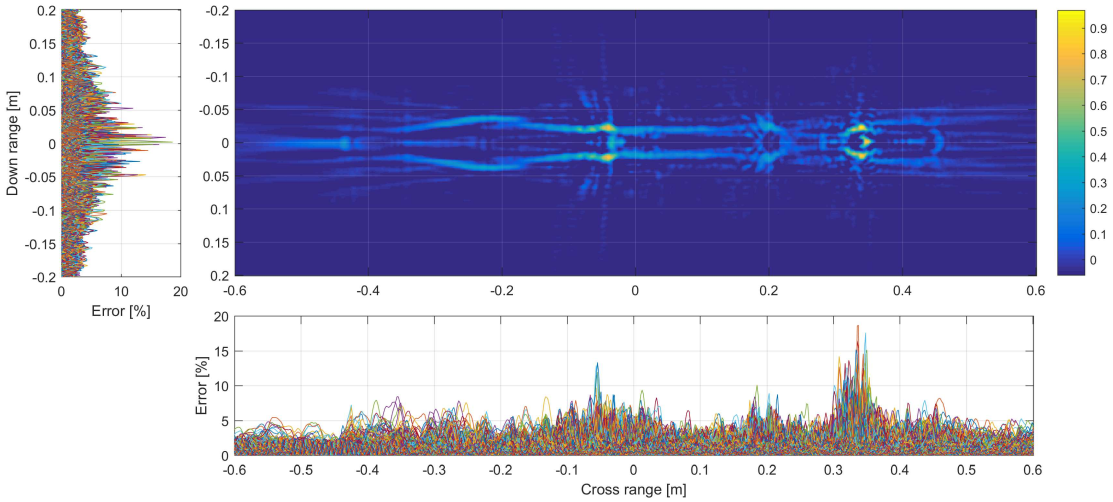

Figure D.4: Reconstructed image of PG-7M from 15 principal components, error below 18.62 %.

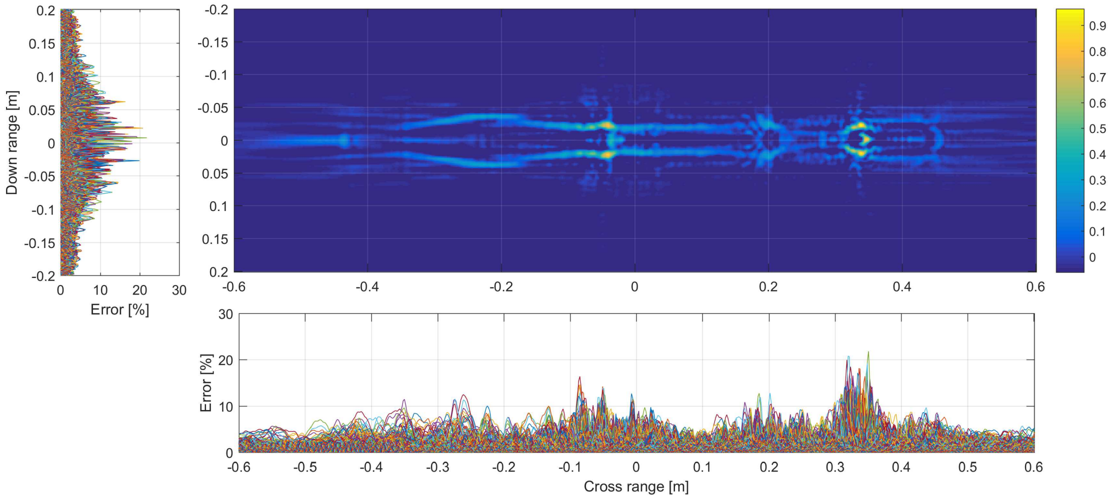

Figure D.5: Reconstructed image of PG-7M from 10 principal components, error below 21.83 %.

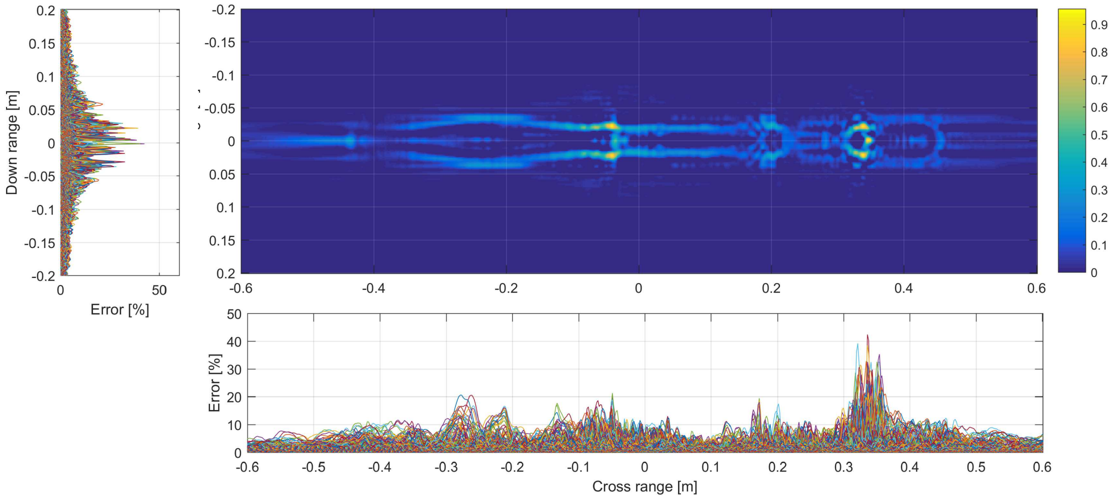

Figure D.6: Reconstructed image of PG-7M from 5 principal components, error below 42.44 %.

D.2 9M14 Malyutka Missile

The target is measured in anechoic chamber at distance 1.5 m, see Fig. D.7. Images of ISAR reconstructed shape of missile and real one are depicted in Fig. D.8. Corresponding principal components and its variances are stated in Fig. D.9, whereas its cumulative sum is outlined in Fig. D.10. It is obvious, that 22 PCs stand for 90 % of total variance and 45 PCs for 95 %. Image is corrupted by additional constant reflection, that is represented by circle in the image, see Fig. D.11. It stands for reflection from absorber situated in front of the target. This and other clutter parts are successively removed by PCA processing, see Fig. D.12 and Fig. D.13.

Figure D.7: Image of 9M14 Malyutka missile in anechoic chamber.

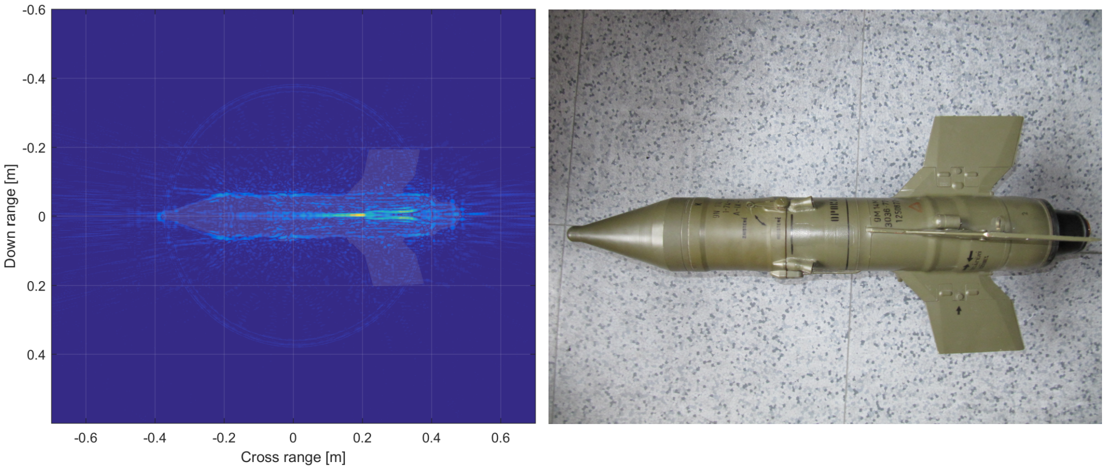

Figure D.8: Comparison of ISAR reconstructed image of 9M14 Malyutka missile and its real image.

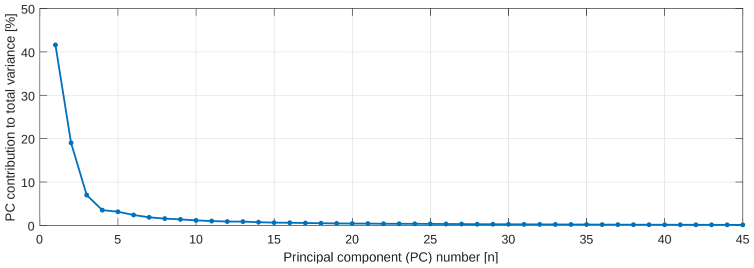

Figure D.9: Contribution of principal components to total variance.

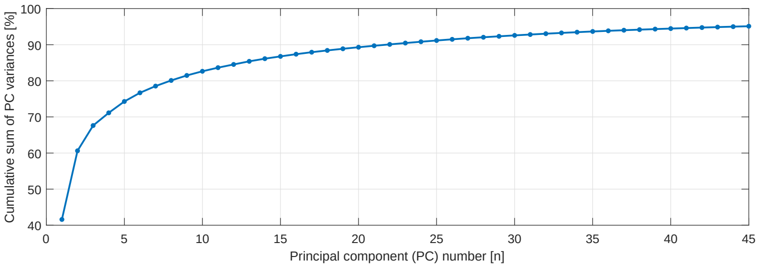

Figure D.10: Cumulative sum of partial variances of principal components.

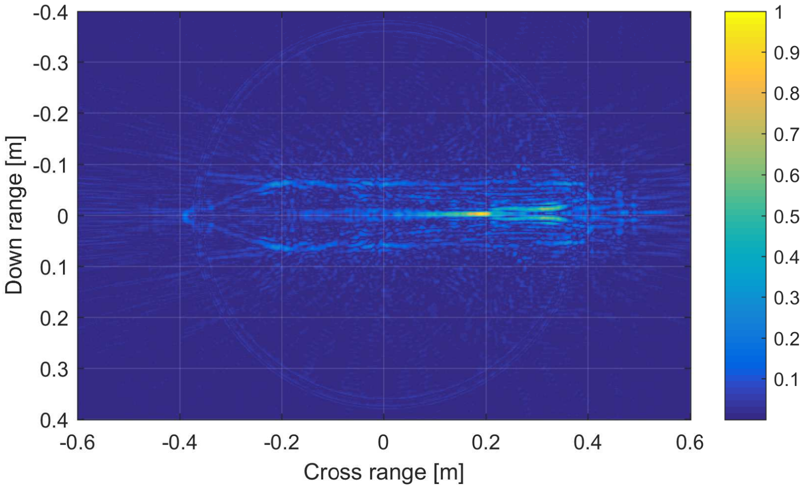

Figure D.11: Reconstructed image of 9M14 Malyutka missile from all principal components.

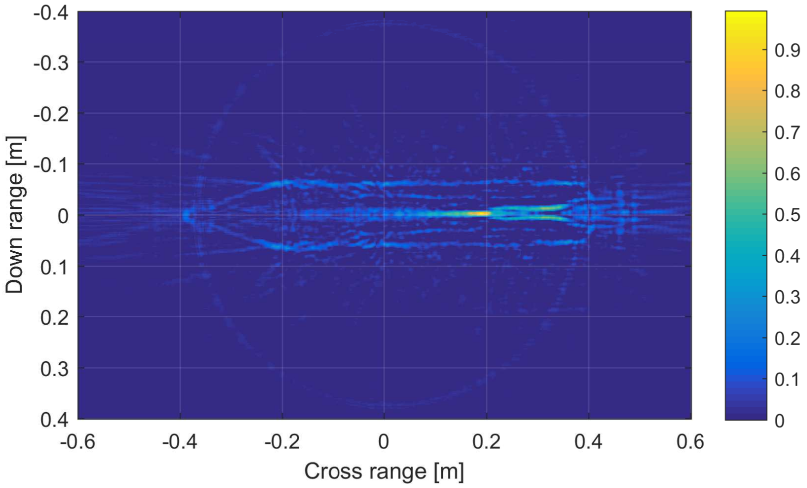

Figure D.12: Reconstructed image of 9M14 Malyutka missile from 45 principal components.

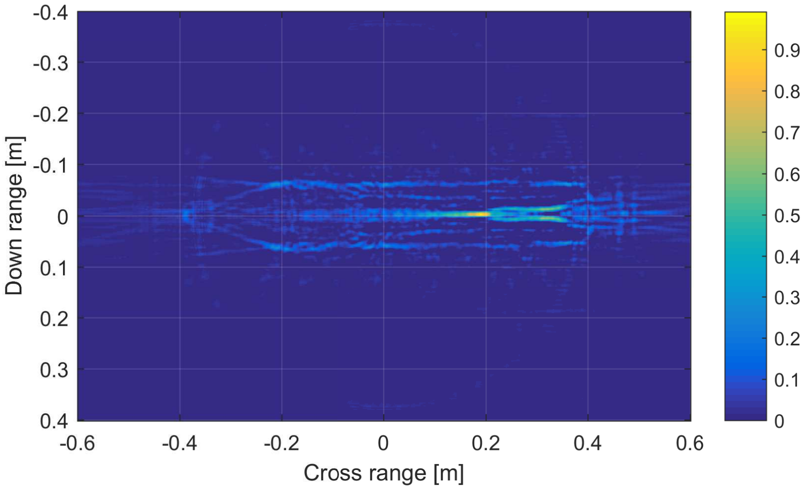

Figure D.13: Reconstructed image of 9M14 Malyutka missile from 22 principal components.